IMPERIAL

Biomechanics of the Trapeziometacarpal Joint during Smartphone Use

A thesis submitted to Imperial College London

for the degree of Doctor of Philosophy

and for the Diploma of Imperial College London

Yumou Han

Department of Bioengineering

Imperial College London

London, SW7 2AZ

January 2026

Declaration of Originality

I declare that this thesis represents my own work and that all sources of information and ideas derived from the work of others have been properly acknowledged and referenced.

Copyright Declaration

The copyright of this thesis rests with the author. Unless otherwise indicated, its contents are licensed under a Creative Commons Attribution-Non-Commercial 4.0 International Licence (CC BY-NC). Under this licence, you may copy and redistribute the material in any medium or format. You may also create and distribute modified versions of the work. This is on the condition that: you credit the author and do not use it, or any derivative works, for a commercial purpose. When reusing or sharing this work, ensure you make the licence terms clear to others by naming the licence and linking to the licence text. Where a work has been adapted, you should indicate that the work has been changed and describe those changes. Please seek permission from the copyright holder for uses of this work that are not included in this licence or permitted under UK Copyright Law.

Acknowledgement

I would like to express my sincere gratitude to my supervisors, Dr Angela Kedgley and Professor Spyros Masouros, for their guidance, support, and patience throughout my PhD. Their expertise and encouragement have been invaluable to this work. Dr Kedgley introduced me to the world of research, and under her mentorship my fundamental skills, such as academic communication, were carefully cultivated. I also admire Dr Kedgley's resilience and professionalism in academia; her consistent commitment to her work, always delivering thoughtful feedback on time, set a standard that I continually aspired to throughout my PhD studies. I am also deeply appreciative of Professor Masouros' rigorous and questioning approach, which facilitate me to scrutinise every aspect of my work and taught me to plan my research with care, ensuring that the methods and results are robust and fully justified. Beyond this, I am thankful for his emphasis on maintaining a healthy balance between work and life, most memorably conveyed through his frequent and timely reminder to "sleep more", even while reading my thesis at 1:30 am.

I am deeply grateful to my family for their unwavering support throughout this journey. Their belief in me provided constant strength, especially during the most challenging moments of the PhD. As my sponsors in every sense, I hope this work proves to be a worthy return on their investment, and I will always strive to be their best one.

I would also like to thank the many friends who stood by me along the way, those who listened and helped soothe my anxiety when the path felt tough. I choose not to name individuals here, not from omission but from abundance, as there are too many people to whom I am grateful, and I would never wish to miss a single one. My gratitude to them is sincere and enduring. I would gladly offer my hand whenever they need it.

Finally, I wish everyone a life in which effort and reward are positively correlated, and in which every sincere endeavour is ultimately acknowledged.

Abstract

Increased smartphone use has altered the functional role of the thumb; from providing stabilisation during daily activities such as gripping objects, to acting as the dominant digit during touchscreen interaction. This shift has raised clinical concerns regarding excessive loading of the trapeziometacarpal (TMC) joint and its potential contribution to early-onset TMC osteoarthritis. However, TMC joint loading during smartphone use remains poorly understood, due, in part, to limitations in experimental measurement of the loading during smartphone use and in relevant computational models of the joint.

This thesis investigated the biomechanical response of the TMC joint during smartphone interaction by integrating experimental measurements of thumb kinematics and kinetics and developing a finite element (FE) model able to predict stresses in the joint. A novel smartphone-sized force plate was designed and validated to capture the low-magnitude thumb forces during natural touchscreen interaction. Combined with optical motion capture, this system enabled synchronised acquisition of thumb-joint kinematics and applied forces during representative smartphone tasks of healthy volunteers. These provided input data for FE simulations of the TMC joint during smartphone activities.

An FE modelling framework of the TMC joint was developed to enable prediction of articular cartilage stress under smartphone-related loading. Systematic sensitivity analyses quantified the influence of key modelling uncertainties, including variability in ligament delineation method and bone geometry, both of which were found to substantially affect predicted cartilage stress distributions.

FE simulations revealed that specific thumb postures during smartphone use produced elevated cartilage stresses, indicating increased mechanical demand at the TMC joint, and therefore risk in developing osteoarthritis. Collectively, this work establishes a robust experimental-computational framework for evaluating TMC joint loading during smartphone use and provides biomechanical evidence to inform ergonomic smartphone

interface and accessory design aimed at reducing excessive TMC-joint loading and mitigating osteoarthritis risk.

Content

Chapter 1 Introduction 1

1.1. Motivation 2

1.2. Aims 3

1.3. Structure of the thesis 4

Chapter 2 Background 6

2.1. Useful terms 7

2.2. Hand and wrist 7

2.2.1. Fingers 8

2.2.2. Wrist 10

2.3. Trapeziometacarpal joint 11

2.3.1. Bony features 11

2.3.2. Ligaments 12

2.3.3. Articular cartilage 14

2.3.4. Osteoarthritis of the trapeziometacarpal joint 14

2.4. Smartphone use 17

2.5. Motion capture system 19

2.6. Force plate 21

2.6.1. Conventional force plates in biomechanics 21

2.6.2. Force measurement techniques for hand and finger activities 21

2.6.3. Custom force plate 24

2.7. Finite element analysis 25

2.7.1. Overview of finite element analysis applications in biomechanics 25

2.7.2. Finite Element Modelling of the Trapeziometacarpal Joint 26

2.7.3. Modelling of Bone 27

2.7.4. Modelling of Articular Cartilage 28

2.7.5. Modelling of Ligaments 29

2.8. Conclusion 33

Chapter 3 A custom force plate for quantifying finger loading during smartphone activities 35

3.1. Introduction 36
3.2. Material and method 37
3.2.1. Force plate design 37
3.2.2. Structural and modal analysis 41
3.2.3. Calibration 42
3.2.4. Accuracy 46
3.2.5. Dynamic validation 48
3.3. Results 48
3.3.1. Natural frequency 48
3.3.2. Calibration 49
3.3.3. Accuracy 52
3.3.4. Dynamic validation 54
3.4. Discussion 55
3.5. Practical technical considerations 58
3.6. Conclusion 59
Chapter 4 Kinetics and kinematics of the thumb during smartphone activities 60
4.1. Introduction 61
4.2. Materials and method 62
4.2.1. Study participant 62
4.2.2. Marker placement and digitisation 62
4.2.3. Experimental protocols 64
4.2.4. Data processing 66
4.3. Results 69
4.3.1. Typing 69
4.3.2. Swiping task 72
4.4. Discussion 78
4.5. Conclusion 84
4.6. Chapter conclusion 85
Chapter 5 Sensitivity analysis of finite element modelling of the trapeziometacarpal joint 86
5.1. Introduction 87

5.2. Method 88
5.2.1. Geometry creation 90
5.2.2. Position setup 91
5.2.3. Simulation type 94
5.2.4. Contact properties 94
5.2.5. Material properties 94
5.2.6. Mesh 97
5.2.7. Boundary conditions 97
5.3. Results 98
5.3.1. Mesh sensitivity 98
5.3.2. Stress distribution of the trapezial cartilage 101
5.4. Discussion 108
5.5. Chapter conclusion 110
Chapter 6 Finite element modelling of the trapeziometacarpal joint during smartphone typing and swiping 111
6.1. Introduction 112
6.2. Method 113
6.2.1. Setup of relative bone orientation 114
6.2.2. Boundary conditions 116
6.2.3. Analysis 118
6.3. Results 119
6.4. Discussion 124
6.4.1. Evaluation of variability in ligament delineation methods 124
6.4.2. Evaluation of variability in CT-scan based geometry 124
6.4.3. Risk of osteoarthritis 125
6.4.4. Ergonomic implication 125
6.4.5. Exclusion of muscle force 126
6.4.6. Exclusion of resulting moment 127
6.4.7. Material property 127
6.4.8. Representation of loading conditions 128
6.5. Chapter conclusion 129
Chapter 7 Summary, Discussion, and Future Work 130

7.1. Summary 131
7.2. Discussion and future work 133
7.2.1. Ligament dataset refinement 133
7.2.2. Population CT-based FE Modelling and Machine Learning Surrogate Prediction 134
7.2.3. Ergonomic improvement for smartphone use 135
7.2.4. Ergonomic Smartphone Case Design to Reduce Thumb Loading 136
7.2.5. Prospective study on joint health 137
7.3. Conclusion 137
References 139
Appendices 162
A.1 Electrical Circuit Design of the Strain Gauge 162
A.2 Error of selected strain gauge combinations 166
A.3 Post-hoc results of position effect on primary degrees of freedom 169
A.4 Kinematics of thumb joints during swiping 175
A.5 Coefficient of determination obtained from partial least squares regression 176
A.6 Methods of delineating trapeziometacarpal ligaments 178

List of Figures

Figure 2.1 Anatomy of the hand (Palmar view). Taken from (Bazira, 2022) with permission 8

Figure 2.2 Movements of the wrist 11

Figure 2.3 Trapeziometacarpal ligaments: (a) dorsal view, (b) deep layer in volar view, (c) superficial layer in volar view. Taken from (Odella, 2018) with permission. 14

Figure 3.1 (a) Exploded schematic of force plate assembly also showing the positions of three of the strain gauges, $\boldsymbol{X1}$, $\boldsymbol{Y1}$ and $\boldsymbol{Z1}$, in one quarter of the plate. All dimensions shown are in mm. (b) Photograph of the internal structure and external appearance of the force plate. 40

Figure 3.2 Flowchart of the methodology 41

Figure 3.3 (a) Calibration grid on interaction platform. Calibration in (b) X direction, (c) Z direction, and (d) Y direction. Calibrations were run by applying a force of 0.5 to 3 N in each of X, Y, and Z directions at each position indicated by red, green and blue dots respectively on the interaction platform. All dimensions shown are in mm. 46

Figure 3.4 Test setup to determine force plate accuracy: (a) diagrammatic side view of the setup; (b) in-plane view of the sloped surface; (c) positions of load application on the surface of the interaction platform. 47

Figure 3.5 Diagram showing the three locations on the interaction platform used for the cyclic loading test. 48

Figure 3.6 Tapping frequency of 10 participants 49

Figure 3.7 Strain $\boldsymbol{EE11}$ (along X direction) and $\boldsymbol{EE33}$ (along Z direction) in the loading cell under a 1-N force applied at central point (x=4, z=4) in (a) X, (b) Y and (c) Z directions 52

Figure 3.8 Error between (a) magnitude of applied and measured force; (b) position of applied and measured position. 53

Figure 3.9 Comparison of the force recorded by the MACH-1 system (solid line) and the force measured by the force plate (dashed line) under sinusoidal loading at 3 Hz over 1000 cycles. 55

Figure 4.1 Placement of clusters of three retroreflective markers on the forearm and hand 64

Figure 4.2 (a) Sizes of three force plates. Dimensions are in millimetres. (b) Experimental setup with a participant performing touchscreen interaction on the force plate. 65

Figure 4.3 Representative synchronized force and joint angle profiles during a typing keypress. The

peak (dashed line) was identified in the force curve (dashed line), and the joint angles for each joint degree of freedom were extracted for the same frame. Joint angles are plotted with an offset for visualization. IP: interphalangeal; MCP: metacarpophalangeal; TMC: trapeziometacarpal; F–E: flexion–extension; A–A: adduction–abduction; I–E: internal–external rotation. 66

Figure 4.4 70

Figure 4.5 Applied force of the thumb during typing when using force plates representing small, medium, and large size smartphones..... 72

Figure 4.6 Range of motion of (a) interphalangeal: flexion–extension, (b) metacarpophalangeal: flexion–extension, (c) trapeziometacarpal: adduction–abduction, (d) trapeziometacarpal: internal–external rotation, and (e) trapeziometacarpal: flexion–extension, when using force plates of small, medium, and large sizes during swiping. 73

Figure 4.7 Applied force by the thumb during swiping when using force plates of small, medium, and large sizes..... 74

Figure 4.8 (a) Representative force and kinematic profiles over five swipe-up and swipe-down cycles. (b) Representative force traces over five swipe-up cycles. (c) Representative force and kinematic profiles over five swipe-left and swipe-right cycles. IP: interphalangeal; MCP: metacarpophalangeal; TMC: trapeziometacarpal; F–E: flexion–extension; A–A: adduction–abduction; I–E: internal–external rotation. 78

Figure 5.1 Workflow for developing finite element models of the trapeziometacarpal joint and the associated software used at each step..... 90

Figure 5.2 Geometry of the model components derived from (a) CT-scan 1, (b) CT-scan 2 and (c) CT-scan 3, represented as surfaces in Geomagic Wrap before meshing. The transverse carpal ligament is represented by the green shell, which was modelled as a rigid structure and served as a reference for the insertion of the ulnar collateral ligament..... 93

Figure 5.3 Boundary conditions of CT scan-3 during dorsal translation. 98

Figure 5.4 Stress distribution on the trapezial cartilage for CT-scan 1 with different mesh element sizes. Maximum stress (Max) is indicated in the unit of MPa. 100

Figure 5.5 Stress distribution on the trapezial cartilage for CT-scan 1 after dorsal translation of 2 mm. From left to right, the results correspond to digitisation operators 1–3. From top to bottom, the results correspond to ligament delineation methods of Bettinger et al. (1999), Nanno et al. (2006)

and Ladd et al. (2012). Maximum von Mises stress was indicated in the unit of MPa. 102
Figure 5.6 Stress distribution on the trapezial cartilage for CT-scan 2 after dorsal translation of 2 mm. From left to right, the results correspond to digitisation operators 1–3. From top to bottom, the results correspond to ligament delineation methods of Bettinger et al. (1999), Nanno et al. (2006) and Ladd et al. (2012). Maximum von Mises stress was indicated in the unit of MPa. 103
Figure 5.7 Stress distribution on the trapezial cartilage for CT-scan 3 after dorsal translation of 2 mm. From left to right, the results correspond to digitisation operators 1–3. From top to bottom, the results correspond to ligament delineation methods of Bettinger et al. (1999), Nanno et al. (2006) and Ladd et al. (2012). Maximum von Mises stress was indicated in the unit of MPa. 104
Figure 5.8 Stress distribution on the trapezial cartilage for CT-scan 1 after volar translation of 2 mm. From left to right, the results correspond to digitisation operators 1–3. From top to bottom, the results correspond to ligament delineation methods of Bettinger et al. (1999), Nanno et al. (2006) and Ladd et al. (2012). Maximum von Mises stress was indicated in the unit of MPa. 105
Figure 5.9 Stress distribution on the trapezial cartilage for CT-scan 2 after volar translation of 2 mm. From left to right, the results correspond to digitisation operators 1–3. From top to bottom, the results correspond to ligament delineation methods of Bettinger et al. (1999), Nanno et al. (2006) and Ladd et al. (2012). Maximum von Mises stress was indicated in the unit of MPa. 106
Figure 5.10 Stress distribution on the trapezial cartilage for CT-scan 3 after volar translation of 2 mm. From left to right, the results correspond to digitisation operators 1–3. From top to bottom, the results correspond to ligament delineation methods of Bettinger et al. (1999), Nanno et al. (2006) and Ladd et al. (2012). Maximum von Mises stress was indicated in the unit of MPa. 107
Figure 6.1 Prescribed trapeziometacarpal joint kinematics used in the finite element simulations for the four loading conditions: typing at key 6, typing at key 1, typing at key 7, and swiping to the left. 116
Figure 6.2 Demonstration of the reference point (red cross) and rigid coupling of the first metacarpal head surface (yellow shade) in the FE model shown as surfaces in Geomagic Wrap before meshing. The transverse carpal ligament is represented by the green shell, which was modelled as a rigid structure and served as a reference for the insertion of the ulnar collateral ligament. 118
Figure 6.3 Stress distribution on the trapezial cartilage for CT-scan 1 during different loading conditions. From left to right, the results correspond to loading conditions: typing at key 6, key 1,

key 7 and swiping to left. From top to bottom, the results correspond to ligament delineation methods of Bettinger et al. (1999), Nanno et al. (2006) and Ladd et al. (2012).....121

Figure 6.4 Stress distribution on the trapezial cartilage for CT-scan 2 during different loading conditions. From left to right, the results correspond to loading conditions: typing at key 6, key 1, key 7 and swiping to left. From top to bottom, the results correspond to ligament delineation methods of Bettinger et al. (1999), Nanno et al. (2006) and Ladd et al. (2012).....122

Figure 6.5 Stress distribution on the trapezial cartilage for CT-scan 3 during different loading conditions. From left to right, the results correspond to loading conditions: typing at key 6, key 1, key 7 and swiping to left. From top to bottom, the results correspond to ligament delineation methods of Bettinger et al. (1999), Nanno et al. (2006) and Ladd et al. (2012).....123

Figure A.1 circuit of strain gauge 162

Figure A.2 Errors between (A, C, E, G, I) the magnitude of the applied and measured force and (B, D, F, H, J) the applied and measured position for the following combinations: $\boldsymbol{X2}$, $\boldsymbol{Y1}$, $\boldsymbol{Y2}$, $\boldsymbol{Y4}$, $\boldsymbol{Z4}$; $\boldsymbol{X3}$, $\boldsymbol{Y1}$, $\boldsymbol{Y3}$, $\boldsymbol{Y4}$, $\boldsymbol{Z3}$; $\boldsymbol{X2}$, $\boldsymbol{Y2}$, $\boldsymbol{Y3}$, $\boldsymbol{Y4}$, $\boldsymbol{Z4}$; $\boldsymbol{X3}$, $\boldsymbol{Y2}$, $\boldsymbol{Y3}$, $\boldsymbol{Y4}$, $\boldsymbol{Z4}$; and $\boldsymbol{X4}$, $\boldsymbol{Y2}$, $\boldsymbol{Y3}$, $\boldsymbol{Y4}$, $\boldsymbol{Z4}$. Outliers, defined as values below the first quartile minus 1.5 times the interquartile range or above the third quartile plus 1.5 times the interquartile range, are denoted by red crosses. 168

Figure A.3 Joint angles of (a) interphalangeal: flexion–extension, (b) metacarpophalangeal: flexion–extension, (c) trapeziometacarpal: adduction–abduction, (d) trapeziometacarpal: internal–external rotation, and (e) trapeziometacarpal: flexion–extension, when using force plates of small, medium, and large sizes during swiping. Positive values represent flexion, adduction, and internal rotation. 175

List of Tables

Table 2.1 Anatomical terminology for the hand and forearm 7

Table 2.2 Intrinsic and extrinsic ligaments associated with the trapeziometacarpal joint and the bones they connect. 12

Table 2.3 Stiffness (N/mm) of AOL, DRL and POL measured elsewhere (Bettinger et al., 2000; D'Agostino et al., 2014; Walker et al., 2025)..... 31

Table 3.1 Dimensions (mm) of the force plate assembly. * Layer 4 consists of 4 identical sections; the dimensions shown are for one piece. 39

Table 3.2 Natural frequencies of the design determined by finite-element modal analysis..... 49

Table 3.3 Regression coefficients and crosstalk of strain gauges. Regression coefficient β represents the sensitivity of each strain gauge to applied forces $\boldsymbol{FX}$, $\boldsymbol{FY}$ and $\boldsymbol{FZ}$ on the centre ($\boldsymbol{x}$=4, $\boldsymbol{z}$=4). Crosstalk (%) is calculated as the ratio of β in one direction to the sum of β across all directions, indicating the relative contribution of each force component to the total output. $\boldsymbol{R2}$ denotes the coefficient of determination for each regression model. NA=Not Applicable. 50

Table 3.4 Coefficients of determination, $\boldsymbol{RFm, n2}$, of the regression between $\boldsymbol{\beta F}$ and coordinates .. 51

Table 3.5 Maximum (max), mean, minimum (min) values and standard deviation (SD) of the error in predicting tri-axial force and position across selected strain gauge combinations..... 54

Table 4.1 Statistical tests conducted in this study. 68

Table 4.2 Post-hoc results of the size effect on primary degrees of freedom. IP: interphalangeal joint; MCP: metacarpophalangeal joint; TMC: trapeziometacarpal joint; F–E: flexion–extension; A–A: adduction–abduction; I–E: internal–external rotation. Statistically different results are only shown (* $\boldsymbol{padj}$<0.05, ** $\boldsymbol{padj}$<0.01, *** $\boldsymbol{padj}$<0.001)..... 69

Table 4.3 Post-hoc results of size effect on force applied by the thumb during typing. Only statistically different results are shown (* $\boldsymbol{padj}$<0.05, ** $\boldsymbol{padj}$<0.01, *** $\boldsymbol{padj}$<0.001). 71

Table 4.4 Post-hoc results of button effect on force. Only statistically different results are shown (* $\boldsymbol{padj}$<0.05, ** $\boldsymbol{padj}$<0.01, *** $\boldsymbol{padj}$<0.001). 71

Table 4.5 Post-hoc results of direction effect on primary degrees of freedom (DoF) IP: interphalangeal; MCP: metacarpophalangeal; TMC: trapeziometacarpal; F–E: flexion–extension; A–A: adduction–abduction; I–E: internal–external rotation. Only statistically different results are

shown (* $\boldsymbol{padj}$<0.05, ** $\boldsymbol{padj}$<0.01, *** $\boldsymbol{padj}$<0.001)..... 72

Table 4.6 Post-hoc results of size effect on force during swiping. Only statistically different results are only shown (* $\boldsymbol{padj}$<0.05, ** $\boldsymbol{padj}$<0.01, *** $\boldsymbol{padj}$<0.001)..... 74

Table 4.7 Weight (in %) of each hand dimension contributing to the first latent component derived from partial least squares (PLS) regression for each combination of force plate size and key position or swipe direction..... 76

Table 5.1 Definitions of the local segment coordinate systems of the first metacarpal and the trapezium (Cooney et al., 1981; Wu et al., 2005). 92

Table 5.2 Stiffness and dimensions of the dorsal radial ligament determined by Bettinger et al. (1999). 96

Table 6.1 Kinematic and kinetic boundary conditions of selected loading conditions, representing 75% joint angles used by the population assessed in Chapter 4 to achieve each task. A-A: adduction–abduction; I-E: internal–external rotation; F-E: flexion–extension..... 114

Table A.1 Post-hoc results of position effect on primary degrees of freedom (DoF). IP: interphalangeal joint; MCP: metacarpophalangeal joint; TMC: trapeziometacarpal joint; F–E: flexion–extension; A–A: adduction–abduction; I–E: internal–external rotation. Statistically different results are only shown (* $\boldsymbol{padj}$<0.05, ** $\boldsymbol{padj}$<0.01, *** $\boldsymbol{padj}$<0.001)..... 174

Table A.2 $\boldsymbol{R2}$ obtained from partial least squares regression (PLS) for all experimental conditions. 177

Table A.3 Dimensions of the TMC ligaments measured by Bettinger et al. (1999) 178

Table A.4 Dimensions of the TMC ligaments measured by Nanno et al. (2006) 178

Table A.5 Dimensions of the TMC ligaments measured by Ladd et al. (2012)..... 178

Publications and Conference Presentations

Journal Article

Han, Y., Vallerini, F.M., Holdsworth, F., Wanglertpanich, K., Kedgley, A.E., Masouros, S.D., 2026. A custom force plate for quantifying the force applied by the finger during smartphone usage. Front. Bioeng. Biotechnol. 14, 1685410. https://doi.org/10.3389/fbioe.2026.1685410

Conference Presentations

Han, Y., Morris, O.A., Kedgley, A.E., Masouros, S.D., 2025. Kinetics and kinematics of the thumb during smartphone typing activities. Presented at the International Society of Biomechanics (ISB), Oral presentation.

Han, Y., Vallerini, F.M., Holdsworth, F., Wanglertpanich, K., Kedgley, A.E., Masouros, S.D., 2025. A custom force plate for quantifying finger loading during smartphone activities. Presented at the European Society of Biomechanics (ESB), Oral presentation.

Han, Y., Kedgley, A.E., 2024. Variability in trapeziometacarpal ligament definitions affects results of finite element model. Presented at the European Society of Biomechanics (ESB), Oral presentation.

Abbreviations

Abbreviation	Explanation
TMC	Trapeziometacarpal
RoM	Range of motion
DoF	Degree of freedom
AOL	Anterior oblique ligament
sAOL	Superior anterior oblique ligament
dAOL	Deep anterior oblique ligament
DRL	Dorsoradial ligament
UCL	Ulnar collateral ligament
POL	Posterior oblique ligament
IML	Intermetacarpal ligament
dIML	Dorsal intermetacarpal ligament
DCL	Dorsal central ligament
DTT	Dorsal trapeziotrapezoid ligament
VTT	Volar trapeziotrapezoid ligament
DT-II MC	Dorsal trapezio-second metacarpal ligament
VT-II MC	Volar trapezio–second metacarpal ligament
T-III MC	Trapezio–third metacarpal ligament
T-C	Trapezio-capitate ligament
RST	Radial scaphotrapezial ligament
TCL	Transverse carpal ligament
VST	Volar scaphotrapezial ligament
CT	Computed tomography
FE	Finite element
MSk	Musculoskeletal
EMG	Electromyography

Chapter 1
Introduction

This chapter introduces the biomechanical and clinical motivation for investigating trapeziometacarpal (TMC) joint loading during smartphone use. It outlines the impact of smartphone interaction on thumb function and existing limitations in experimental and computational approaches and defines the aims and structure of the thesis.

1.1. Motivation

The human thumb is central to hand function, enabling precision, dexterity, and stabilisation during everyday activities. This functional versatility is largely afforded by the TMC joint, whose high mobility allows complex thumb movements but also renders it susceptible to mechanical overload and degenerative change (Neumann and Bielefeld, 2003; Vincent D. Pellegrini, 2001).

In recent decades, smartphones have become widely adopted worldwide, with more than 95% of individuals under the age of 30 using smartphones for over four hours per day (Kim et al., 2024; Kumban et al., 2025; Olson et al., 2022). This intensive pattern of use has shifted the functional role of the thumb from one of providing stability in traditional manual tasks, such as grasping, to the primary effector during smartphone interaction (Karakostis et al., 2021). As a result, the thumb is repeatedly required to perform large-range movements such as swiping and typing, often in non-neutral postures.

Previous research has demonstrated that rapid, repetitive, and non-ergonomic hand and finger movements are associated with the development of musculoskeletal (MSk) disorders, including osteoarthritis and overuse syndromes (Palmer, 2003; Punnett and Wegman, 2004). Consistent with these findings, clinical observations have linked intensive smartphone use to thumb issues, and more recently to cases of early-onset trapeziometacarpal (TMC) osteoarthritis in individuals without conventional risk factors (Canillas et al., 2014). Together, these observations suggest that repetitive, thumb-dominated smartphone interaction may contribute to degenerative changes at the TMC joint.

Despite this emerging evidence, the biomechanical mechanisms underlying the relationship between smartphone use and TMC-joint pathology remain poorly understood.

Finite element (FE) modelling provides a valuable means of examining the internal stress distribution of the TMC joint, which cannot be measured directly *in vivo*. However, modelling this small and complex joint is challenging. There is no consistent delineation method of the TMC ligaments; ligament attachment sites are not directly visible in clinical imaging, and ligament placement must therefore be interpreted by an individual digitising medical imaging data. These factors introduce subjectivity and inter-model variability, making it essential to evaluate the sensitivity of model predictions to ligament delineation method and anatomical assumptions before applying the model to analyse TMC-joint mechanics during smartphone use.

The reliability of FE predictions is also dependent on the accuracy of the boundary conditions used to drive the model. Although established methods exist for measuring joint kinematics (motion capture system) and kinetics (force plate), smartphone interaction involves small-magnitude forces applied under handheld conditions. Conventional commercial force plates lack the sensitivity required to resolve the small-magnitude forces generated during smartphone interactions, which are typically less than 3 N (Kim et al., 2019), and do not replicate the size and mass of a smartphone, thereby altering natural handling and thumb motion. Consequently, the development of a custom force plate capable of resolving small thumb forces while preserving realistic smartphone interaction is a critical component of this research.

Together, these considerations highlight the need for a biomechanically grounded investigation of TMC joint loading during smartphone use. By integrating experimental measurements with TMC FE modelling, this thesis aims to characterise the mechanical response of the TMC joint during smartphone interaction and to support ergonomic smartphone design and usage strategies that reduce excessive thumb loading.

1.2. Aims

The overall aim of this thesis is to investigate the biomechanical response of the TMC joint during smartphone use. Specifically, by integrating experimental measurement of

thumb kinematics and kinetics with FE modelling, the thesis seeks to calculate the stress distribution within the TMC articular cartilage and thus identify factors that may contribute to the development of TMC osteoarthritis associated with smartphone interaction. To achieve this overarching aim, the specific objectives of this thesis are to:

1) develop and validate a custom force plate capable of quantifying thumb forces during natural smartphone interaction;
2) characterise thumb kinematics and kinetics during common smartphone activities under realistic handheld conditions and derive implications for smartphone design and usage habits;
3) develop a FE model of the TMC joint and evaluate the sensitivity of predicted joint mechanics to ligament definition, digitisation-operator interpretation, and bone geometry;
4) examine the stress distribution within the TMC articular cartilage during smartphone use and assess associated risk of developing TMC osteoarthritis.

1.3. Structure of the thesis

This thesis is organised into 7 chapters, structured to progress from background knowledge and experimental data collection to computational modelling and biomechanical interpretation.

Chapter 1 outlines the motivation, aim of this study and the structure of this thesis.

Chapter 2 establishes the anatomical, biomechanical, and modelling background required to investigate TMC-joint loading during smartphone use. It first reviews the structure and function of the hand and thumb, with emphasis on the unique mobility and stabilisation mechanisms of the TMC joint. The chapter then summarises current understanding of TMC osteoarthritis, including its prevalence, risk factors, and proposed biomechanical mechanisms.

The latter sections review existing experimental approaches for measuring thumb kinematics and forces, as well as FE modelling strategies applied to the TMC joint. By synthesising current knowledge and identifying key limitations in experimental measurement and computational representation, this chapter provides the foundation for the experimental and modelling work presented in the subsequent chapters.

Chapter 3 describes the development and validation of a custom force plate to quantify thumb forces during smartphone use. The chapter details the design rationale, calibration procedures, and performance evaluation of the force measurement system.

Chapter 4 investigates thumb kinematics and kinetics during common smartphone activities performed by healthy volunteers. Using the force plate described in Chapter 3 in combination with motion capture, this chapter assesses the influence of task type, device size, and individual hand dimensions on thumb-joint motion and applied forces.

Chapter 5 details the development of a FE model of the TMC joint and evaluates the sensitivity of the model to variability in ligament definition, digitisation-operator interpretation, and bone geometry. The effects of these factors on joint mechanics and cartilage stress distribution are analysed.

Chapter 6 applies the boundary conditions derived from Chapter 4 to the FE model developed in Chapter 5 and predicts articular cartilage stresses. It then interprets these to evaluate the risk of developing osteoarthritis under different smartphone interaction conditions.

Chapter 7 summarises the findings of this research, discusses the limitations of the study, and proposes directions for future work. The chapter concludes by highlighting the contributions of this thesis to the understanding of TMC-joint mechanics during smartphone use.

Chapter 2
Background

This chapter establishes the biomechanical basis of the thesis by linking smartphone use to loading of the trapeziometacarpal (TMC) joint and by exploring how such loading may contribute to degenerative changes. The anatomy and mechanics that enable thumb mobility and the multifactorial origins of TMC osteoarthritis are presented. Smartphone interaction is then examined as a repetitive, high-excursion task that imposes sustained, non-neutral thumb postures, highlighting the need to quantify both thumb kinematics and external forces. The chapter subsequently reviews existing experimental approaches for measuring hand and thumb motion and loading, highlighting their limitations for realistic smartphone use. Finally, the principles and applications of finite element (FE) modelling in TMC joint biomechanics are reviewed, providing the methodological foundation for integrating experimentally measured kinematic and kinetic data with CT-scan based FE models in later chapters.

2.1. Useful terms

Clinicians and anatomists use specialized terminology to describe locations and movements of the wrist and hand. This terminology is presented in Table 2.1.

Terminology	Explanation
Dorsal	Posterior or extensor aspect of the hand and wrist
Volar	Anterior or flexor aspect of the forearm and wrist
Palmar	Referring to the palm side of the hand and fingers
Radial	Towards the side of the forearm and wrist where the radius and radial artery lie. In the hand this refers to the thumb and index finger side.
Ulnar	Towards the side of the forearm and wrist where the ulna and ulnar artery lie. In the hand this refers to the little and ring finger side.
Supination	Turning the palm of the hand anteriorly, also described as external rotation of the forearm.
Pronation	Turning the palm of the hand posteriorly, also described as internal rotation of the forearm.

Table 2.1 Anatomical terminology for the hand and forearm

2.2. Hand and wrist

The human wrist–hand complex is located at the distal end of the upper limb and is composed of a complex arrangement of bones, joints, ligaments, and muscles that together enable both stability and fine manipulation (Bazira, 2022). The skeletal framework of the hand consists of 14 phalanges, 5 metacarpals, and 8 carpal bones (Figure 2.1). Multiple joints contribute to its various ranges of motion, from broad flexion-extension at the wrist to the delicate opposition of the thumb, allowing the hand to grip and orient objects with great dexterity. Below is the review on the primary movements of the wrist, fingers, and thumb, with emphasis on their biomechanics and standard terminology.

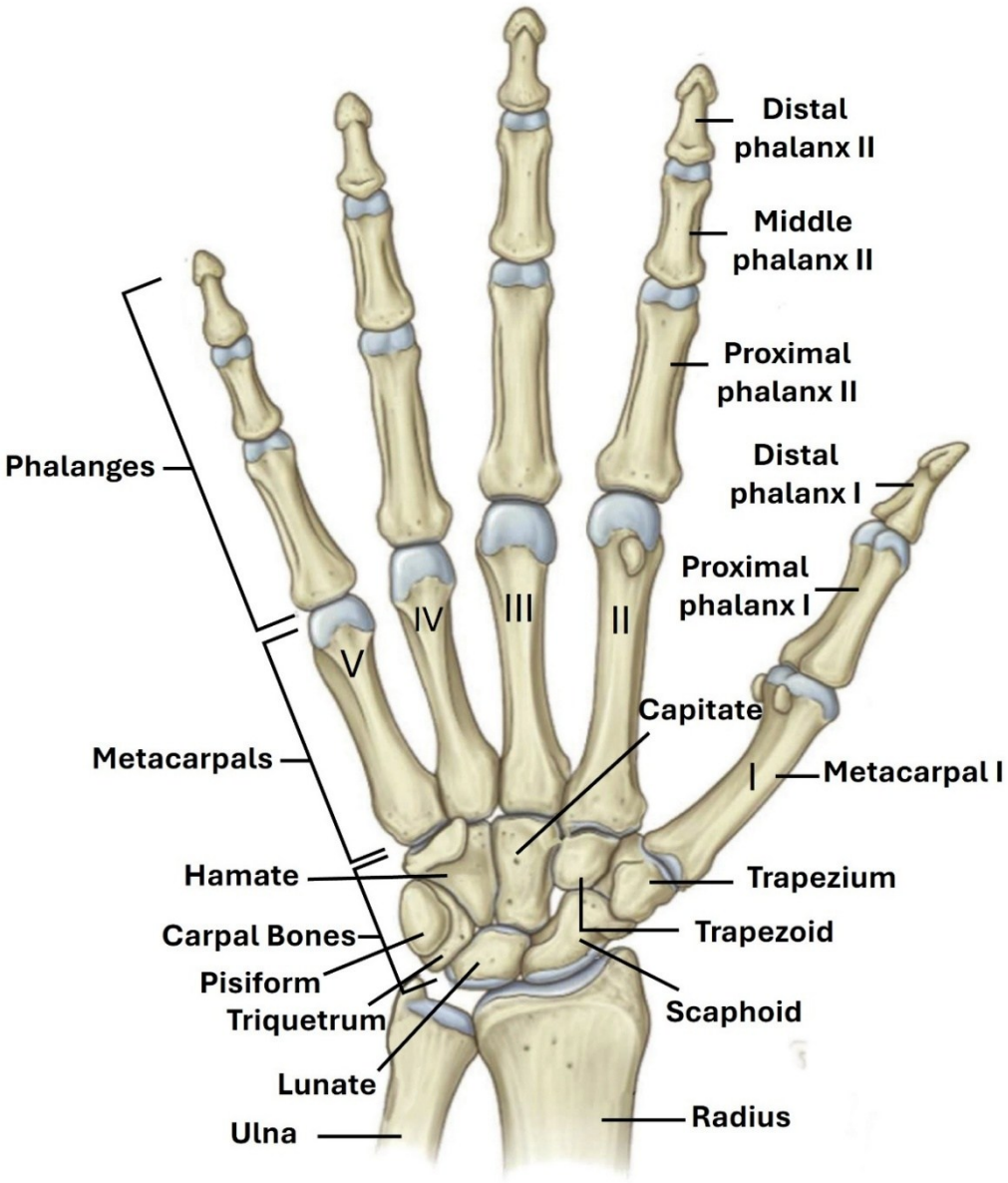


Figure 2.1 Anatomy of the hand (Palmar view). Taken from (Bazira, 2022) with permission

2.2.1. Fingers

Each ray of the hand, except the thumb, is composed of a metacarpal bone and three phalanges: the proximal phalanx, middle phalanx, and distal phalanx. Together, these bones form two interphalangeal (IP) joints (a proximal IP joint and a distal IP joint),

one metacarpophalangeal (MCP) joint and one carpometacarpal (CMC) joint. The IP joints are classified as hinge joints, permitting a single degree of freedom that allows only flexion and extension (bending and straightening the finger). By contrast, the MCP joints are condyloid joints with two degrees of freedom: they permit flexion and extension as well as abduction and adduction, enabling the digits to spread apart or move close together (Rath, 2011). Proximally, each metacarpal articulates with the distal row of carpal bones at the CMC joint. The CMC joints of the index to little fingers are gliding joints, with variable flexibility. The second (index) and third (middle) CMC joints form a rigid central pillar of the hand and are essentially immobile, functioning primarily in load distribution, with mean range of motion (RoM) for flexion-extension of only 11° and 7°, radial-ulnar deviation of 2° and 4°, and axial rotation of 5° each. The fourth (ring) and fifth (little) CMC joints allow greater motion, with RoM for flexion-extension of 20° and 27°, radial-ulnar deviation of 7° and 13°, and axial rotation of 27° and 22°, respectively (El-shennawy et al., 2001; Gray et al., 2021).

The thumb is of particular importance in hand function. Unlike the other four fingers, which each contain three phalanges, the thumb contains only two phalanges: the proximal phalanx (phalanx I proximalis) and the distal phalanx (phalanx I distalis) and therefore possesses only a single IP joint. Despite this reduction in skeletal elements, the thumb achieves remarkable mobility through its unique saddle-shaped articulation, the trapeziometacarpal (TMC) joint, also referred to as the first CMC joint (Imaeda et al., 1992). This joint allows mean RoM of approximately 41° for flexion-extension, 51° for abduction-adduction, and 21° for axial rotation (Barakat et al., 2013; Goubier et al., 2009). Further anatomical and biomechanical details of the TMC joint will be introduced in section 2.3, as this is the joint of interest of this thesis.

In addition to these geometric differences, the musculotendinous organisation of the hand also contributes to differences in digit mobility. The movement of the other four digits is relatively coupled due to shared musculotendinous structures. For example, the flexor digitorum profundus (FDP) originates as a single muscle belly that divides into

tendons supplying digits 2–5, producing flexion at the metacarpophalangeal (MCP) and distal interphalangeal (DIP) joints (Lung and Burns, 2026). Furthermore, although separate tendons exist for finger extension, complete independent extension of each digit is limited by intertendinous connections, including the juncturae tendinum and dorsal intertendinous fascia linking the extensor tendons (Von Schroeder and Botte, 1997).

The thumb, in comparison, is actuated by an independent set of muscles. Four extrinsic muscles: flexor pollicis longus (FPL), extensor pollicis longus (EPL), extensor pollicis brevis (EPB), and abductor pollicis longus (APL); and four intrinsic muscles: flexor pollicis brevis (FPB), abductor pollicis brevis (APB), adductor pollicis (ADP), and opponens pollicis (OPP), control thumb movement (Cooney and Chao, 1977; Paul Smutz et al., 1998). This greater degree of muscular specialisation, combined with reduced mechanical coupling, enhances dexterity of the thumb relative to the other digits.

2.2.2. Wrist

The wrist is an integral part of the hand, serving as the crucial link between the forearm and the structures of the palm and fingers. It is composed of eight carpal bones arranged in two rows. The distal row, comprising the trapezium, trapezoid, capitate, and hamate, articulates with the bases of the metacarpal bones. The proximal row, consisting of the scaphoid, lunate, triquetrum, and pisiform, articulates primarily with the distal radius and ulna of the forearm (Wadsworth, 1983).

Wrist motion is primarily bi-planar, encompassing flexion-extension, as well as radial-ulnar deviation (Figure 2.2) (Volz et al., 1980). In contrast, pronation–supination, often misinterpreted as wrist motion due to the visible rotation of the hand, occurs at the proximal and distal radioulnar joints of the forearm, where the radius rotates about the

ulna.

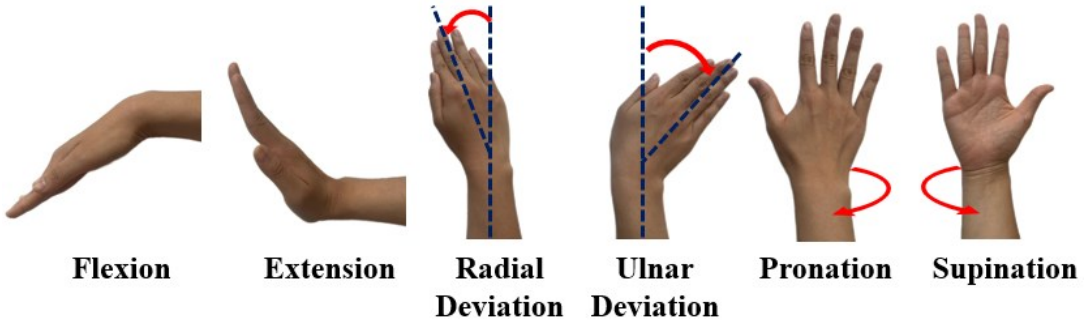


Figure 2.2 Movements of the wrist

2.3. Trapeziometacarpal joint

2.3.1. Bony features

The TMC joint is located at the base of the thumb, where the first metacarpal articulates with the trapezium, one of the distal carpal bones. Unlike the relatively constrained CMC joints of the other fingers, the TMC joint is highly mobile because of its specialised structure. Morphologically, the TMC joint is classified as a saddle joint with biconcave-convex geometry, in which each articular surface is concave in one dimension and convex in the perpendicular dimension (Edmunds, 2011; Gillis et al., 2011). This configuration creates an articulation capable of two principal degrees of freedom: flexion-extension (F-E) and abduction-adduction (A-A), with a limited degree of coupled axial rotation, permitting a broad range of thumb movements (Bettinger et al., 1999; Neumann and Bielefeld, 2003; Toft and Berme, 1980).

2.3.2. Ligaments

Bettinger et al. (1999) specified the position and function of 16 ligaments attached to the trapezium and the first metacarpal (Table 2.2).

Ligaments	Connecting Bones
SAOL	Trapezium — the first Metacarpal
DAOL	Trapezium — the first Metacarpal
UCL	Transverse carpal ligament — the first Metacarpal
DRL	Trapezium — the first Metacarpal
POL	Trapezium — the first Metacarpal
IML	the first Metacarpal — the second Metacarpal
DIML	the first Metacarpal — the second Metacarpal
DTT	Trapezium — Trapezoid
VTT	Trapezium — Trapezoid
DT-II MC	Trapezium — the second Metacarpal
VT-II MC	Trapezium — the second Metacarpal
T-III MC	Trapezium — the third Metacarpal
T-C	Trapezium — Capitate
RST	Trapezium — Scaphoid
VST	Trapezium — Scaphoid
TCL	Hamate and Pisiform — Scaphoid and Trapezium

Table 2.2 Intrinsic and extrinsic ligaments associated with the trapeziometacarpal joint and the bones they connect.

Seven ligaments directly resist the forces acting on the TMC joint: superior anterior oblique ligament (sAOL), deep anterior oblique ligament (dAOL), dorsoradial ligament (DRL), posterior oblique ligament (POL), ulnar collateral ligament (UCL),

Intermetacarpal ligament (IML), and dorsal intermetacarpal ligament (dIML) (Figure 2.3). The AOL has been described as “broad and strong,” and its degeneration has been associated with articular damage in early osteoarthritis (Eaton and Littler, 1973). Pellegrini (1991) concluded that the AOL plays a key role in maintaining volar stability of the TMC joint. The DRL, described as a “strong ligamentous structure,” spans a larger surface area than any other TMC ligament (Bettinger et al., 1999). Its mechanical importance has been verified experimentally. Strauch et al. (1994) observed the greatest subluxation following DRL removal in a sequential ligament sectioning study, and Rusli and Kedgley, (2020) reported the largest translation increment after DRL sectioning in controlled loading tests. The dorsal ligament group, including the DRL and POL, is generally thicker and exhibits greater neural innervation density than the anterior ligaments, whereas the AOL has little or no innervation. These morphological and sensory characteristics suggest that the dorsal ligaments play a more dominant role in joint stabilization than the anterior ligaments (Ladd et al., 2012; Lin et al., 2014).

The UCL extends from the ulnar aspect of the trapezium to the ulnar base of the first metacarpal and provides secondary resistance against ulnar and volar translation, especially during pinch loading. Although less extensively examined than the AOL and DRL, both anatomical and sectioning studies confirm its contribution to overall TMC joint stability (Bettinger et al., 1999; Gómez et al., 2017; Strauch et al., 1994).

The IML and DIML assist in maintaining TMC joint stability by limiting metacarpal translation. Anatomical investigations indicate that these ligaments act as secondary stabilisers, particularly resisting radial displacement of the first metacarpal (Gómez et al., 2017).

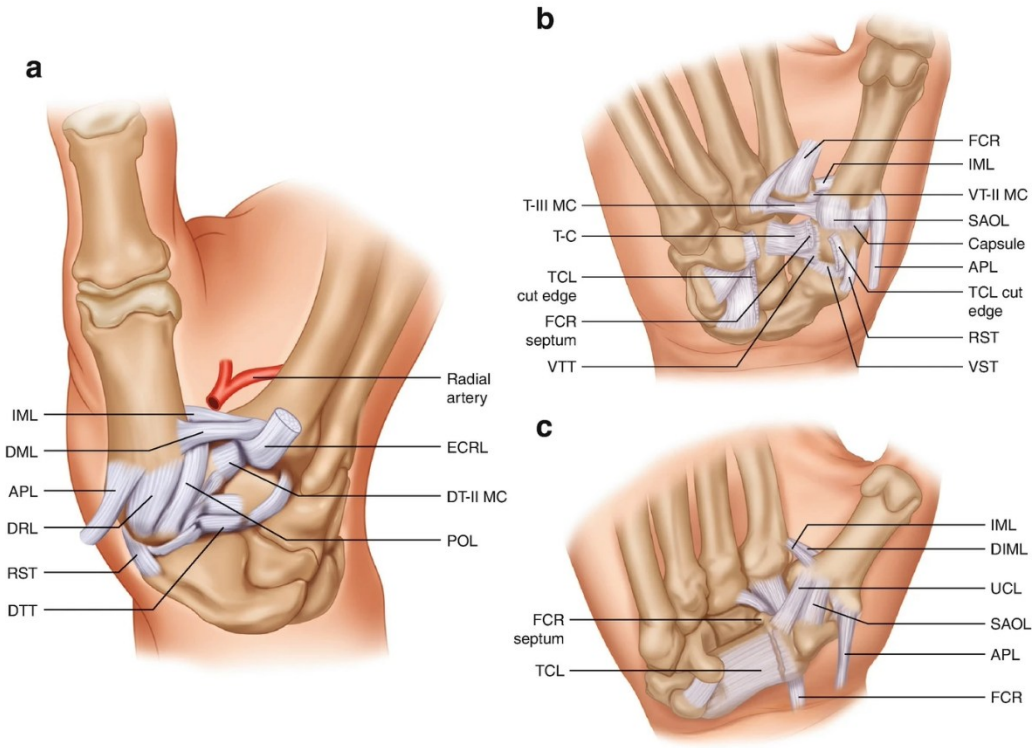


Figure 2.3 Trapeziometacarpal ligaments: (a) dorsal view, (b) deep layer in volar view, (c) superficial layer in volar view. Taken from (Odella, 2018) with permission.

2.3.3. Articular cartilage

Articular cartilage is a thin layer of connective tissue covering the ends of bones, containing large amounts of water, proteoglycan, and collagen fibres. It functions as the gliding surface of synovial joints. The surface is smooth and lubricated, reducing friction and promoting mobility at joints (Sophia Fox et al., 2009).

2.3.4. Osteoarthritis of the trapeziometacarpal joint

TMC osteoarthritis is a debilitating disease that affects many people (Bettinger et al., 1999; Gillis et al., 2011; V. D. Pellegrini, 2001). Common symptoms of TMC-joint arthritis can include joint pain, especially exacerbated by pinch or grasping actions,

reduced grip strength, joint stiffness, and swelling at the base of the thumb (Neumann and Bielefeld, 2003). These symptoms can significantly reduce the dexterity during activities of daily living such as brushing teeth, turning a key and using a smartphone (Kim et al., 2019; V. D. Pellegrini, 2001). The aetiology of TMC osteoarthritis is widely recognised as multifactorial, encompassing both intrinsic determinants such as anatomical features, ligamentous integrity, and systemic hormonal influences, and extrinsic contributors including cumulative mechanical loading and repetitive use.

Sex and hormonal status are particularly salient intrinsic determinants. A study investigating 3595 subjects in Finland indicated that 7% of men and 15% of women over 30 years old are afflicted by TMC osteoarthritis (Haara et al., 2004). 25% of American women over the age of 55 years are reported to have TMC osteoarthritis (Zhang et al., 2013); Nottingham University Hospital found that the prevalence of TMC osteoarthritis of women aged 45 to 70 years is 33% (Armstrong et al., 1994). The decline in circulating oestrogen following menopause has been hypothesised to facilitate ligamentous laxity and to alter chondrocyte metabolism, thereby accelerating degenerative processes. The presence of oestrogen receptors within periarticular tissues provides biological plausibility; although, the precise causal pathways remain incompletely elucidated (Lou et al., 2016; Roman-Blas et al., 2009).

Advancing age and the cumulative mechanical demands placed on the thumb also contribute to TMC osteoarthritis. Repeated pinch, grasp, and torque tasks performed over decades induce progressive degradation of the articular cartilage and osteophyte formation (Guilak, 2011; Venne et al., 2020). Although definitive occupational risk data remain limited, studies of manual workers have suggested that there is an association between manual work necessitating repetitive or forceful load on the thumb and increased prevalence of TMC osteoarthritis (Lewis et al., 2025; Wolf et al., 2020).

Due to the lack of bony constraint on the radial side of the wrist, the TMC joint is largely stabilised by ligaments. Consequently, ligamentous laxity leads to

destabilisation of the joint and is regarded as a key factor in the pathogenesis of TMC joint osteoarthritis (Bettinger et al., 2000, 1999; Gillis et al., 2011; Imaeda et al., 1993; Pellegrini, 2001). Specifically, TMC joint osteoarthritis is associated with hypermobility and dorsoradial subluxation of the joint. The AOL (or volar beak ligament) and the DRL, constraining dorsoradial translation, have been identified as the main stabilisers of the TMC joint. Investigations with cadaveric specimens have demonstrated a correlation between AOL degeneration and the presence and severity of TMC osteoarthritis. Furthermore, DRL has been shown to play a critical role in TMC joint stability, as its rupture results in significant metacarpal translation and is significantly associated with the presence and regional progression of osteoarthritis (Gómez et al., 2017). Attenuation or elongation of the ligaments permits subluxation during pinch and opposition. This pathological redistribution of load initiates joint instability and progressive wear (Pellegrini, 1991).

Morphological variation of the TMC joint has emerged as another critical determinant of osteoarthritis risk. Prominent differences in features such as articular surface curvature, bone size, and the ratio of articular surface area to total bone surface area have been reported between individuals with thumb osteoarthritis and healthy populations (Halilaj et al., 2014; Neumann and Bielefeld, 2003). Morphological variation of the TMC joint among healthy individuals has also been demonstrated through statistical shape modelling (Rusli and Kedgley, 2020). Finite-element (FE) analyses have shown that variations in trapezial geometry, particularly, a reduced drooler curvature, increase joint contact stresses during pinch and grip, thereby predisposing the joint to degeneration (Valerio et al., 2023). Statistical shape modelling further indicates that torsional changes of the distal metacarpal head and regional differences in bone morphology alter shear forces and compromise stability, thereby elevating the risk of disease onset (Fu et al., 2023). Longitudinal imaging studies have also demonstrated that osteophyte growth occurs in consistent, non-opposing regions of the trapezium and first metacarpal, suggesting that local bone morphology directs

the spatial pattern of degeneration (Crisco et al., 2019). Collectively, these findings establish that anatomical variability influences joint congruence and loading, underscoring morphology as a primary driver in the initiation and progression of TMC-joint osteoarthritis.

2.4. Smartphone use

Smartphone use has become ubiquitous, with over 50% of the global population now using a smartphone, with this percentage reaching 80% in high-income regions such as North America and Europe (Olson et al., 2022). Adolescents and young adults consistently emerge as the heaviest users: across studies from multiple countries including Thailand, South Korea, and the United States, over 95% of individuals under 30 years old own a smartphone, with average daily use commonly exceeding four hours (Kim et al., 2024; Kumban et al., 2025; Olson et al., 2022). University students show even higher levels of use, with nearly one-third spending more than eight hours on smartphones each day (Kaewpradit et al., 2025; Kumban et al., 2025). Importantly, smartphone adoption is no longer confined to younger populations. Older adults have embraced this technology, with ownership among those aged 65 years and older rising from only about 10% in 2011 to 61% in 2021 (Pew Research Center, 2024, 2014).

With this widespread and prolonged use of smartphones, numerous studies have linked smartphones to MSk problems, particularly in the upper extremities. Due to the current design of smartphones, the device is often held with one hand, using the thumb to navigate. However, traditionally, the thumbs are used to grip or stabilise the hand while the other fingers perform the task. Smartphone use reverses this role, requiring the thumb to execute frequent and wide-ranging movements to interact with the smartphone's touchscreen (Jonsson et al., 2007; Sampath et al., 2022).

Cross-sectional studies have consistently demonstrated significant associations

between long term use of smartphone and pain in the neck, shoulders, wrists, and thumbs, with symptom prevalence exceeding 50% in some populations (Al-Dhafer et al., 2023; Baabdullah et al., 2020). Overuse has also been associated with specific pathologies such as De Quervain's tenosynovitis and reduced grip strength (Athar et al., 2025).

Overuse-related upper extremity disorders have been documented in other repetitive thumb- and hand-intensive activities. A systematic review of musicians reported a lifetime prevalence of playing-related musculoskeletal disorders of up to 89%, with the hand and wrist among the most commonly affected regions, presenting with pain, weakness, stiffness, and reduced motor control (Betzl et al., 2020). Likewise, acute overuse injuries have been described in gaming contexts, such as a case of wrist pain and symptoms consistent with carpal tunnel syndrome following prolonged use of a motion-controlled Nintendo Wii game (Boehm and Pugh, 2009).

Emerging evidence has raised concerns regarding the potential link between excessive smartphone use and degenerative joint conditions. A widely cited case report even described "WhatsAppitis," an acute bilateral thumb tenosynovitis provoked by excessive use of a smartphone to write messages (Fernandez-Guerrero, 2014). More concerning are reports of young women developing TMC-joint osteoarthritis without other predisposing factors, where excessive touchscreen phone use was identified as the primary exposure (Canillas et al., 2014). These cases suggest that repetitive, thumb-dominated smartphone interactions may accelerate degenerative changes in the TMC joint. Given the continuing global increase in smartphone use across all age groups, the prevalence of thumb-related pain and MSk disorders are likely to increase.

Biomechanical investigations have provided mechanistic support for these clinical observations. Compared with keypad phones, touchscreen devices require greater thumb abduction, flexion, and excursion, and elicit higher activation of the thenar musculature (Gustafsson et al., 2018, 2010). Postural studies confirmed that prolonged

smartphone tasks involve sustained non-neutral positions of the thumb and wrist, creating an environment of elevated mechanical loading (Berolo et al., 2011). Collectively, these findings highlight that the physical demands of smartphone interaction are concentrated on the thumb and may contribute to MSk strain and early degenerative disease. This makes the impact of smartphone use on TMC-joint health an important topic for further investigation.

To investigate joint mechanics associated with smartphone use, thumb kinematics and kinetics need to be collected. Optical motion capture systems are commonly used to characterise three-dimensional joint motion, while force measurement devices, such as force plates, are used to quantify ground reaction forces during functional tasks. Together, these data provide inputs for FE modelling of the TMC joint. The following sections review the principles of these measurement techniques and summarise their application in existing studies.

2.5. Motion capture system

Understanding human joint motion has long been a central goal in biomechanics. Early pioneers relied on simple observational and manual tools to quantify movement. Clinical measurements of joint range of motion traditionally used goniometers, rulers, or tape measures to record angular or linear displacements. While these manual methods are simple and accessible, they are prone to error; differences of up to 5–10° can occur due to observer bias and alignment variability (Cook et al., 2007). As the demand for more precise and dynamic assessments increased, dedicated motion capture technologies were developed.

The origins of motion capture can be traced back to 1872, when Eadweard Muybridge designed an automatic electro-photographic apparatus that triggered multiple cameras in rapid succession to capture consecutive phases of animal and human motion

(Muybridge, 1887). This innovation introduced the core principle underlying modern optical motion capture systems: recording sequential images to reconstruct motion.

Nowadays, motion capture systems with skin-mounted markers have become the gold standard for capturing joint kinematics in three dimensions. In a typical laboratory setup, reflective markers or LED markers are affixed to anatomical landmarks, and a network of synchronized infrared cameras tracks their 3D positions throughout motion (Kobsar et al., 2020). The cameras triangulate the reflected light to reconstruct marker trajectories in global coordinates, which are then processed to compute segment orientations, joint angles, and angular velocities using rigid-body models. To define local coordinate systems, a digitising wand is often used to record the spatial locations of specific bony landmarks, improving the anatomical accuracy of joint centre estimations. This approach provides high-resolution kinematic data for dynamic movements and is widely applied in biomechanics, ergonomics, and rehabilitation research.

However, markers affixed to the skin are subject to soft tissue artefacts (STA), as the skin and subcutaneous tissues move relative to the underlying bones. This relative displacement introduces discrepancies between measured marker trajectories and true skeletal motion. Several strategies have been proposed to mitigate these errors. A common approach is to place markers on regions with minimal soft tissue movement, such as bony prominences or areas with thinner tissue (Ancillao et al., 2021; Metcalf et al., 2020).

To ensure comparability of kinematic data across participants, motion analyses require the definition of local coordinate systems based on consistent bony landmarks. As some of these landmarks may be difficult to palpate accurately or subject to STAs, digitisation procedures are employed to record their 3D positions relative to the marker clusters. This process enables precise alignment of the motion capture model with skeletal anatomy and promotes reproducibility across subjects (Cappozzo et al., 1995; Wu et al.,

2005).

2.6. Force plate

2.6.1. Conventional force plates in biomechanics

Because joint-contact mechanics depend on both kinematics and kinetics, motion-capture data must be complemented by synchronous force measurements to characterise the mechanical interactions that occur during smartphone use. This section describes the force plate and associated instrumentation used to capture these loads and outlines the synchronisation with the motion capture system for integrated kinematic–kinetic analysis.

Traditionally, kinetic data in human biomechanics, especially for applications like gait analysis, have been collected using tri-axial force plates. These force plates are embedded in laboratory floors and are designed to measure the ground reaction forces (GRFs) generated when people walk, run, or perform other movements (Bamberg et al., 2008; Benedetti et al., 1998; Kanai et al., 2008; Nagano et al., 2010). Common laboratory force plates, such as those produced by Kistler and AMTI, are typically large and heavy, with surface dimensions of approximately 40–60 cm and a thickness of 5–10 cm, and are capable of measuring forces ranging from a few newtons to several kilonewtons. Although highly accurate for whole-body studies, their bulk and limited sensitivity make them unsuitable for small-scale forces such as those produced by the fingers.

2.6.2. Force measurement techniques for hand and finger activities

Given these limitations, several alternatives have been developed to capture small-scale interaction forces. Pressure-based sensing technologies have been explored. Austin et

al. (2022) integrated multiple piezoresistive sensors into wearable gloves, enabling distributed measurement of contact forces during activities of daily life such as grasping or key turning. These gloves captured individual phalangeal force up to 9 N at the middle finger and 24 N at the thumb, showing potential for monitoring realistic hand interactions. Santos et al. (2022) attached differential pressure sensors to the palmar and dorsal surfaces of the hands to estimate resultant hand forces, providing a scalar magnitude of propulsive force during swimming. Sengupta et al. (2022) developed flexible 3D graphene–PDMS spongy pressure sensors that convert compressive strain into electrical resistance changes, enabling the measurement of normal contact forces in wearable and consumer applications.

Despite their flexibility and ease of integration, pressure sensors exhibit limited accuracy and reliability for small, dynamic interactions. They typically detect only normal (single axis) forces, lacking directional information. Their piezoresistive and capacitive structures exhibit nonlinear responses, hysteresis, and signal drift under continuous or dynamic loading (Parmar et al., 2017; Seesaard and Wongchoosuk, 2023). Their relatively low temporal resolution further limits their use in capturing fast, transient gestures such as tapping or swiping during smartphone interaction.

Tri-axial force measurements have also been developed to capture 3D characteristics of finger–surface interactions. Multi-axial load cells have been attached to touchscreen and handheld devices to quantify fingertip force during tapping, swiping, and pinching gestures. These studies report fingertip forces ranging from 0.5 to 2 N during touchscreen interactions. (Asakawa et al., 2017; Kim et al., 2014, 2019). While providing 3D force data, their rigid structure and mounting constraints can interfere with natural hand posture. Kim et al. (2019) attached load cells to the back of a phone increasing the thickness of the device, altering the physical dimensions, thus likely affecting hand kinematics. Asakawa et al. (2017) fixed a tablet to a rigid platform, therefore restricting posture and movement of the participants' hand. These experimental constraints reduce the ecological validity of the measured fingertip forces.

Alternative methods, such as fingernail-mounted strain gauges, have been proposed to estimate both normal and tangential forces through nail deformation. Although this approach allows for more natural movements, it provides a measurement resolution of around 1 N, which is insufficient to accurately capture the fine-scale fingertip forces involved in smartphone interactions. Furthermore, the method is highly sensitive to finger geometry, nail curvature, and sensor placement, and its output can be distorted by slight changes in finger orientation (Popplewell et al., 2017).

Strain-gauge-based designs have been extended to hand and finger biomechanics. A study measuring repetitive tapping on a computer key switch used a two-axis strain-gauge transducer beneath the key surface to record vertical and sagittal forces (Jindrich et al., 2004). A planar three-degree-of-freedom sensor employing a fiberglass plate with paired strain gauges was developed to capture fingertip forces from patients of hand palsy with high sensitivity (2.564 mN), linearity, and low cost (350 US dollars) (Carducci et al., 2022). Another design features an L-shaped aluminium load cell with strategically positioned gauges to detect axial, bending, and torsional strains, enabling real-time thumb force measurement with approximately 2 % error (Acosta-Flores et al., 2024). These fixed experimental setups ensured stable force measurement conditions. However, smartphone interactions are inherently more dynamic, requiring users to hold and manipulate the device while applying fine-scale forces across multiple fingers and directions.

To realistically capture these forces, a custom force plate integrating strain gauges and replicating the size and weight of a standard smartphone would be ideal. Such a system enables quantification of finger-applied GRFs during natural smartphone use while maintaining ecological validity.

2.6.3. Custom force plate

Custom force plates have been widely applied in insect biomechanics, where forces in the micronewton range must be measured with high precision. Early designs, such as that of Heglund (1981), utilised orthogonal flexural beams with foil strain gauges to measure two force components with low crosstalk and high stiffness. The configuration provided high-frequency response and a simple calibration procedure, establishing the basis for later miniaturised systems. Subsequent developments extended the concept to a tri-axial plate with strain gauges mounted on orthogonal beams to measure normal and shear forces during gecko locomotion, and managed to capture rapid and transient forces (Autumn et al., 2006). Later developments enabled the acquisition of both tri-axial forces and their positional information by employing strain-gauge arrays and spatial calibration methods. A modular 16-tile force-measuring array was designed to resolve three-dimensional forces at millinewton resolution and frequencies above 200 Hz, allowing reconstruction of the magnitude and location of applied loads through matrix calibration and spatial mapping (Dai et al., 2011). An ultra-miniature tri-axial plate fabricated via stereolithography further demonstrated this capability, achieving sub-newton sensitivity, less than 2 % crosstalk, and eigenfrequencies exceeding 1 kHz (Reinhardt and Blickhan, 2013). Its calibration procedure enabled estimation of the centre of pressure, confirming the feasibility of simultaneously capturing the vector components and spatial distribution of reaction forces at micro-scale dimensions.

Across these studies, the mechanical structure amplifies applied loads into measurable strain, while strain gauges provide precise, stable, and economical signal transduction. These designs demonstrate that compact strain-gauged platforms can achieve accurate tri-axial force sensing with high temporal resolution, forming the basis for smartphone-scale applications.

2.7. Finite element analysis

2.7.1. Overview of finite element analysis applications in biomechanics

FE analysis is a numerical method for analysing the stress and strain of structures by solving partial differential equations derived from boundary conditions. Most FE analysis in MSk biomechanics has focused predominantly on the hip and knee because of their frequency of injury and disorders such as osteoarthritis, their relatively simple geometry, and extensive previous research regarding their loading conditions (Gíslason et al., 2010). Creation of an FE model consists of five main processes: image acquisition, image segmentation, meshing, assignment of material properties and application of boundary, including loading, conditions. Usually, the geometry of the structures of the joint is acquired from medical imaging. Image segmentation aims to separate the components of the joint under investigation from other bones or soft tissues in the scan. Surface meshing sections the surface of the objects of interest into small elements. This process can be carried out in the segmentation software. Then the surface mesh is imported into FE analysis software, where a volume mesh is created, material properties assigned, and boundary conditions applied (Gíslason et al., 2010; Kjartan and H., 2012; Peng et al., 2018).

Loading response is an important indicator for assessing the function of the joints. Few studies have investigated the loading response of the TMC joint during activities of daily living. Direct in vivo measurement of joint contact forces is typically achieved using instrumented implants, but such approaches are restricted to large joints such as the hip and knee and are limited to patients undergoing joint replacement (Bergmann et al., 2001; Damm et al., 2010; D'Lima et al., 2006) Owing to its small size, this approach is not applicable to the TMC joint. In addition, TMC ligaments have a layered, overlapping configuration, so the internal structures cannot be accessed until ligaments are sectioned (Bettinger et al., 1999; Rusli et al., 2021). Consequently, direct evaluation of the TMC joint loading response *in vivo* is not feasible.

Existing experimental approaches are limited to measurements of external forces, while internal joint reaction forces can only be estimated indirectly using inverse dynamics within MSk modelling frameworks. This inverse-dynamic approach has been used to estimate the resultant TMC joint reaction force during smartphone use; however, it provides no information on how this load is distributed across the articular surfaces and therefore cannot resolve cartilage stress or contact mechanics (Kim et al., 2019). FE analysis therefore provides a promising way to overcome these limitations by providing cartilage stress under realistic loading conditions.

2.7.2. Finite Element Modelling of the Trapeziometacarpal Joint

The TMC joint is challenging to model because of the complex bone geometry and soft tissue envelope. In addition, there is little literature about the loading conditions of wrist activities and the material properties of wrist ligaments and cartilage. However, several models have been attempted by other research groups. Gíslason et al. (2010) created a wrist complex FE model to examine how the load is transferred between the wrist joints during gripping. Bajuri et al. (2012) compared the stress distribution within healthy wrists and those with rheumatoid arthritis during gripping. Guo et al. (2009) applied a compressive load on the wrist model to investigate the contact force between the proximal row of the carpal bones and the radius. However, these models did not concentrate on the TMC joint, so loading conditions for thumb-involved activities were not specified or investigated.

More specific on the TMC joint, Schneider et al. (2017) developed population-based FE models from clinical CT-scan data to investigate sex and age differences in cartilage contact area and peak stress location during functional tasks, demonstrating that joint loading patterns vary between individuals. Similarly, Kurosawa et al. (2024) used FE modelling to reveal stress distributions in the articular surfaces during different thumb postures under static loading, providing insight into possible mechanisms of tissue

degeneration. Dong et al. (2023) developed a muscle-driven FE model of the thumb to study TMC joint mechanics during lateral pinch. The model revealed how changes in ligament or muscle function could reduce joint stress, highlighting the role of soft tissues in joint stability. However, it mainly focused on ligament functionality and surgical interventions rather than ergonomic strategies and the importance of the ligaments was not revealed in their models. To date, little relevant research has investigated the loading response of the TMC joint by FE analysis.

2.7.3. Modelling of Bone

2.7.3.1. Geometric Representation Modelling

Bones are the easiest joint component to image. Bone geometry in FE models is commonly segmented from high-resolution computed tomography (CT), therefore, the complex shapes of articular bone surfaces and epiphyses can be captured.

2.7.3.2. Material Properties

There are several common approaches to modelling the material properties of bone, depending on the study objective. The bone can be simplified as a rigid body to reduce computational cost, particularly in simulations where the primary interest is the mechanical response of the articular cartilage rather than bone deformation (Dong et al., 2023; Schneider et al., 2017; Willing et al., 2013). In many studies, bone is instead modelled as a linear elastic material defined by a Young's modulus and a Poisson's ratio, providing a straightforward approximation when the objective is to evaluate joint-level mechanics or overall load transfer (Incze-Bartha et al., 2023; Wei et al., 2020). More detailed representations separate cortical and trabecular bone into distinct regions with different material properties, approximating the cortex as a shell or a layer with a prescribed thickness (Kjartan and H., 2012; Zaharie and Phillips, 2018). To further reflect spatial heterogeneity, some models assign properties to each element based on

the CT Hounsfield unit values (Imai, 2015; Strack et al., 2024). In addition, bone could be described using non-linear constitutive behaviour or incorporating damage and failure criteria when the focus is on predicting fracture risk or localised failure (Soltani et al., 2024). In conclusion, the selection of an appropriate bone material representation is dependent on the research aim, requiring a balance between computational efficiency and the necessary level of physiological fidelity to address the intended biomechanical application.

2.7.4. Modelling of Articular Cartilage

2.7.4.1. Geometric Representation

Articular cartilage plays an important role in the study of joint mechanics. Its geometry in FE models is typically derived either from medical imaging or by idealised construction. In large joints such as the knee or hip, magnetic resonance imaging (MRI) or contrast-enhanced CT can directly visualise soft tissues adequately, providing a reference for the reconstruction of the cartilage (Anwar et al., 2020). In small joints where the resolution of cartilage in medical imaging is poor, researchers often create cartilage geometry by extruding a uniform-thickness layer from the articular surface of the bone. In the TMC joint, which has thin cartilage not visible adequately on regular CT or MRI, it is common to loft or offset the bony articular surfaces to form cartilage layers of assumed thickness (Dong et al., 2023; Kurosawa et al., 2024; Schneider et al., 2017; Valerio et al., 2024).

2.7.4.2. Material Properties

As 70-80% of cartilage is water, fluid exudation under load and reabsorption during unloading critically affect its stiffness, damping, and energy dissipation (Eschweiler et al., 2021). Dehydration leads to compaction and shrinkage of the solid matrix, which increases apparent stiffness. Therefore, its response depends on the interaction between

the solid matrix and interstitial fluid, making it time and strain-rate dependent (Han et al., 2018). Therefore, any FE model assuming purely elastic behaviour would fail to capture these fluid–solid coupling effects. A previous study reported that the homogeneous model overestimated the stress in healthy cartilage and underestimated them in degenerated regions, producing less accurate predictions of localised tissue loading (Lampen et al., 2021).

The material model of cartilage in FE models ranges from simple elastic solids to complex multiphasic models, depending on the study's objectives. When loading is sustained over time, biphasic models are advantageous because they treat cartilage as a fluid-saturated porous solid and capture the time-dependent transfer of load support from interstitial fluid pressure to the solid matrix. However, monophasic assumptions are still commonly used for static or instantaneous loading conditions, where the solid phase is described by nonlinear hyperelastic laws such as Ogden, and Mooney–Rivlin models (Brown et al., 2009; Mellors et al., 2023; Weizel et al., 2022).

2.7.5. Modelling of Ligaments

2.7.5.1. Geometric Representation Modelling

From section 2.3.2, there are seven ligaments resisting the movement of the first metacarpal: SAOL, DAOL, UCL, DRL, POL, IML and DIML, which were considered in previous FE models of the TMC joint (Dong et al., 2023; Synek et al., 2012; Valerio et al., 2024). There are several approaches of modelling ligaments in FE analyses. They can be categorised by model complexity as three-dimensional (3D), two-dimensional (2D), or one-dimensional (1D) representations.

3D elements enable anatomically realistic geometries, allowing ligament-bone contact interactions and wrapping behaviour around bony surfaces to be modelled. Therefore, it can capture local stress distributions and load transfer between ligaments and adjacent

tissues. In large joints, such as the knee, ligaments can be clearly identified in medical images, allowing their geometry to be segmented and modelled as 3D solid structures (Kiapour et al., 2013). For small joints, ligament geometry is difficult to define from medical images; therefore, their insertion sites are typically determined based on anatomical studies. In such cases, the 3D structure can be reconstructed using Boolean operations, simplified 3D solids, or a 3D truss network (Guo et al., 2009; Hamidrad et al., 2021; Marqués et al., 2022). 2D models represent ligaments as shell elements, which assume uniform ligament thickness and provide an intermediate level of structural detail and computational efficiency (Bruna-Rosso et al., 2016; Hamidrad et al., 2021).

Nevertheless, both 3D and 2D models suffer from several limitations. While complex constitutive laws such as hyperelasticity or viscoelasticity can be implemented in FE frameworks, these material definitions do not ensure physiologically realistic ligament behaviour. A key challenge lies in capturing ligament slackness and pre-strain, which strongly influence the transition from the toe-region to full load-bearing and represent a major source of uncertainty in ligament modelling (Esrafilian et al., 2020). Consequently, these approaches are computationally demanding and may still fail to fully represent the true mechanical behaviour of ligamentous tissue (Galbusera et al., 2014).

1D ligaments representation is the most common and computationally efficient method. Ligaments can be modelled as spring, beam, or truss elements, where nonlinear tension-only formulations accurately reproduce experimental force-displacement curves and pre-strain behaviour (Gislason et al., 2009; Synek et al., 2012; Wei et al., 2020). However, 1D models cannot represent transverse deformation, ligament wrapping, or local stress variations. They are therefore well suited for modelling They are therefore well suited for simulations in which joint kinematics are prescribed, for example when evaluating forces and contact mechanics at specific joint angles, where ligament deformations are relatively small and the detailed internal stress state of the ligament is not of primary interest.

In conclusion, when the FE study focuses on the stress distribution within the ligaments themselves, 3D models are more appropriate than 2D and 1D models. However, in studies primarily concerned with cartilage response, ligaments can be represented using 1D elements or, in some cases, even excluded entirely to improve computational efficiency without compromising the accuracy in cartilage mechanics (Sakuma et al., 2025).

2.7.5.2. Material properties

The stiffness of ligaments varies, even within the same joint. For example, in the TMC joint, the DRL exhibited a stiffness of approximately 89 ± 21 MPa, whereas the AOL showed values of 65 ± 30 MPa (D'Agostino et al., 2014; Nowalk and Logan, 1991). Furthermore, not all the TMC ligaments have been mechanically tested. The stiffness of the AOL, DRL and POL has been the focus of a few studies, but the reported results differed between studies (Table 2.3) (Bettinger et al., 2000; D'Agostino et al., 2014; Walker et al., 2025). In these studies, stiffness was defined as the slope of the linear portion of the force–displacement curve.

Ligament	Bettinger et al.	D'Agostino et al.	Walker et al.
AOL	24.1 ± 13.3	48.4 ± 23.1	57.9 ± 33.0
DRL	78.3 ± 21.9	117.3 ± 38.6	75.0 ± 36.5
POL	--	--	18.8 ± 11.8

Table 2.3 Stiffness (N/mm) of AOL, DRL and POL measured elsewhere (Bettinger et al., 2000; D'Agostino et al., 2014; Walker et al., 2025)

However, ligaments are hyperelastic tissues that exhibit nonlinear elastic behaviour; therefore, a single stiffness value cannot fully represent their mechanical response. Two previous FE models represented ligaments as linear elastic springs; one adopted the stiffness values measured by Bettinger et al. (Dong et al., 2023), while the other

estimated ligament stiffness through optimisation using the Levenberg–Marquardt algorithm to minimise the difference between experimental and simulated metacarpal displacements (Valerio et al., 2024).

Three FE models of the wrist joints have incorporated nonlinear formulations to capture the ligament's stress–strain relationship. Carrigan et al. (2003) developed a 3D FE model of the carpus to study load transmission pathways under static compressive loading in a neutral wrist posture. In this model, the relationship was defined by a piecewise nonlinear function that approximated physiological ligament behaviour. A parabolic toe region described the low-stiffness response for strains below 2%, followed by a linear region with constant stiffness between 2% and 5% based on experimentally derived stiffness values. For strains exceeding 5%, the stiffness was manually increased by a factor of ten to restrict excessive elongation and ensure computational convergence.

Gislason et al. (2009) developed a fully 3D FE model of the human wrist to investigate internal load transfer during maximal grip. In their model, the wrist ligaments were represented using nonlinear, tension-only spring elements in order to capture the characteristic toe-to-linear recruitment behaviour. The force-strain relationship was described as shown in Eq.2.1.

$$F = \begin{cases} \frac{a}{2\varepsilon_{ref}} \cdot x^2 & for\ 0 \le x \le \varepsilon_{ref} \\ ax - \frac{a\varepsilon_{ref}}{2} & for\ x > \varepsilon_{ref} \end{cases} \quad \text{Eq.2.1}$$

where a is a constant, F is the force, x is the strain, and ε_{ref} represents the nonlinear 'toe' region, which may extend to approximately 15% of the maximum strain. Beyond this threshold, the ligament response transitions into a linear region that persists until the maximum strain is reached.

Synek et al. (2012) proposed a multi-body simulation framework of the TMC joint, where joint motion was driven by forces from contact, ligaments, and muscles rather than assuming fixed rotational axes. In this model, ligaments were represented as tension-only spring elements, and their mechanical behaviour was defined using a quadratic elongation-based force law (Eq.2.2).

$$F = \begin{cases} \frac{CSA}{CSA_{avrg}} \cdot c \cdot (l - l_0)^2 & for\ l > l_0 \\ 0 & for\ l \leq l_0 \end{cases} \quad \text{Eq.2.2}$$

where CSA refers to the ligament's cross-sectional area; c is a stiffness constant of $7.5N/mm^2$; CSA_{avrg} is the averaged cross-sectional area of $7.27\ mm^2$; l is the ligament length, and l_0 is the initial length of the ligament.

2.8. Conclusion

This chapter presented the anatomy of the hand, and reviewed the biomechanics, and modelling approaches relevant to the TMC joint, highlighting its importance in the context of modern smartphone use. The literature demonstrated that the joint's exceptional mobility, while essential for thumb dexterity, also predisposes it to instability and degenerative changes under repetitive loading characterised by smartphone use.

Despite the growing prevalence of smartphone use, only few studies have quantified the joint loading environment of the TMC joint under smartphone-specific tasks. A further understanding of this relationship requires simultaneous kinematic and kinetic measurements, such that thumb motion can be directly related to the multidirectional forces applied at the thumb tip. While optical motion capture provides a reliable method

for capturing thumb kinematics, existing measurement solutions remain limited in their ability to capture the small-magnitude, multi-axis thumb tip forces generated during handheld device use. In particular, commercially available sensors often lack the required sensitivity, and they are unsuitable for integration within a realistic smartphone interaction, restricting their applicability for capturing physiologically realistic force data during naturalistic smartphone interaction.

Consequently, the development of a smartphone-sized, high-resolution, three-dimensional force measurement system, capable of synchronising with motion capture, is essential to enable realistic loading characterisation and to support subsequent FE modelling of the TMC joint. The following chapter describes the design, development and validation of a novel force plate specifically for measuring fingertip forces during smartphone tasks.

Chapter 3

A custom force plate for quantifying finger loading during smartphone activities

Building on the limitations identified in Chapter 2 regarding the measurement of small-magnitude fingertip forces during smartphone interaction, Chapter 3 presents the design, calibration, and validation of a custom force plate developed to quantify fingertip forces during smartphone use. The chapter begins by outlining the need for accurate measurement of small-magnitude finger forces in touchscreen interactions and the limitations of existing measuring methods. It then describes the mechanical and electrical design of a force plate closely matching both the size and weight of a smartphone. Finite element modelling is used to evaluate strain behaviour and natural frequencies to ensure dynamic stability during application. The chapter further details the calibration procedure for determining force magnitude and contact position, followed by experimental validation to quantify measurement accuracy. The chapter concludes with a discussion of the device performance, limitations, and its potential applications in hand biomechanics, musculoskeletal modelling, and ergonomic assessment of smartphone use.

The work presented in this chapter has been accepted to publish in *Frontiers in Bioengineering and Biotechnology*. The PhD candidate was responsible for the force plate design and validation, data analysis, and manuscript writing as first author.

3.1. Introduction

As established in Chapter 2, smartphone use has introduced repetitive, high-excursion thumb movements that concentrate mechanical loading at the trapeziometacarpal (TMC) joint (Canillas et al., 2014; Jonsson et al., 2007; Sampath et al., 2022). Quantifying the external fingertip forces generated during these interactions is therefore essential for understanding joint loading and for providing boundary conditions for MSk and FE models of the thumb. However, collecting kinetic data for the fingers remains challenging. Conventional commercial force plates used in biomechanics are primarily designed for recording ground-reaction forces during gait analysis and are too large and insufficiently sensitive for studying the fine forces applied during finger-based tasks (Bamberg et al., 2008; Benedetti et al., 1998; Kanai et al., 2008; Nagano et al., 2010).

Current approaches for measuring fingertip forces during touchscreen interaction have several limitations, including restricting physiological hand posture, and lacking the ability to capture both tri-axial force magnitude and accurate positional information simultaneously. Moreover, because a single sensor only reports the resultant force and moment at one point, at least three non-collinear load cells are required to measure both the fingertip force and its point of application (Wang et al., 2019). Beyond these mechanical constraints, 6-DoF load cells are expensive, typically costing on the order of USD 3,000–5,000 (Cao et al., 2021; Pérez Ubeda et al., 2018).

In response to these challenges, a custom-designed force plate could provide an effective alternative solution, as it can replicate the size and weight of a smartphone whilst enabling three-dimensional force measurement with positional information. Miniaturised strain-gauge-based force plates, originally developed and extensively validated in insect biomechanics, have demonstrated excellent performance for capturing small-magnitude forces with high sensitivity and low crosstalk (Dai et al., 2011; Fang et al., 2024; Heglund, 1981; Reinhardt and Blickhan, 2013). Building on these designs, this study proposes a novel force-plate design capable of capturing tri-

axial fingertip forces applied to a smartphone.

3.2. Material and method

3.2.1. Force plate design

To replicate the size and feel of a real smartphone, the force plate was designed to match the dimensions of a commercial device. Dimensions of 109 smartphones were sourced from three major manufacturers: Samsung, Apple, and Xiaomi. The iPhone 8, being approximately 10th percentile in size, was chosen as the starting point for this study. Upon successful implementation, any design of this size can be readily scaled to a larger size.

The force plate assembly was designed in SolidWorks (v2023, Dassault Systèmes, USA). It comprised five layers, whereby the loading cell was sandwiched between four components (Figure 3.1 and Table 3.1). The loading cell featured 12 spring beams; a strain gauge (350 Ω foil strain gauges, RunesKee, Shenzhen City Xinglinlieren Technology Co., Ltd, China) was mounted on each. The 350 Ω resistance was selected over the 120 Ω to reduce current flow and thereby minimise self-heating. Each strain gauge was dedicated to capturing forces primarily in one direction of a cartesian coordinate system that was aligned with the major axes of the assembly (Figure 3.1). As the resistance change of each strain gauge was small, the output voltage was amplified twice with a gain of 2000. Strain gauges can be affected by environmental factors such as temperature and humidity. To assess and correct for potential voltage drift due to temperature, the circuit was tested by running it for 30 minutes, monitoring the shift in output voltage. With five repeated tests, an increase of 0.0177 ± 0.0106 V was observed in the first 15 minutes, and the voltage remained stable thereafter, with a shift of 0.0013 ± 0.0032 in the second 15 minutes. A resistor was also added to the circuit to zero the voltage at the start of use, eliminating any resistance changes caused by storage conditions.

The interaction platform, where the fingers interact with the force plate during use, mimicked the touchscreen of the smartphone. Spacers were placed on either side of the loading cell to ensure that any force applied to the interaction platform was transferred fully to the central area of the loading cell. Only the two ends of the loading cell were supported, preventing the central portion from contacting the bottom plate. The gaps between the spacers allowed effective cable -routing.

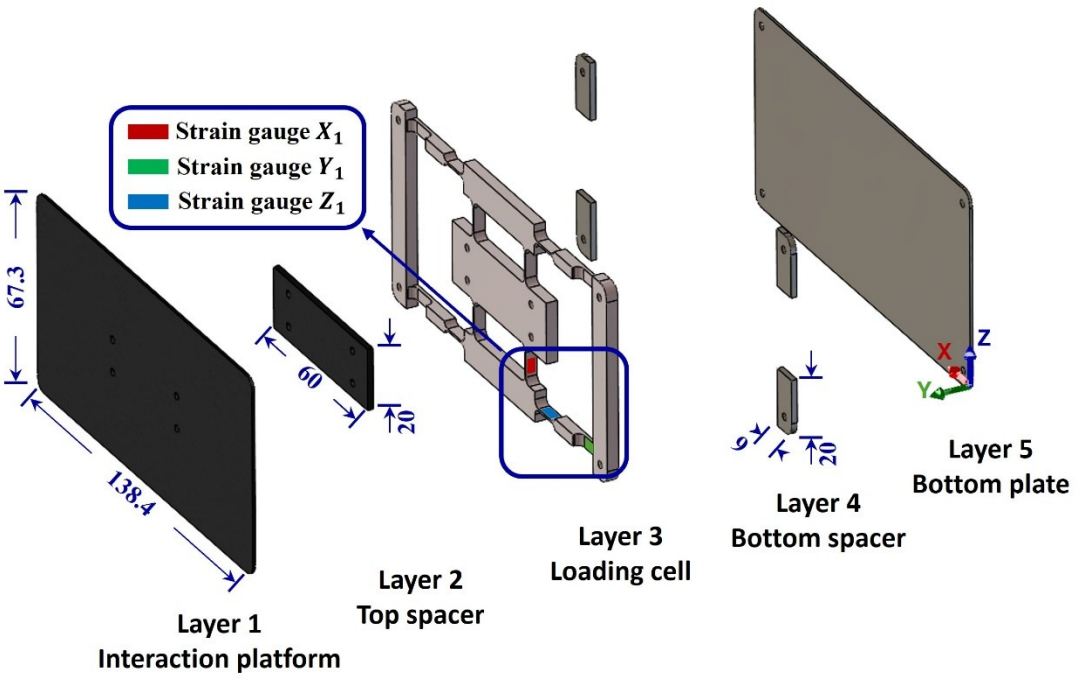
The interaction platform and adjacent spacers were made from carbon fibre, which was chosen for its lightweight properties and high stiffness. The loading cell was made from polycarbonate, which undergoes elastic deformation under typical touchscreen forces, ranging from 0.5 N to 3.5 N. The bottom plate and adjacent spacers were made from G304 stainless steel to add weight and enhance the stability of the assembly. The total weight of this design was 145.3 g, closely matching the weight of the iPhone 8 (148 g). The interaction platform, bottom plate, and spacers were cut using a ProtoMAX waterjet cutter (OMAX Corporation). The loading cell was cut and milled using a flat-bed CNC router (AXYZ Infinite 4008 series, AXYZ International Inc.).

In order to assess the ability of the force plate to meet its intended accuracy in recording force magnitude and location, (a) a modal FE analysis was conducted to ensure that natural frequencies would not affect the recordings, (b) calibration to link strain-gauge outputs with force magnitude and location was carried out, and (c) test for validation - confirmation of the accuracy of the force plate's recordings - was conducted whereby the force plate recordings were compared with those of a uniaxial testing machine. This process is illustrated in a flowchart (Figure 3.2).

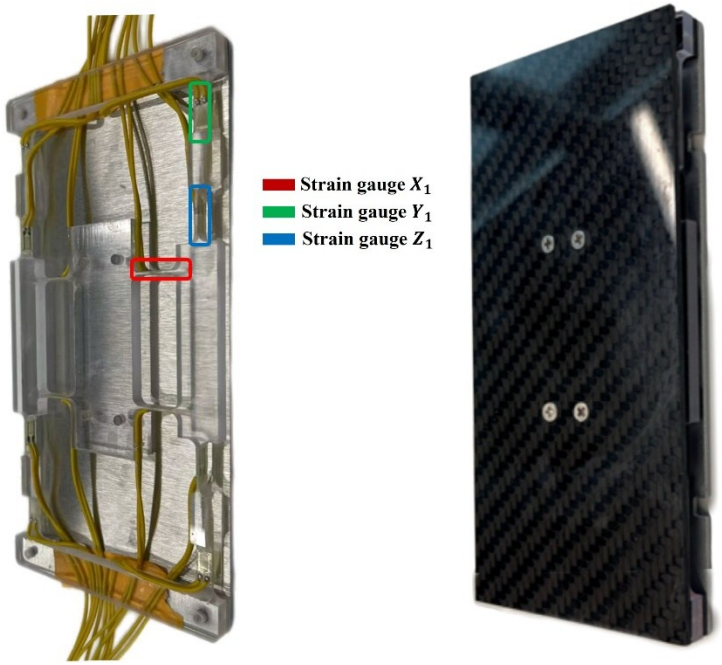
Layer	Layer 1 Interaction platform	Layer 2 Spacer	Layer 3 Loading cell	Layer 4* Spacer	Layer 5 Bottom plate
Width (mm)	67.3	20	67.3	9	67.3
Length (mm)	138.4	60	138.4	20	138.4
Thickness (mm)	1	2	4	2	1.2

Table 3.1 Dimensions (mm) of the force plate assembly. * Layer 4 consists of 4 identical sections; the dimensions shown are for one piece.

+



(a)



(b)

Figure 3.1 (a) Exploded schematic of force plate assembly also showing the positions of three of the strain gauges, X_1, Y_1 and Z_1 , in one quarter of the plate. All dimensions shown are in mm. (b) Photograph of the internal structure and external appearance of the force plate.

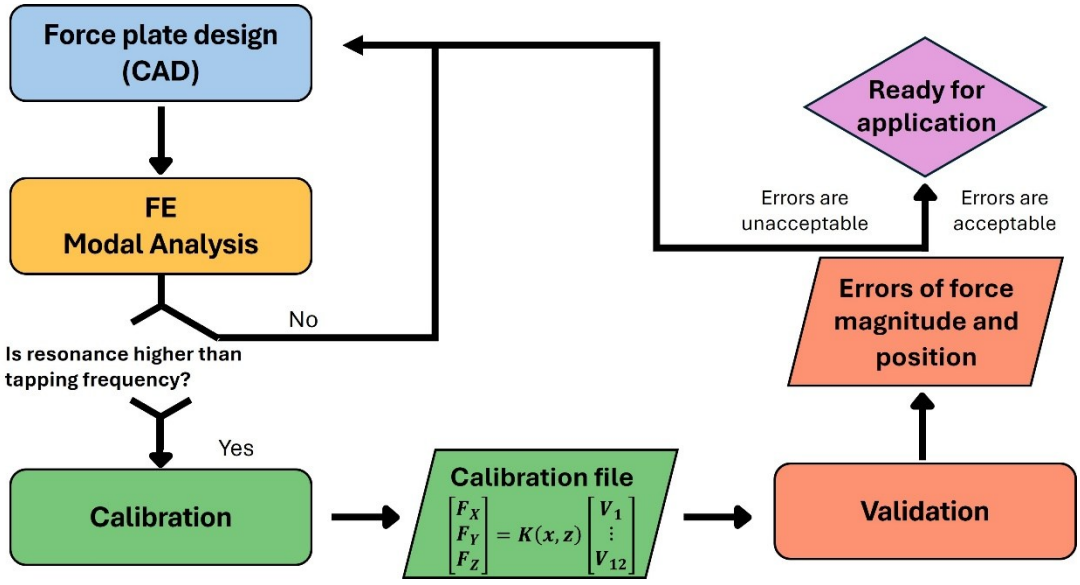


Figure 3.2 Flowchart of the methodology

3.2.2. Structural and modal analysis

To aid in the design of the force plate, an FE model was developed in Abaqus (v2020, SIMULIA, Dassault Systèmes, France). The FE model had two objectives: the first was to verify that the strain in the spring beam is sufficiently large and exhibits a linear relationship with the applied force and position; and the second was to analyse the natural frequency to ensure that resonance does not compromise the measurements of the force plate. The model only incorporated the interaction platform, top spacer and loading cell; the bottom spacer and bottom plate were simplified as fixed boundary conditions since they only provided support and were expected to not deform during use. The four corner holes on the load cell layer were fully constrained to represent the physical mounting of the force plate to a rigid base. Four central holes on layers 1, 2 and 3 were connected as rigid bodies, and the contact between each layer was modelled as smooth (no friction) and hard (no penetration). The model was meshed with 20-node quadratic brick elements with reduced integration (type C3D20R). A sensitivity

analysis determined that a 0.5 mm element-edge size was sufficient, whilst a finer mesh was applied to the spring beams, where strain gauges were to be mounted, ensuring a minimum of four finite elements through the thickness. All materials were assumed to be linearly elastic and isotropic; (G304) stainless steel: Young's modulus, E = 190 GPa, Poisson's ratio $\nu = 0.27$, mass density $\rho = 7.9$ g/cm^3; carbon fibre: E = 243 GPa, $\nu = 0.27$, $\rho = 1.8$ g/cm^3; polycarbonate: E = 2.4 GPa, $\nu = 0.36$, $\rho = 1.2$ g/cm^3.

To confirm the capability of the spring beams to generate measurable strain responses in each axis, a unit load of 1 N was applied at the centre of the force plate sequentially along the X, Y, and Z directions to evaluate their deformation behaviour under directional loading.

Smartphone activities, such as typing, involve repetitive interaction with the touchscreen. To ensure that resonance would not affect the performance of the force plate, its natural frequency needed to be compared with the typical frequency of smartphone users touching the screen. Modal analysis was conducted to determine the natural frequency of the force plate. Since no existing literature provided data on typing frequency, ten frequent smartphone users, each with a screen time of over four hours per day, were recruited. They were asked to type a message as quickly as possible, and their frequency was calculated by dividing the number of letters typed by the time taken in seconds. This part of the study received ethical approval from the Research Governance and Integrity Team (Imperial College Research Ethics Committee Reference Number: 6455822)

3.2.3. Calibration

Force plate calibration is necessary to determine the linear matrix transformation (Eq.3.1 and Eq.3.2) that relates strain gauge outputs to the force vector applied to the interaction platform (Dai et al., 2011; Reinhardt and Blickhan, 2013; Schrand, 2007).

$$\begin{bmatrix} F_X \\ F_Y \\ F_Z \end{bmatrix} = K(x, z) \begin{bmatrix} V_1 \\ \vdots \\ V_{12} \end{bmatrix} \quad \text{Eq. 3.1}$$

$$\begin{bmatrix} V_1 \\ \vdots \\ V_{12} \end{bmatrix} = [V_i]_{i=1}^{12} = K^{-1} \begin{bmatrix} F_X \\ F_Y \\ F_Z \end{bmatrix} \quad \text{Eq. 3.2}$$

where F_X, F_Y and F_Z are the three components of the applied force, V_i is the voltage of strain gauge i; and K is the characteristic matrix; the inverse of K (K^{-1}) is termed the sensitivity matrix.

Although each spring beam was designed to respond primarily to forces in its designated axis direction, crosstalk was inevitable. Crosstalk was accounted for by treating the output voltage of each strain gauge as a combination of three components, reflecting the influence of forces from different directions (Eq.3.3). K^{-1} was obtained through regression analysis of the applied load magnitude and position against the output voltage of strain gauges, which was expressed in terms of x and z (Eq.3.4).

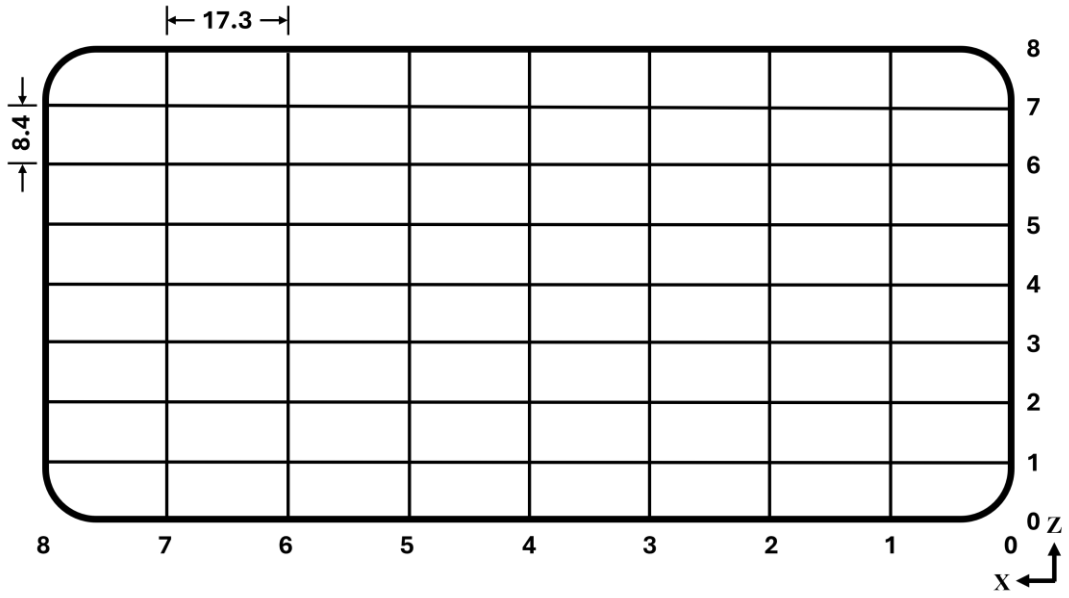
$$V_i = (\gamma_{iX} z + c_{iX}) F_X + (\alpha_{iY} x + \gamma_{iY} z + c_{iY}) F_Y + (\alpha_{iZ} x + c_{iZ}) F_Z \quad \text{Eq.3.3}$$

$$K^{-1} = [\gamma_{iX} z + c_{iX} \quad \alpha_{iY} x + \gamma_{iY} z + c_{iY} \quad \alpha_{iZ} x + c_{iZ}]_{i=1,\dots,12} \quad \text{Eq.3.4}$$

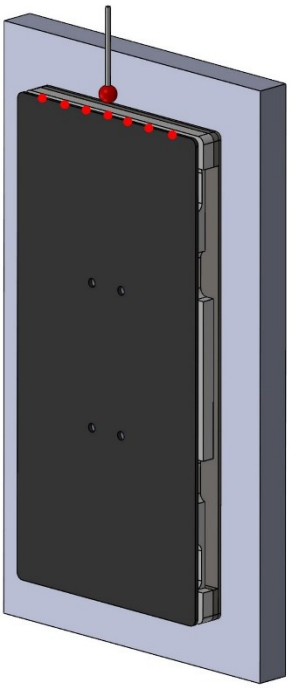
Coefficients α_{iY}, α_{iZ}, γ_{iX}, γ_{iY}, c_{iX}, c_{iY}, and c_{iZ} were associated with strain gauge i and can be determined through calibration tests. Specifically, regression analyses were conducted between the applied forces and output voltages, followed by a second regression analysis between the positions of load application and output voltages. The coefficients were derived from the results of these regression analyses.

To establish the relationship between the output voltage of strain gauges and the magnitude and position of an applied force, forces were applied separately in each of X, Y, and Z directions at regularly spaced positions on the interactive platform. A materials testing machine (MACH-1, Biomomentum Inc., Laval, Canada), equipped with a 10 N single-axis load cell and a 5 mm indenter (Figure 3.3) was used to apply forces in a grid pattern with spacings of 17.3 mm along the X-direction and 8.4 mm along the Z-direction (Figure 3.3a). Forces ranging from 0.5 N to 3.5 N were applied in the X direction at seven positions (Figure 3.3b); in the Y direction (normal to the interaction platform) at 49 positions (Figure 3.3d); and in the Z direction at seven positions (Figure 3.3c). This force range was based on the reaction forces observed during touchscreen use (Asakawa et al., 2017; Kim et al., 2019). The strain-gauge output voltage was collected using the cRIO-9048, module NI-9205, and LabVIEW (National Instrument, Texas, United States). The data were post-processed and visualised in MATLAB (v.R2024b, MathWorks, Massachusetts, United States).

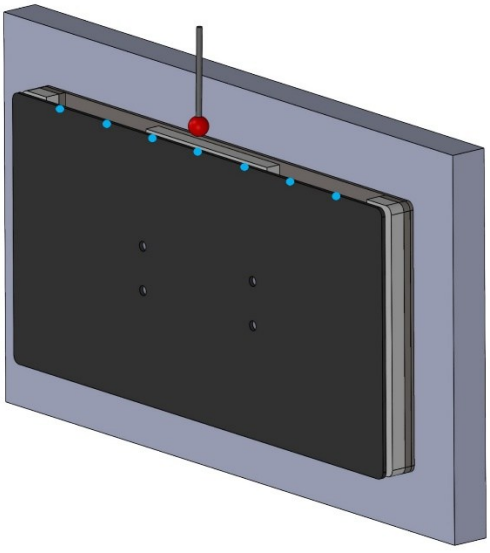
Solving an algebraic system of five-variable nonlinear equations with quadratic terms requires only five independent equations to determine the variables (F_X, F_Y, F_Z, x and z). In this study, each strain gauge provides one independent equation; therefore, although 12 strain gauges were installed, only five were needed and used to solve for the unknown coefficients. The combination of the five strain gauges with the highest coefficient of determination (R^2) was selected to calculate the force's magnitude and position. The correct solution was identified by constraining the range of F_X, F_Y, F_Z, x and z, as well as cross-checking the results with solving using other five-strain gauge combinations. The redundancy of the strain gauges enabled cross-validation of the results, optimisation of the gauge combination, and accounted for potential gauge failures or malfunctions, ensuring reliable measurements.



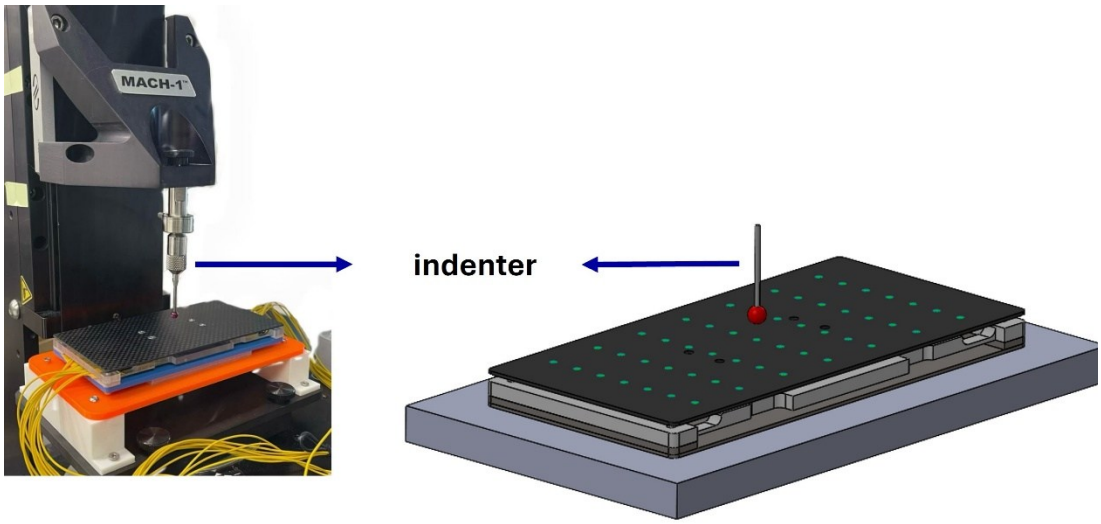
(a)



(b)



(c)



(d)

Figure 3.3 (a) Calibration grid on interaction platform. Calibration in (b) X direction, (c) Z direction, and (d) Y direction. Calibrations were run by applying a force of 0.5 to 3 N in each of X, Y, and Z directions at each position indicated by red, green and blue dots respectively on the interaction platform. All dimensions shown are in mm.

3.2.4. Accuracy

The MACH-1 system was used to assess the accuracy of the force plate in measuring both the magnitude and position of applied forces.

The bottom plate of the force-plate assembly was mounted on a sloped platform angled at 15° (Figure 3.4a). Within the plane of the sloped surface, the force plate was orientated at 0°, 45°, and 90° (Figure 3.4b), enabling simultaneous application of normal and shear forces. Static forces of 1, 2, and 3.5 N were applied at nine designated positions on the plate (Figure 3.4c) per orientation using a 5 mm diameter spherical indenter.

The measurement error was defined as the difference between the value measured by the MACH-1 and the value measured by the force-plate assembly. A total of 792

combinations of five strain gauges were evaluated in their ability to measure accurately magnitude and position of the applied force. The selection criteria for an optimal set focused on minimising estimation errors in the force components (F_X, F_Y and F_Z) and position coordinates (X and Z). Combinations with force-estimation errors within ±0.15 N and positional errors in the X and Z directions within ±2.5 mm were set as thresholds. Furthermore, the overall positional deviation, defined as the absolute distance between the actual and estimated positions, was required to remain below 3 mm.

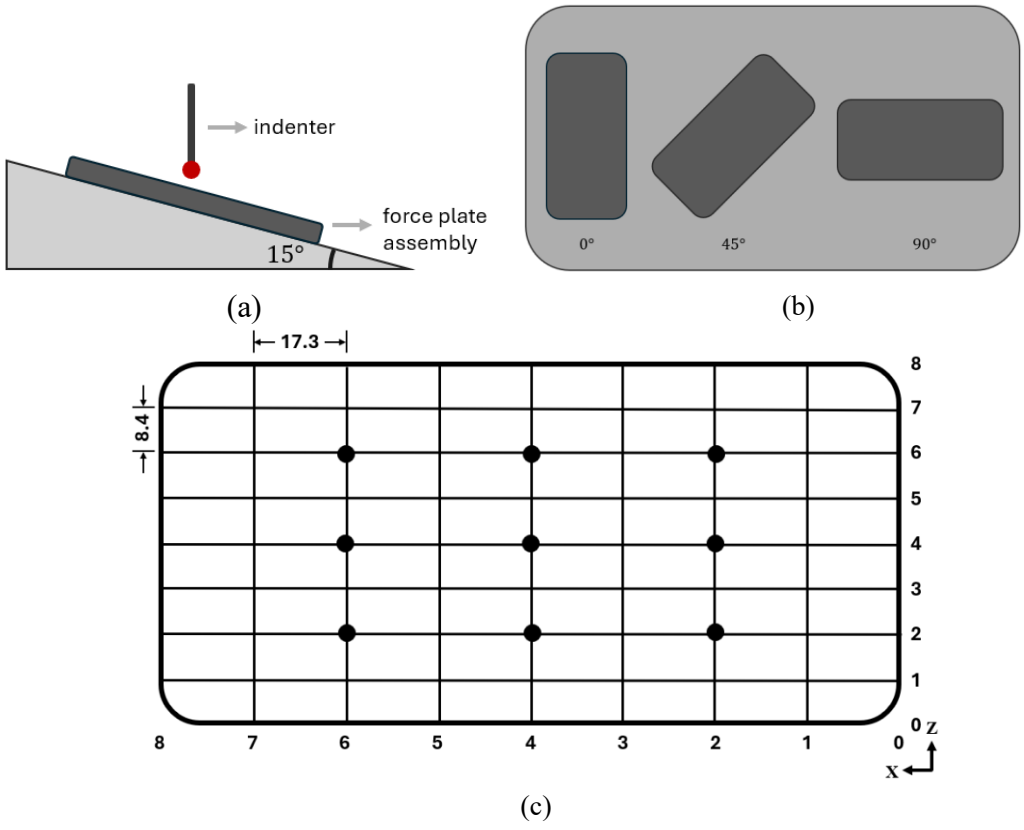


Figure 3.4 Test setup to determine force plate accuracy: (a) diagrammatic side view of the setup; (b) in-plane view of the sloped surface; (c) positions of load application on the surface of the interaction platform

3.2.5. Dynamic validation

To evaluate the stability and repeatability of the force plate under dynamic loading, a cyclic test was performed using the MACH-1 system. A sinusoidal force 3.5 N in amplitude was applied for 1000 consecutive cycles at a frequency of 3 Hz, corresponding to the average tapping frequency during smartphone use, at three representative positions on the interaction platform (Figure 3.5) to account for spatial variability. The force measured by the force plate was compared with the reference force recorded by the MACH-1 system across the 1000 cycles.

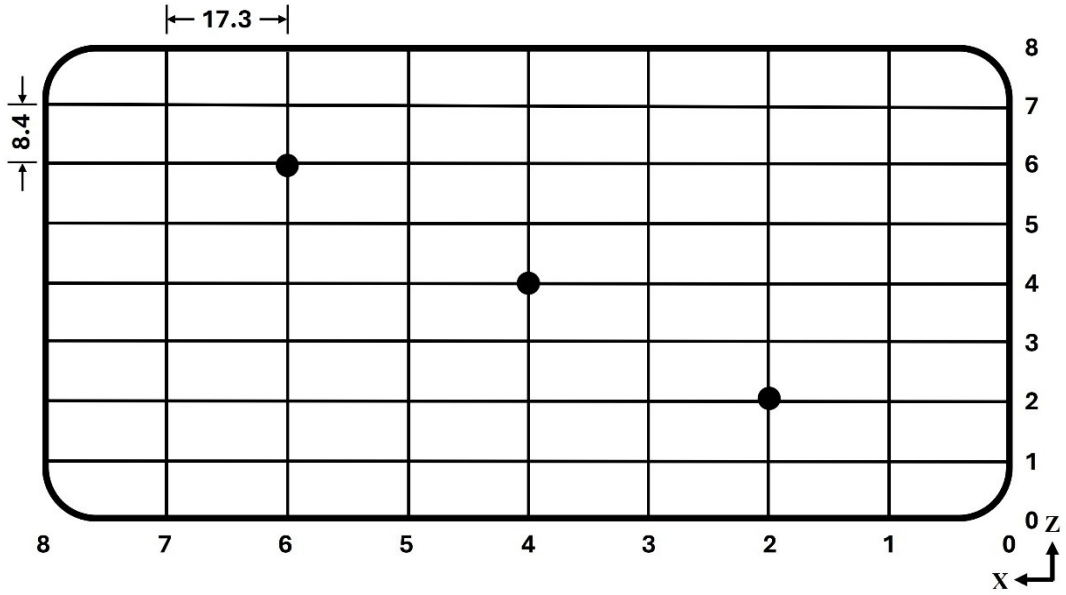


Figure 3.5 Diagram showing the three locations on the interaction platform used for the cyclic loading test.

3.3. Results

3.3.1. Natural frequency

The average frequency with which participants touched the screen of their smartphones during rapid typing was 2.7 ± 0.7 Hz (mean ± SD) (Figure 3.6). The first six modes of

the modal analysis were an order of magnitude higher than the frequency with which participants were tapping the screen, and so the effect of resonance on the loading plate was deemed minimal (Table 3.2).

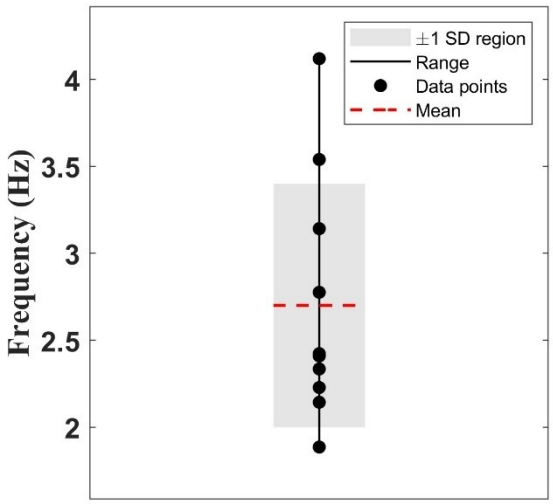


Figure 3.6 Tapping frequency of 10 participants

Mode	Frequency (Hz)	Associated motion
1	47	oscillatory translation along X-axis
2	52	oscillatory translation along Z-axis
3	64	oscillatory rotation about the X-axis
4	70	oscillatory rotation about the Z-axis
5	80	oscillatory rotation about the Y-axis
6	84	oscillatory translation along Y-axis

Table 3.2 Natural frequencies of the design determined by finite-element modal analysis

3.3.2. Calibration

In both the experimental and FE models, the resultant strain displayed a linear relationship with force (Table 3.3). K^{-1} was obtained through regression analysis;

Eq.3.5 shows the K^{-1} for the load case at the centre ($x = 4, y = 4$).

$$\begin{bmatrix} V_1 \\ V_2 \\ V_3 \\ V_4 \\ V_5 \\ V_6 \\ V_7 \\ V_8 \\ V_9 \\ V_{10} \\ V_{11} \\ V_{12} \end{bmatrix} = \begin{bmatrix} -0.393 & -0.033 & -0.051 \\ -0.524 & -0.037 & 0.103 \\ 0.133 & -0.027 & -0.021 \\ 0.294 & -0.023 & 0.015 \\ -0.035 & 0.316 & -0.110 \\ -0.028 & 0.336 & 0.168 \\ 0.017 & 0.264 & -0.073 \\ 0.020 & 0.193 & 0.026 \\ -0.021 & -0.070 & -0.369 \\ -0.068 & -0.207 & 0.613 \\ 0.006 & -0.106 & -0.666 \\ 0.054 & -0.202 & 0.553 \end{bmatrix} \begin{bmatrix} F_X \\ F_Y \\ F_Z \end{bmatrix} \quad \text{Eq.3.5}$$

The relationship between the positions where the load was applied and output voltage of each strain gauge was expected to be linear. The coefficients of determination (${R_{F_{m,n}}}^2$) quantify the goodness of fit in the regression model relating output voltage to the load position, n, which represents a spatial variable that may vary along the X-direction, Z-direction, or across the XZ-plane, under an applied force in direction m (Table 3.4).

Strain gauge	β_{F_X}	Crosstalk %	${R_{F_X}}^2$	β_{F_Y}	Crosstalk %	${R_{F_Y}}^2$	β_{F_Z}	Crosstalk %	${R_{F_Z}}^2$
X_1	-0.393	NA	0.999	-0.033	6.92	0.990	-0.051	10.69	0.990
X_2	-0.524	NA	0.997	-0.037	5.57	0.996	0.103	15.51	0.933
X_3	0.133	NA	0.998	-0.027	14.92	0.999	-0.021	11.60	0.991
X_4	0.294	NA	0.996	-0.023	6.93	0.997	0.015	4.52	0.968
Y_1	-0.035	7.59	0.991	0.316	NA	0.994	-0.110	23.86	0.999
Y_2	-0.028	5.26	0.953	0.336	NA	0.996	0.168	31.58	0.988
Y_3	0.017	4.80	0.980	0.264	NA	0.994	-0.073	20.62	0.988
Y_4	0.020	8.37	0.991	0.193	NA	0.996	0.026	10.88	0.997
Z_1	-0.021	4.57	0.989	-0.070	15.22	0.999	-0.369	NA	0.999
Z_2	-0.068	7.66	0.998	-0.207	23.31	0.999	0.613	NA	0.996
Z_3	0.006	0.77	0.756	-0.106	13.62	0.999	-0.666	NA	1.000
Z_4	0.054	6.67	0.992	-0.202	24.97	0.997	0.553	NA	0.999

Table 3.3 Regression coefficients and crosstalk of strain gauges. Regression coefficient β

represents the sensitivity of each strain gauge to applied forces F_X, F_Y and F_Z on the centre (x=4, z=4). Crosstalk (%) is calculated as the ratio of β in one direction to the sum of β across all directions, indicating the relative contribution of each force component to the total output. R^2 denotes the coefficient of determination for each regression model. NA=Not Applicable.

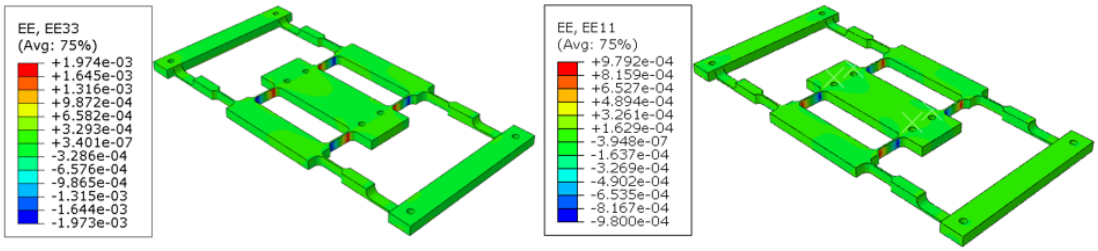
Strain gauge	γ_{iX}	c_{iX}	${R_{F_{X,z}}}^2$	α_{iY}	γ_{iY}	c_{iY}	${R_{F_{Y,xz}}}^2$	α_{iZ}	c_{iZ}	${R_{F_{Z,x}}}^2$
X_1	0.086	-0.727	0.99	-0.033	0.012	0.042	0.89	-0.207	0.773	1.00
X_2	-0.095	-0.156	1.00	-0.041	0.005	0.109	0.97	0.225	-0.786	1.00
X_3	-0.025	0.224	0.98	0.000	-0.009	0.052	0.74	0.061	-0.260	1.00
X_4	0.055	0.043	1.00	0.024	-0.015	-0.079	0.96	-0.123	0.497	1.00
Y_1	0.018	-0.108	1.00	-0.104	-0.079	1.048	1.00	-0.027	0.219	1.00
Y_2	-0.010	0.024	0.80	-0.119	0.094	0.422	1.00	0.039	-0.318	0.99
Y_3	-0.006	0.04	0.86	0.090	-0.059	0.123	1.00	0.020	-0.008	0.97
Y_4	0.004	0.01	0.61	0.083	0.052	-0.358	0.99	-0.020	0.014	1.00
Z_1	-0.034	0.144	0.98	-0.032	0.008	0.018	0.98	0.082	-0.703	1.00
Z_2	0.053	-0.294	1.00	0.017	-0.040	-0.113	0.98	-0.108	1.087	1.00
Z_3	0.067	-0.262	1.00	0.021	0.003	-0.196	0.88	-0.113	-0.203	1.00
Z_4	-0.050	0.263	1.00	-0.022	-0.038	0.037	0.99	0.080	0.215	0.96

Table 3.4 Coefficients of determination, ${R_{F_{m,n}}}^2$, of the regression between β_F and coordinates

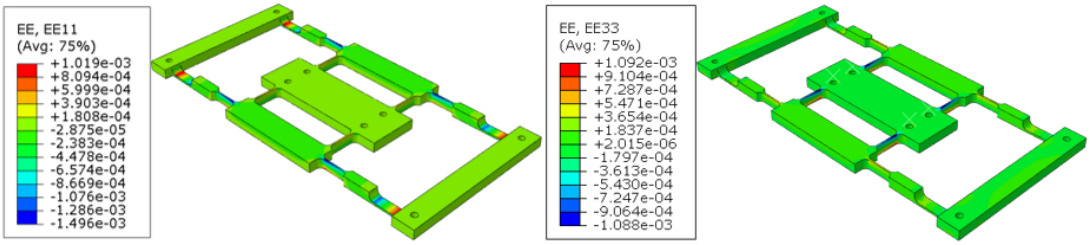
The strain distribution in the spring beams under unit loading in the X, Y, and Z directions is shown in Figure 3.7. The strain gauges were configured to measure different normal strain components, with the strain gauge X capturing ε_{33} (normal strain along the Z-axis), while strain gauges Y and Z primarily captured ε_{11}(normal strain along the X-axis).

When loads were applied in the Y and Z directions, noticeable ε_{11} responses were observed in strain gauges Y and Z, respectively. However, $\varepsilon_{11}$was also detected in strain gauge Y when a load was applied in the Z direction, and in strain gauge Z when

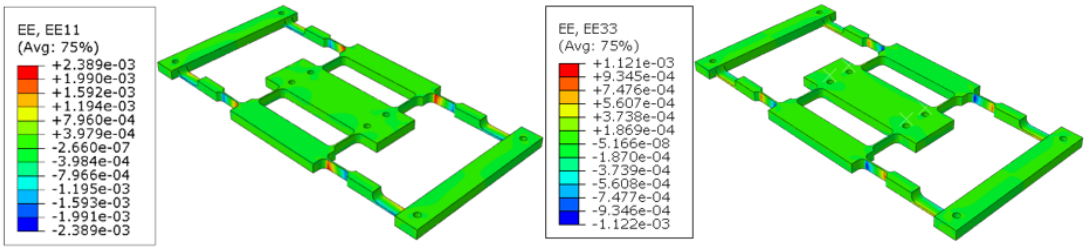
a load was applied in the Y direction (Figure 3.7c). This indicates the presence of crosstalk between the measurement channels in the current load-cell structure.



(a)



(b)



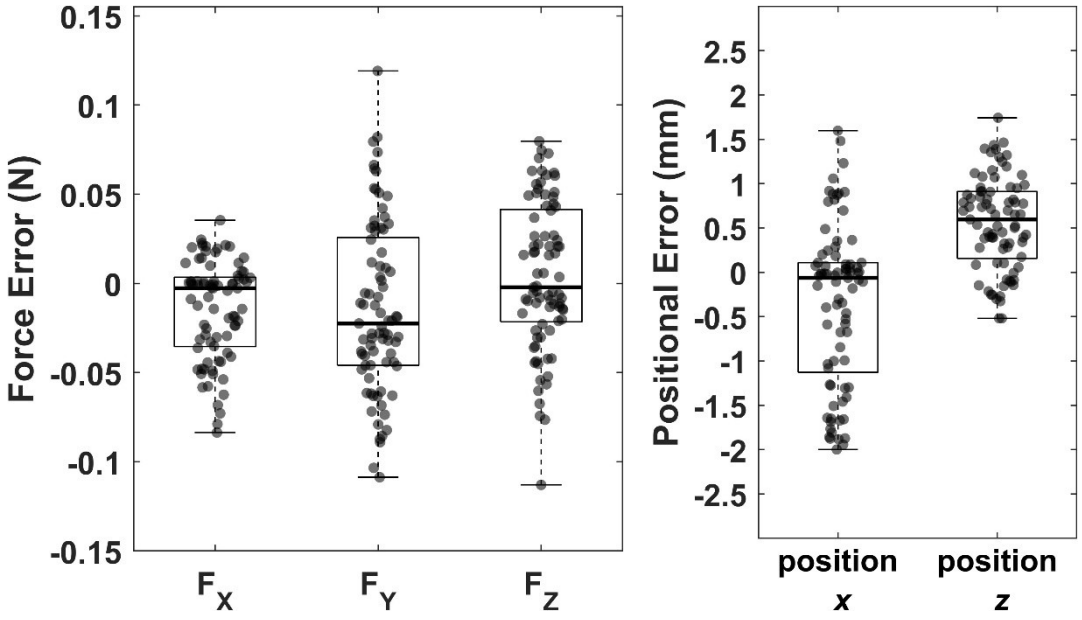
(c)

Figure 3.7 Strain EE_{11} (along X direction) and EE_{33} (along Z direction) in the loading cell under a 1-N force applied at central point (x=4, z=4) in (a) X, (b) Y and (c) Z directions

3.3.3. Accuracy

Five combinations of strain gauges were identified as meeting the accuracy criteria set. Figure 3.7 illustrates the error in predicting force and position using one such

combination consisting of strain gauges X_3, Y_2, Y_3, Y_4, and Z_4. The maximum, mean, and minimum errors in the predicted forces and positions are summarised in Table 3.5. The remaining combinations that satisfied the selection criteria are presented in the Appendix (Figure A.2). Any of the five identified combinations were thus deemed eligible to be used as the calibration file for measurement.



(a) (b)

Figure 3.8 Error between (a) magnitude of applied and measured force; (b) position of applied and measured position.

Combination		F_x (N)	F_y (N)	F_z (N)	x (mm)	z (mm)
X_2, Y_1, Y_2, Y_4, and Z_4	max	0.048	0.109	0.082	1.250	2.532
	mean	-0.012	-0.029	-0.001	-0.515	0.740
	min	-0.069	-0.108	-0.095	-2.277	-0.495
	SD	0.025	0.042	0.044	0.907	0.856

X_3, Y_1, Y_3, Y_4, and Z_3	max	0.023	0.119	0.143	2.370	0.543
	mean	-0.011	-0.029	0.039	-0.088	-0.096
	min	-0.059	-0.095	-0.031	-2.189	-1.363
	SD	0.023	0.042	0.050	1.456	0.347
X_2, Y_2, Y_3, Y_4, and Z_4	max	0.016	0.121	0.080	1.618	1.638
	mean	-0.014	-0.014	0.000	-0.375	0.576
	min	-0.065	-0.109	-0.099	-2.175	-0.279
	SD	0.021	0.048	0.044	0.937	0.502
X_3, Y_2, Y_3, Y_4, and Z_4	max	0.035	0.119	0.080	1.597	1.742
	mean	-0.015	-0.015	0.003	-0.374	0.581
	min	-0.084	-0.109	-0.113	-1.999	-0.256
	SD	0.028	0.049	0.043	0.890	0.510
X_4, Y_2, Y_3, Y_4, and Z_4	max	0.036	0.121	0.123	1.562	1.668
	mean	-0.015	-0.017	0.008	-0.333	0.527
	min	-0.132	-0.134	-0.097	-2.089	-0.224
	SD	0.036	0.052	0.048	0.914	0.469

Table 3.5 Maximum (max), mean, minimum (min) values and standard deviation (SD) of the error in predicting tri-axial force and position across selected strain gauge combinations.

3.3.4. Dynamic validation

Under sinusoidal loading at 3 Hz, the force measured by the force plate closely matched the reference force recorded by the MACH-1 system throughout the 1000-cycle test at each of the three loading positions. Figure 3.8 illustrates a representative comparison between the applied force and the force measured by the force plate at the centre ($x = 4, y = 4$). Across all cycles and positions (3000 cycles in total), the difference between the amplitude of the applied and measured force was 0.044 ± 0.036 N. Stability was further evaluated by comparing the zero-load voltage averaged over 5 s before testing

with that measured over 5 s after the 1000 loading cycle tests. The resulting voltage difference was 0.0083 ± 0.0048 V across the 12 strain gauges, indicating negligible drift.

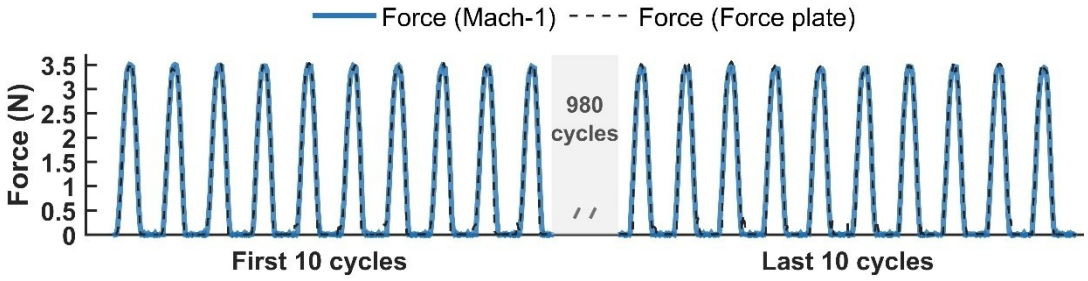


Figure 3.9 Comparison of the force recorded by the MACH-1 system (solid line) and the force measured by the force plate (dashed line) under sinusoidal loading at 3 Hz over 1000 cycles.

3.4. Discussion

This study presented the design of a force plate capable of measuring magnitude, direction and position of the force applied by fingers during smartphone use.

The high R^2 values indicate a strong linear relationship between output voltage and applied force (Table 3.4), confirming the effectiveness of the force-plate assembly. Crosstalk between force directions was expected and observed. When the force was applied at the centre, regression analysis (Table 3.4) revealed that each strain gauge was most responsive to its primary force direction. Strain gauge X_i exhibited crosstalk from force components F_Y and F_Z, with crosstalk effect below 15.5%. Strain gauges Y_i and Z_i exhibited crosstalk between F_Y and F_Z, with crosstalk ranging from 10.9% to 31.6%.

Crosstalk was more pronounced under eccentric loading conditions. For example, when a force was applied at position ($X = 6,\ Z = 4$), β_{F_Z} of strain gauge X_1 increased to

0.7, indicating a strong influence from an off-axis force component. This effect is particularly critical for force plates with a large surface area, where off-centre loads are likely and can lead to increased measurement inaccuracies. In the present design, crosstalk was not treated as noise but rather incorporated into the calibration process. Each strain gauge, although sensitive primarily to one force direction, responds to forces applied along other axes. To account for this behaviour, each gauge was calibrated under forces applied in all three directions, allowing the influence of each force component on every gauge to be quantified. The resulting sensitivity matrix therefore represents the combined effect of all directional components, enabling accurate multi-axial force reconstruction and effective compensation for crosstalk.

For the top five combinations of strain gauges used to achieve calibration, the measurement error for F_x, F_y and F_z was deemed adequate for the intended application of a target force range of 0 – 3.5 N, with the error values within ±0.15 N. The force plate was calibrated for forces up to 3.5 N, covering the typical force range applied by fingers during smartphone use (Asakawa et al., 2017; Kim et al., 2019). The loading cell never made contact with the bottom plate for forces below 3.5 N. In additional tests, with Y forces that reached 5 N, the loading cell made contact with the bottom plate, but remained deformed within its elastic region, meaning that the maximum load limit of the load cell was not reached. As a result, the design has the potential to measure forces of up to 5 N. Further tests are required to identify the load limit of the loading cell and to ascertain whether the calibration presented here is still valid.

For position measurements, the error in the Z coordinate ranged from –1 mm to 2.5 mm, while the error in the X coordinate ranged from –2 mm to 1.5 mm. The absolute positional deviation varied between 0.3 mm and 3 mm, indicating a high level of positional accuracy, particularly when considering that the diameter of the indenter used during testing was 5 mm. However, the indenter size could introduce uncertainty in contact location, contributing to positional deviations. Improved accuracy could be

achieved with a smaller indenter. Previous studies reported fingertip contact areas of approximately 60-80 mm² under a normal force of approximately 0.5 N, corresponding to a contact diameter of 9 mm (Dzidek et al., 2017; Logozzo et al., 2022). Considering that the typical fingertip force during smartphone use ranges from 0.5 N to 2.6 N and that contact area at the fingertip would normally increase with load, the 0.5 N condition represents a conservative lower bound for realistic interactions. Therefore, even under this minimum loading scenario, the positional error observed in our system (≤3 mm) remains comfortably within the fingertip contact region. Positional data were not used in subsequent analyses, as the primary focus was on force measurement. Therefore, the achieved accuracy is deemed sufficient for this study, although improved calibration may enhance future performance.

The tapping frequency analysis was based on a relatively small sample size (n = 10), which may have limited the generalisability of the observed variability in tapping dynamics. The maximum measured tapping frequency (4.2 Hz), however, was one order of magnitude lower than the lowest resonance frequency of the force plate (47 Hz) and so individual variability and potential outliers present a negligible risk of interference with the force recordings.

Validation was performed under static, controlled loading conditions rather than during dynamic smartphone interactions such as tapping or swiping, which may involve transient or impact forces. Further, the maximum tested load range extended to 5 N, while calibration validity beyond 3.5 N was not conducted; further work is required to confirm linearity and structural stability for forces greater than 3.5 N. Lastly, the current prototype has not been evaluated yet for long-term durability or performance under repetitive use, which may be needed to assess when recalibration may be necessary. Addressing these aspects in future work will strengthen the robustness of the design and broaden its applicability.

The force plate presented here can now be integrated with a motion capture system to

study the kinematics and kinetics of the hand when executing common smartphone activities. Such data can help smartphone design and ergonomics, such as in the study by Xiong and Muraki, (2014), whereby thumb-muscle workload varied significantly with button size and thumb movement orientation; fingertip force data from our device could directly inform considerations of interface design. Moreover, pain at the base of the thumb has been associated with prolonged smartphone use (Choi et al., 2025), highlighting the need to understand the loading response at the trapeziometacarpal joint. In biomechanical modelling, the proposed device can provide accurate force magnitude, direction, and location inputs that enable MSk and FE models of the hand to ascertain joint forces and moments and evaluate hand function during smartphone use and potential susceptibility to joint degeneration or injury. For example, realistic smartphone interaction scenarios using the force plate can explore how variations in device characteristics, such as screen size and device weight, influence fingertip forces and user biomechanics.

To enable investigation of the effect of smartphone size on thumb kinematics and kinetics, two additional force plates were manufactured based on the same structural and electrical design described in this chapter but scaled to the 50th and 90th percentiles of the dimensions of the 109 smartphones described in Section 3.2.1. These additional force plates were calibrated using the same procedure, and their force and positional errors were within 0.15 N and 3 mm, respectively. Together with the force plate presented in this chapter, these three devices therefore represent small, medium, and large smartphone sizes.

3.5. Practical technical considerations

This project involved extensive technical manufacturing processes, and several practical considerations were critical for successful replication of the force plate. Surface preparation prior to strain gauge bonding was particularly important, as

inadequate roughening or contamination could reduce adhesion and compromise measurement accuracy. At the same time, an appropriate level of surface roughness was required to ensure effective bonding.

The wiring of the strain gauges also required careful handling. The connection points were fragile and not protected by an insulating sheath; therefore, the wires were secured to the load cell to prevent mechanical strain and potential damage to the soldered joints.

During the fabrication of the load cell, the polycarbonate plate needed to be firmly fixed to ensure machining accuracy. A layer of double-sided tape was applied to stabilise the plate, and a thin film (approximately 0.2 mm) was intentionally retained at the base during cutting to avoid uneven machining of the spring beam. This remaining layer was removed later.

All fabrication and assembly processes were performed by the author, ensuring consistency across devices. These considerations highlight key practical aspects that should be carefully controlled when replicating the construction of this load cell and developing similar custom sensors.

3.6. Conclusion

With the force plate made and validated, subsequent work in this thesis focuses on extending its application by employing three plate sizes in combination with a motion capture system. In the next Chapter, this integrated setup is utilised for the simultaneous collection of kinetic and kinematic data during smartphone use and examines how smartphone size, hand dimensions, and interaction activity influence thumb kinematics and kinetics.

Chapter 4

Kinetics and kinematics of the thumb during smartphone activities

Chapter 4 investigates the kinematics and kinetics of the thumb during common smartphone activities, including typing and swiping. The custom force plates presented in the preceding chapter are used along with a motion-capture system for the simultaneous collection of kinematic and kinetic data of the thumb of volunteers during smartphone use. Twenty right-handed participants were recruited to perform touchscreen tasks on three different-sized force plates representing small, medium, and large smartphones. The chapter examines the effects of smartphone size, key location, swipe direction, and individual hand dimensions on thumb joint kinematics and kinetics. The chapter concludes by interpreting these findings in the context of thumb biomechanics and ergonomics, and by identifying their implications for computational modelling and smartphone interface design.

4.1. Introduction

As outlined in Chapter 2, smartphone use places high mechanical demands on the thumb and the TMC joint due to the holding posture employed during smartphone use. When the first iPhone was introduced in 2007, its capacitive multi-touch screen replaced physical buttons with thumb-driven gestures, establishing the interaction paradigm used by modern smartphones. Since then, the standard iPhone screen size has increased by 50%, and even larger smartphones, such as Samsung Galaxy S25 Ultra ($162.8 \times 77.6 \times 8.2\,mm$), are now common. Smartphone size, dimensions and weight have been shown to influence grip comfort (Lee et al., 2019). Another study demonstrated that larger keypad phone sizes also lead to greater thumb abduction and higher movement velocities, suggesting that device dimensions directly affect thumb range of motion and may contribute to MSk strain during smartphone use (Jonsson et al., 2007).

Previous research investigating smartphone biomechanics has focused on either kinematics or kinetics in isolation. For example, thumb motion has been captured using electrogoniometers or optical motion capture, while touchscreen forces have been measured using commercial load cells. However, the size and mass of these sensors often alter natural device interaction, either by increasing phone thickness or restricting hand support, limiting the ecological validity of these measurements.

Chapter 3 addressed these limitations by developing and validating a smartphone-sized force plate capable of measuring thumb–screen interaction forces without altering typical handling behaviour. When synchronised with motion capture, this platform enables simultaneous measurement of thumb kinematics and kinetics during realistic touchscreen use.

The present study applies this integrated system to examine how smartphone size influences thumb kinematics and kinetics, and whether these biomechanical variables are correlated with individual hand dimensions. It was hypothesised that larger

smartphones would increase thumb joint range of motion and applied force, whereas greater hand dimensions would be associated with reduced joint range of motion due to enhanced reachability, but increased applied force. By combining motion capture with a custom-designed force plate, the study sought to provide insight into how variations in smartphone design interact with anatomical factors, which may inform future ergonomic guidelines and smartphone design.

4.2. Materials and method

4.2.1. Study participant

Twenty healthy participants (10 male and 10 female), all right-handed and aged between 19 and 31 years, were recruited for the study. The study was approved by the local ethics committee (reference number: 7411234). Prior to participation, informed consent was obtained from all participants. None of the participants reported a history of pain in the hands, wrists, arms, or shoulders. All individuals had more than five years of smartphone experience and reported using their devices daily. Each participant's hand span (measured from the tip of the outstretched thumb to the tip of the outstretched fifth digit), thumb–index span (measured from the tip of the outstretched thumb to the tip of the outstretched second digit), and the lengths of each thumb segment (distal phalanx (TDP), proximal phalanx (TPP), and first metacarpal (MC1)) were measured to analyse individual anatomical characteristics in relation to thumb kinematics and applied forces.

4.2.2. Marker placement and digitisation

The primary degrees of freedom (DoFs) of the thumb include flexion-extension (F-E) at the interphalangeal (IP), metacarpophalangeal (MCP), and trapeziometacarpal (TMC) joints, as well as adduction-abduction (A-A) and internal-external rotation (I-E) at the

TMC joint. To quantify the angles corresponding to these five DoFs, clusters of three retroreflective markers were placed on: the TDP, TPP, MC1, third metacarpal (MC3), distal forearm, and proximal forearm (Figure 4.1). Since the trapezium is difficult to palpate and its position relative to MC3 remains fixed, the marker cluster placed on MC3 was used to reflect the position of the trapezium (Cooney et al., 1981; Kuo et al., 2003). The locations of the reflective markers were monitored using a ten-camera optical motion capture system (Qualisys AB, Gothenburg, Sweden), with kinematic data recorded at a frequency of 100 Hz.

The relative position of the trapezium with respect to the MC3 varies among individuals. To account for this variability, all participants were asked to reproduce a standardized neutral thumb posture, defined as the thumb positioned in the plane of the palm, with the TDP and TPP aligned in a straight line and the TPP resting lightly against the radial side of the palm. This neutral posture was used as the baseline posture of the TMC joint, defining 0° F-E, 0° A-A and 0° I-E.

To ensure data comparability across participants, 10 bony landmarks were digitised: the head of the phalanx, two lateral bony prominences of the IP joint, two lateral bony prominences of the MCP joint and the condyles of the TMC joint. Local coordinate systems of each segment were constructed based on the recommendations of International Society of Biomechanics (Wu et al., 2005).

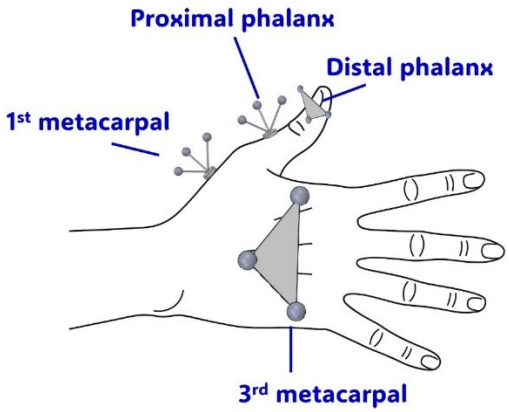


Figure 4.1 Placement of clusters of three retroreflective markers on the forearm and hand

4.2.3. Experimental protocols

To measure the forces exerted by the thumb during touchscreen interactions, custom-built force plates were used in place of smartphones (Chapter 3). Data were sampled from the force plates at a frequency of 100 Hz, consistent with the optical motion capture system. These force plates were designed to resemble closely the dimensions and weights of commercial devices to allow natural handling. To characterise device dimensions, the sizes of 109 smartphone models released by three major manufacturers, Samsung, Apple, and Xiaomi, between 2014 and 2025 were collected, and cumulative distribution functions of device height and width were generated. Representative values corresponding to the 10^{th} ($139.2 \times 68.5 \times 10\ mm$), 50^{th} ($153.2 \times 73.9 \times 10\ mm$), and 90^{th} ($163.3 \times 77.8 \times 10\ mm$) percentiles of height and width distributions were used to construct three force plate sizes for comparative analysis (Figure 4.2). The order in which participants used the three plates was randomized.

Participants were instructed to hold each force plate in a comfortable, self-selected posture, similar to how they would typically use their own smartphones. The force plate

was positioned according to each participant's comfort to ensure natural interaction. The cables were arranged to avoid tension and routed away from the contact area to prevent interference with force measurements (Figure 3.1b). They were asked to complete two types of touchscreen tasks: swiping and typing. The swiping task included four directions: up, down, left, and right, with each direction repeated ten times. The swipe-up and swipe-down gestures simulated scrolling through social media applications such as Instagram, while left and right swipes mimicked photo browsing or page turning. The typing task simulated dialling, requiring participants to press all keys on a full letter keyboard and dial pad. This task was repeated three times, and a mock screen (Figure 4.2) was attached to the top of each force plate to indicate the key positions to press.



(a) (b)

Figure 4.2 (a) Sizes of three force plates. Dimensions are in millimetres. (b) Experimental setup with a participant performing touchscreen interaction on the force plate.

Each of the three force plate sizes was used once to complete a full set of swiping and typing tasks. The experimental design enabled the examination of whether smartphone size affected thumb kinematics and the forces applied during touchscreen interaction.

4.2.4. Data processing

From each swipe, the peak force and peak joint angles were extracted; these values were averaged across the ten repetitions per direction. From the typing task, the peak force while pressing each key was extracted and it was identified as the maximum force applied at that position. The kinematic data were taken at the same time frame as that peak force (Figure 4.3). MATLAB (R2024b, The Mathworks, Inc., Natick, MA) was used for all calculations.

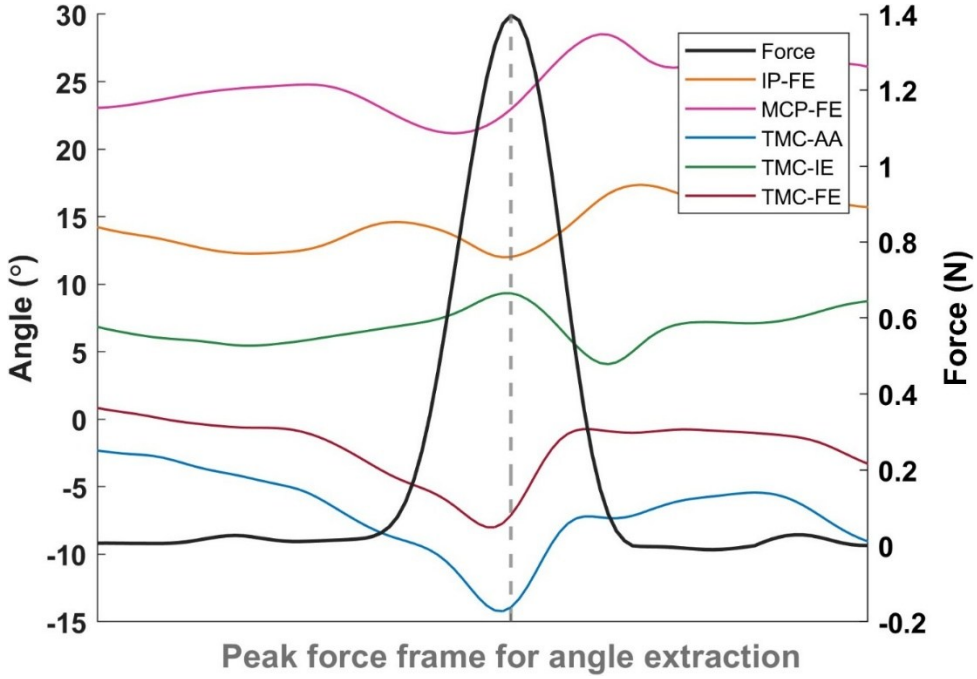


Figure 4.3 Representative synchronized force and joint angle profiles during a typing keypress. The peak (dashed line) was identified in the force curve (dashed line), and the joint angles for each joint degree of freedom were extracted for the same frame. Joint angles are plotted with an offset for visualization. IP: interphalangeal; MCP: metacarpophalangeal; TMC: trapeziometacarpal; F–E: flexion–extension; A–A: adduction–abduction; I–E: internal–external rotation.

The Shapiro–Wilk test indicated that the data could not be assumed to be normally distributed ($p < 0.05$). Therefore, non-parametric Friedman tests were used to determine whether there were differences in kinematic and kinetic measurements across smartphone sizes, key positions, and swiping directions with Bonferroni correction

applied to the post-hoc tests. Adjusted p-values (p_{adj}) were calculated based on Eq.4.1, where p_{raw} denoted the unadjusted p-value from an individual test, and m was the total number of hypotheses tested (i.e., the number of comparisons made). Statistical significance was defined as $p_{adj} \leq 0.05$.

$$p_{adj} = \min(1, m \cdot p_{raw}) \quad \text{Eq.4.1}$$

Post-hoc pairwise comparisons were defined separately for each analysis to reflect the structure of the experimental factors (Table 4.1). For example, in analysis B (key position effect), post-hoc tests compared all key positions using pairwise contrasts $\left(\binom{12}{2} = 66\right)$. These comparisons were conducted within each force plate size (3 sizes) and for each kinematic outcome (5 DoFs), yielding 990 post-hoc comparisons in total ($5 \times 66 \times 3$).

Since the hand dimensions were highly intercorrelated (Greiner, 1991), partial least squares (PLS) regression was employed to model the relationships between hand dimensions and the kinematic and kinetic variables. PLS regression reduces the original correlated hand-dimension variables into a smaller set of latent components, each representing a weighted combination of the original variables, while preserving their relationship with the kinematic and kinetic outcomes. Cross-validation was used to determine the best number of latent components. Coefficients of determination (R^2) greater than 0.50 were interpreted as indicating moderate or high correlations (Hair et al., 2011). All statistical analyses were performed using MATLAB.

Analysis	Dependent variables	Independent variable	Repeated factor	Number of post-hoc tests
A: Effect of force plate size on thumb kinematics during typing	Peak joint angles	Force plate size	Key position	180
B: Effect of key position on thumb kinematics during typing	Peak joint angles	Force plate size	Key position	990
C: Effect of force plate size on thumb kinetics during typing	Peak thumb force	Key position	Force plate size	36
D: Effect of key position on thumb kinetics during typing	Peak thumb force	Key position	Force plate size	198
E: Effect of force plate size on thumb kinematics during swiping	Peak joint angles	Force plate size	Swiping direction	60
F: Effect of force plate size on thumb kinetics during swiping	Peak joint angles	Force plate size	Swiping direction	90
G: Effect of swiping direction on thumb kinematics during swiping	Peak thumb force	Swiping direction	Smartphone size	12
H: Effect of swiping direction on thumb kinetics during swiping	Peak thumb force	Swiping direction	Smartphone size	18
I: Relationship between hand dimensions and kinetics/kinematics	Hand dimensions (predictors); peak joint angles and forces (responses)			

Table 4.1 Statistical tests conducted in this study.

4.3. Results

4.3.1. Typing

4.3.1.1. Kinematics

Differences between the force plate sizes were observed in 5.6% of the post-hoc tests within analysis A (Figure 4.4, Table 4.2). In contrast, differences across key positions were identified in 20.8% of the post-hoc tests within analysis B (Figure 4.4, Table A.1). Specifically, flexion at the IP and MCP joints showed an increasing trend between key locations on the right side of the keypad (keys 1, 4, 7, *) to those on the left (keys 3, 6, 9, #). For the TMC joint, adduction increased when pressing keys on the right side of the phone, while greater extension was observed for keys located at the bottom of the phone (e.g., 0 and *). Internal–external rotation of the TMC joint was similar across all positions. All statistical comparisons are provided in the Appendix (Table A.1).

Joint	Degree of Freedom	Position on the keypad	Phone sizes compared	Significance level
IP	F-E	1	Small-Large	**
IP	F-E	1	Medium-Large	*
IP	F-E	3	Small-Large	**
IP	F-E	6	Medium-Large	*
IP	F-E	8	Small-Large	*
IP	F-E	#	Medium-Large	*
MCP	F-E	*	Small-Large	*
MCP	F-E	0	Small-Large	*
TMC	A-A	7	Medium-Large	***
TMC	I-E	1	Small-Large	**

Table 4.2 Post-hoc results of the size effect on primary degrees of freedom. IP: interphalangeal joint; MCP: metacarpophalangeal joint; TMC: trapeziometacarpal joint; F–E: flexion–extension; A–A: adduction–abduction; I–E: internal–external rotation. Statistically different results are only shown (* p_{adj}<0.05, ** p_{adj}<0.01, * p_{adj}<0.001)**

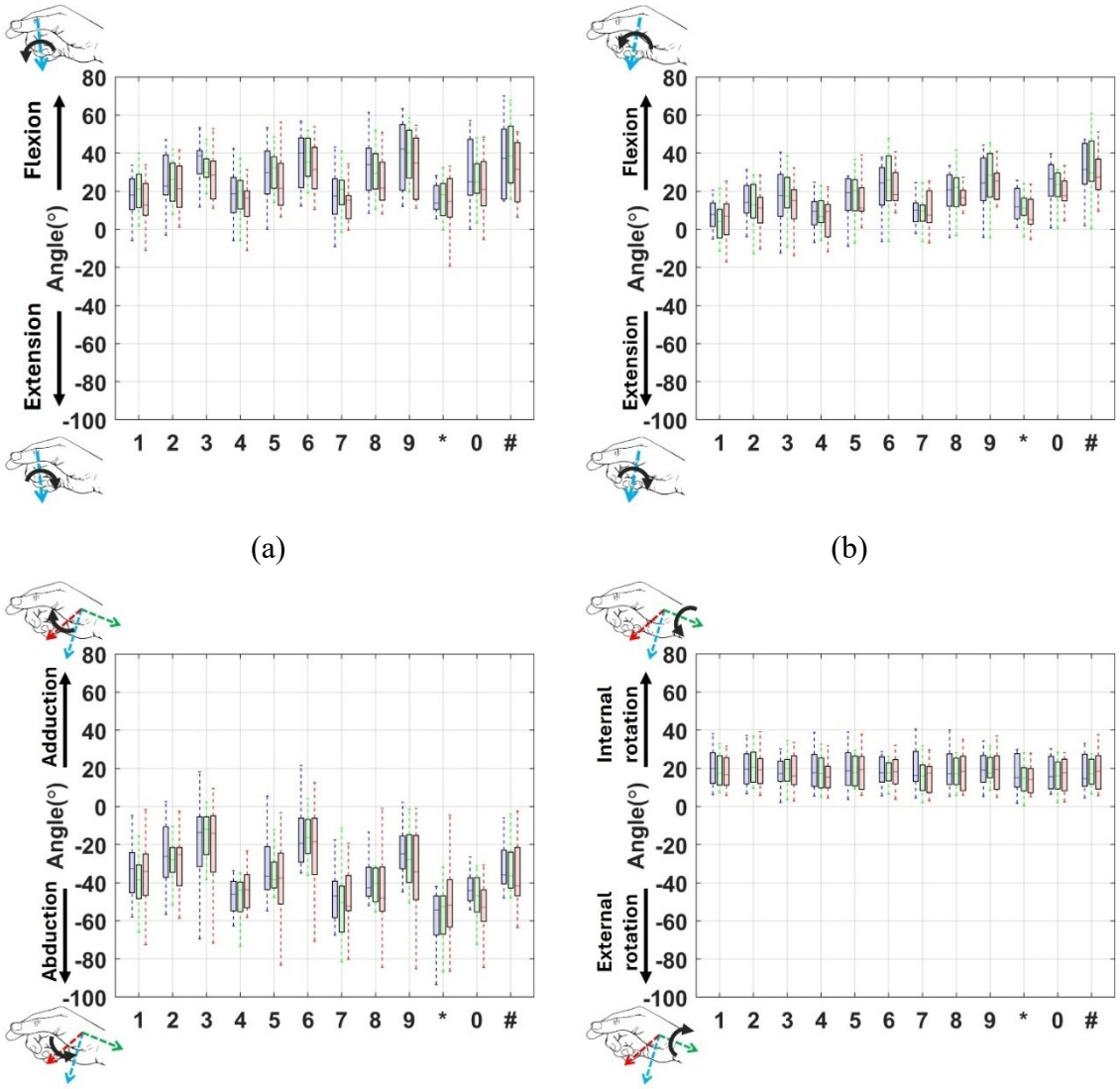


Figure 4.4

Joint angles of (a) interphalangeal: flexion–extension, (b) metacarpophalangeal: flexion–extension, (c) trapeziometacarpal: adduction–abduction, (d) trapeziometacarpal: internal–external rotation, and (e) trapeziometacarpal: flexion–extension, when using force plates of small, medium, and large sizes during typing. Positive values represent flexion, adduction, and internal rotation.

4.3.1.2. Kinetics

Overall, 16.7% (6 of 36) of the post-hoc tests within analysis C showed differences in the resultant applied force across sizes (Figure 4.5). The force was similar between medium and large sizes; however, six tests comparing the small with medium and large phone sizes revealed significant differences (Table 4.3). Only 5.6% (11 of 198) of the post-hoc test within analysis D presented differences in key positions. Nevertheless, key position had a notable effect on force in the small-sized phone, with 11 pairwise differences identified (Table 4.4).

Position	Phone sizes compared	Significance level
1	Small-Medium	**
4	Small-Medium	*
4	Small-Large	*
7	Small-Large	**
10	Small-Medium	**
10	Small-Large	***

Table 4.3 Post-hoc results of size effect on force applied by the thumb during typing. Only statistically different results are shown (* p_{adj}<0.05, ** p_{adj}<0.01, * p_{adj}<0.001).**

Size	Keypad positions compared	Significance level
Small	2-7	*
Small	2-*	*
Small	2-#	*
Small	5-7	*
Small	5-10	*
Small	7-9	*
Small	7-#	*
Small	8-9	*
Small	8-#	*
Small	9-*	*
Small	*-#	*

Table 4.4 Post-hoc results of button effect on force. Only statistically different results are shown (* p_{adj}<0.05, ** p_{adj}<0.01, * p_{adj}<0.001).**

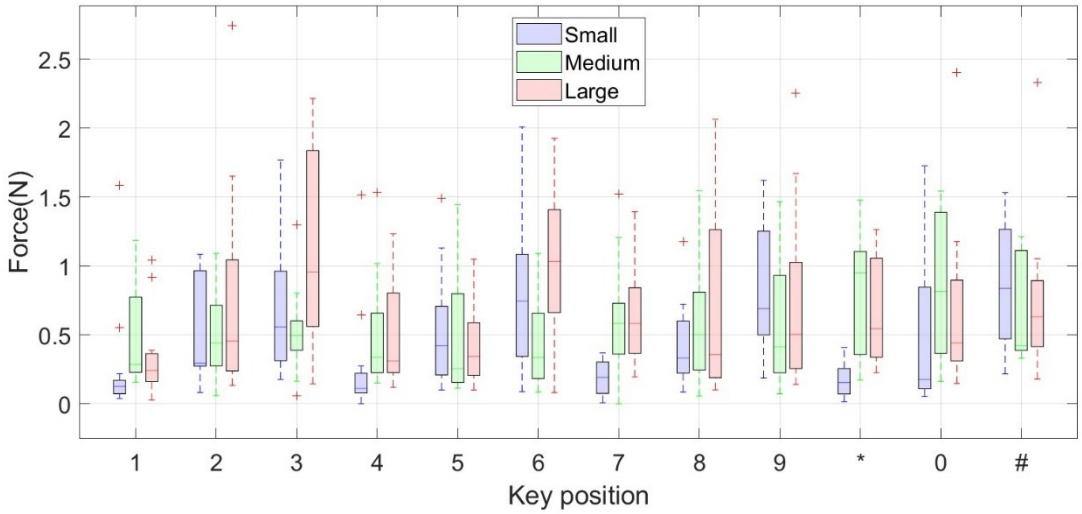


Figure 4.5 Applied force of the thumb during typing when using force plates representing small, medium, and large size smartphones.

4.3.2. Swiping task

4.3.2.1. Kinematics

No differences were found among force plate sizes for any joint DoFs (Figure 4.6). Swipe direction (up, down, left, right) showed an effect on thumb kinematics, with 10% (9 of 90) of post-hoc tests within analysis F indicating statistical differences (Table 4.5).

Joint	Degree of Freedom	Phone size	Swiping directions compared	Significance level
MCP	F-E	Small	Down-Left	*
MCP	F-E	Medium	Up-Left	**
TMC	A-A	Small	Up-Left	*
TMC	A-A	Medium	Up-Left	**
TMC	A-A	Large	Down-Left	*
TMC	F-E	Small	Up-Left	**
TMC	F-E	Small	Down-Left	*
TMC	F-E	Large	Up-Left	**
TMC	F-E	Large	Down-Left	*

Table 4.5 Post-hoc results of direction effect on primary degrees of freedom (DoF) IP: interphalangeal; MCP: metacarpophalangeal; TMC: trapeziometacarpal; F–E: flexion–extension; A–A: adduction–abduction; I–E: internal–external rotation. Only statistically different results are shown (* p_{adj}<0.05, ** p_{adj}<0.01, * p_{adj}<0.001)**

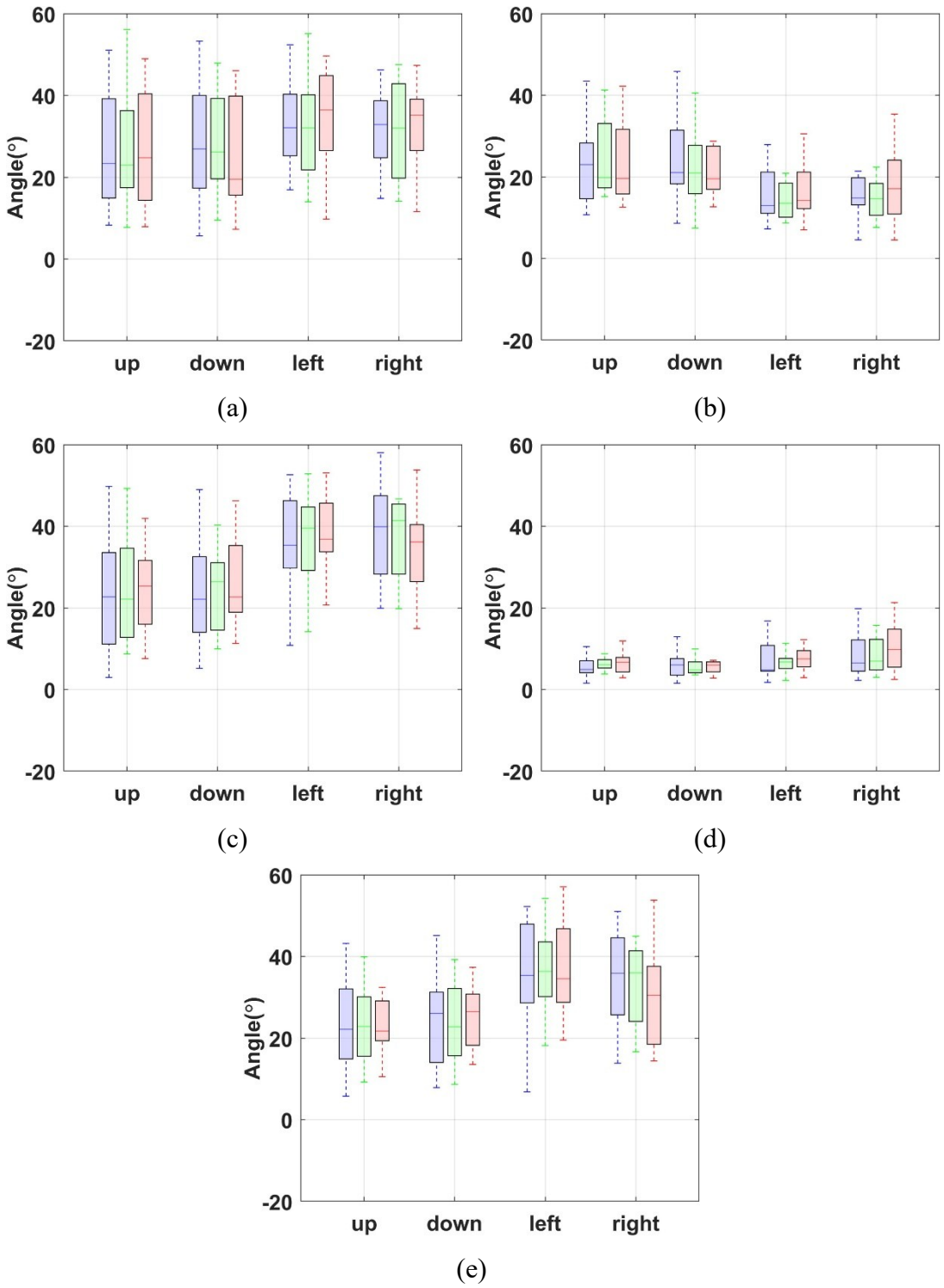


Figure 4.6 Range of motion of (a) interphalangeal: flexion–extension, (b) metacarpophalangeal: flexion–extension, (c) trapeziometacarpal: adduction–abduction, (d) trapeziometacarpal: internal–external rotation, and (e) trapeziometacarpal: flexion–extension, when using force plates of small, medium, and large sizes during swiping.

4.3.2.2. kinetics

For analysis G, 5 out of 12 (41.7%) post-hoc tests comparing the applied force of the thumb between force plate sizes during swiping demonstrated statistical differences (Figure 4.7). Forces in the large force plate condition were consistently greater than those in the small force plate across all directions. Post-hoc comparisons confirmed differences between small and large force plates for all swipe directions, as well as between small and medium force plates in the left-swipe condition (Table 4.6). No differences were observed between medium and large force plates. In contrast, the swiping direction had minimal influence on thumb kinetics, with no differences observed.

Swiping direction	Smartphone sizes compared	Significance level
Up	Small-Large	***
Down	Small-Large	***
Left	Small-Large	**
Left	Small- Medium	*
Right	Small-Large	*

Table 4.6 Post-hoc results of size effect on force during swiping. Only statistically different results are only shown (* p_{adj}<0.05, ** p_{adj}<0.01, * p_{adj}<0.001).**

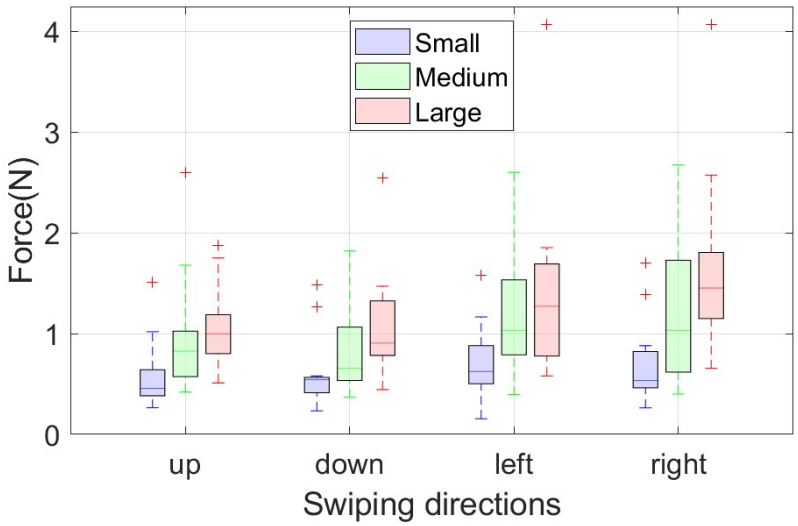


Figure 4.7 Applied force by the thumb during swiping when using force plates of small, medium, and large sizes

4.3.2.3. correlation between hand dimensions and corresponding kinematic and kinetic measurements

Prior to performing the PLS analysis, cross-validation was conducted to determine the optimal number of components to retain in the regression model. The cross-validation results indicated that a single component provided the best predictive performance. Accordingly, the variation in hand dimensions was represented by one latent component, comprised of weighted hand dimensions (Table 4.7). A higher weight meant that the corresponding hand dimension had a greater influence on the latent component and therefore explained a larger extent of the variability in hand morphology that was most relevant to the kinematic and kinetic outcomes. Thumb-index span and hand span contributed the highest weights (over 80%).

Condition (force plate size-key or swipe direction)	Distal Phalanx	Proximal Phalanx	Metacarpal	Thumb-Index Span	Hand Span
Small-1	1.1	0.6	0.4	40.5	57.4
Small-2	1.8	1.4	0.6	49.2	47.0
Small-3	2.3	1.5	0.0	45.6	50.6
Small-4	1.2	0.6	0.3	46.5	51.3
Small-5	1.5	1.4	0.1	65.0	31.9
Small-6	1.8	1.2	0.3	59.7	37.0
Small-7	1.3	0.1	0.0	40.4	58.2
Small-8	1.3	0.6	0.1	70.1	27.9
Small-9	1.9	1.2	0.1	56.4	40.5
Small-*	1.1	0.2	0.2	38.1	60.4
Small-0	0.8	0.1	0.4	80.6	18.1
Small-#	1.9	0.5	0.2	57.8	39.6
Medium-1	1.3	0.3	1.6	26.0	70.8
Medium-2	1.9	1.3	2.2	32.2	62.4
Medium-3	2.2	1.5	1.0	37.8	57.5
Medium-4	0.8	0.6	1.3	26.2	71.0
Medium-5	2.1	1.2	1.0	40.4	55.3
Medium-6	2.3	1.3	0.2	40.2	56.0
Medium-7	1.0	0.8	1.2	28.1	68.9

Medium-8	1.5	0.9	0.9	42.8	53.9
Medium-9	1.8	1.1	0.5	41.3	55.3
Medium-*	0.6	0.4	0.5	33.4	65.1
Medium-0	0.6	0.2	0.1	51.4	47.7
Medium-#	1.4	0.5	0.0	49.2	48.9
Large-1	0.5	0.7	1.8	39.0	58.0
Large-2	0.5	1.0	0.2	59.4	38.9
Large-3	0.6	1.0	0.0	65.6	32.8
Large-4	1.0	0.5	1.7	35.4	61.4
Large-5	0.6	0.5	0.6	68.7	29.6
Large-6	1.9	1.5	0.7	50.5	45.5
Large-7	0.9	0.2	1.8	34.1	63.0
Large-8	0.6	0.5	0.3	69.9	28.7
Large-9	0.8	0.5	0.0	62.9	35.6
Large-*	1.0	0.1	1.8	34.8	62.3
Large-0	0.9	0.3	0.8	49.6	48.5
Large-#	0.9	0.3	0.2	62.8	35.8
Small-up	4.8	0.4	6.9	15.3	72.5
Small-down	2.6	0.1	0.8	59.4	37.1
Small-left	3.8	0.6	0.1	50.9	44.7
Small-right	2.2	0.1	0.4	57.8	39.6
Medium-up	4.1	0.5	10.5	19.0	66.0
Medium-down	2.2	0.2	1.9	54.1	41.6
Medium-left	3.0	0.7	0.5	51.4	44.3
Medium-right	1.7	0.1	0.1	49.2	48.9
Large-up	1.9	0.6	0.3	60.3	36.9
Large-down	2.5	0.1	0.2	47.2	49.9
Large-left	1.6	0.1	0.3	77.8	20.2
Large-right	0.9	0.0	2.7	69.1	27.2

Table 4.7 Weight (in %) of each hand dimension contributing to the first latent component derived from partial least squares (PLS) regression for each combination of force plate size and key position or swipe direction.

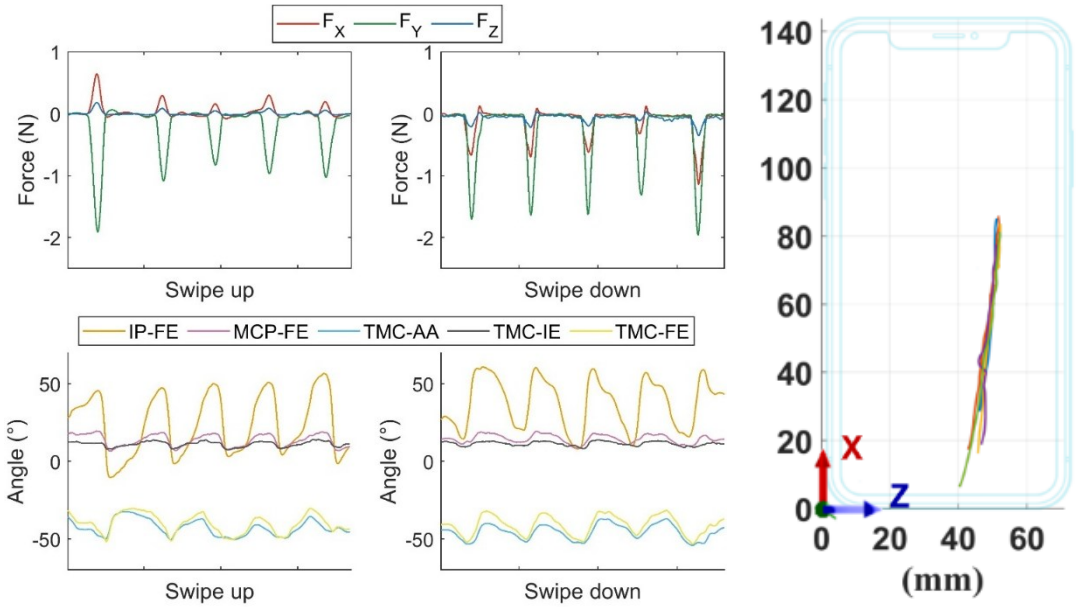
The coefficients of determination (R^2) were obtained from the PLS regression between the latent hand dimension component and the kinematics and kinetics of the thumb. Only 30 out of 240 (12.5%) kinematic R^2 values and 3 out of 48 (6.3%) kinetic R^2 values exhibited strong correlations ($R^2 > 0.70$), which occurred sporadically. The complete results are provided in Appendix Table A.2.

4.3.2.4. Difference between directions

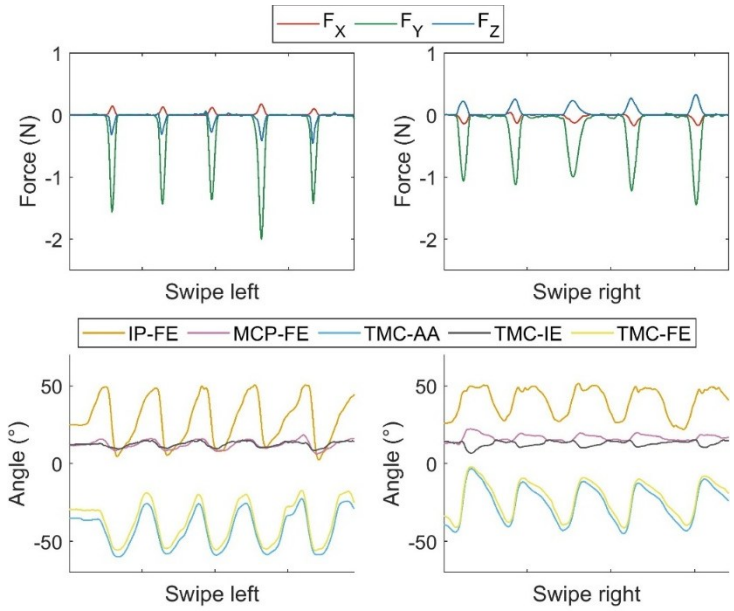
Differences between swiping directions were observed in both force and kinematic profiles (Figure 4.8). For vertical swiping, swipe-up and swipe-down tasks exhibited similar magnitudes of force and joint range of motion (Figure 4.8a); however, the direction of movement was opposite. The timing of peak forces also differed between the two conditions, occurring at distinct phases of the motion cycle. Specifically, peak forces occurred during joint extension in swipe-up and during flexion in swipe-down, however, the absolute joint angles at these peak force instances were comparable.

The force traces for 5 swipe-up cycles are shown in Figure 4.8b as an example. They were consistent with the force data, with positive X and Z components and a negative Y component. The presence of a small Z-direction force indicated that the movement trajectory was not strictly vertical.

A similar pattern was observed for horizontal swiping (Figure 4.8c), where swipe-left and swipe-right showed comparable force magnitudes and joint kinematics, but with reversed movement patterns and corresponding shifts in force timing.



(a) (b)



(c)

Figure 4.8 (a) Representative force and kinematic profiles over five swipe-up and swipe-down cycles. (b) Representative force traces over five swipe-up cycles. (c) Representative force and kinematic profiles over five swipe-left and swipe-right cycles. IP: interphalangeal; MCP: metacarpophalangeal; TMC: trapeziometacarpal; F–E: flexion–extension; A–A: adduction–abduction; I–E: internal–external rotation.

4.4. Discussion

This study investigated thumb kinematics and kinetics during common smartphone

activities, using a handheld, phone size-matched force plate synchronised with a motion capture system. The effects of device size, keypad position, swipe direction, and individual hand dimensions on the kinematics and kinetics of the thumb were examined. It was found that device size affected the forces exerted by the thumb during swiping tasks and to a lesser extent during typing. Kinematic differences were associated with keypad position but were largely not related to the size of the device, suggesting that specific touchscreen locations place greater biomechanical demands on the thumb than other locations. The hand dimensions of the participants were found to have limited correlation with both kinematics and kinetics.

4.4.1.1. Kinematics

In the typing task, device size had a limited effect on thumb kinematics during typing, with differences observed in a small proportion of comparisons. This was likely because participants were instructed to use their right thumb to perform all tasks but were permitted to stabilise the device with their left hand. In practice, this allowed them to adjust their grip or to reposition the device, as would occur during regular device use, thereby avoiding extreme joint angles and reducing the influence of device size on thumb motion.

In contrast, the key position appeared to influence thumb posture; in particular, flexion at the IP and MCP joints and both flexion and abduction at the TMC joint increased progressively from the leftmost to the rightmost of the phone. This overall directional pattern across the keypad was consistent, albeit certain pairwise comparisons between key positions did not yield statistical differences in kinematics, for example, key 1 versus key 4 and key 5 versus key 8. The lack of significance in specific comparisons may not imply the absence of positional influence but may reflect the limited statistical power of individual comparisons to capture systematic patterns across the keyboard layout.

For the swiping tasks, device size did not affect thumb kinematics. Across the small,

medium, and large devices, joint-angle patterns remained consistent, suggesting that individuals adjust the way they hold the device to perform the task; as swiping gestures are not constrained to a specific target area on the screen, users are able to perform the action wherever it feels most comfortable, thereby minimising the influence of device size on thumb kinematics.

4.4.1.2. Kinetics

Analysis of the reaction forces during typing revealed that the small device generally was associated with lower forces compared with the medium and large devices, while forces between medium and large sizes were similar (Figure 4.5). This outcome may be explained by the way participants held the devices: 18 out of 20 participants used a one-handed grip for the small device. In this configuration, it was more difficult to control and stabilise the phone while performing precise tapping tasks, as tapping requires the thumb to press on a specific target area. It is plausible that participants tended to apply less force to the keys on the small device to avoid destabilising it, whereas the medium and large devices, which were stabilised with both hands by 18 out 20 participants, allowed for firmer and more consistent force application.

Although only a small proportion of key position comparisons reached statistical significance, using the small device showed more positional variability than using the medium and large devices. This suggests that reduced stabilisation in one-handed use not only limited the absolute magnitude of applied forces but also introduced variability across different key positions. These findings highlight that ergonomic differences in smartphone use were not solely determined by screen size, but also by the strategies users adopt to stabilise the device during fine motor tasks.

4.4.1.3. Hand dimensions

The hand dimensions included were known to exhibit substantial interdependence,

meaning they could not be treated as statistically independent predictors. PLS regression was therefore used rather than traditional regression, because it accounted for multicollinearity while also maximised covariance with the kinematic and kinetic outcomes. This method has been established as an appropriate analytical approach for assessing relationships between hand dimensions and its biomechanical performance (Rostamzadeh et al., 2021).

Although thumb–index span and hand span were the dominant contributors to the latent morphology component, the correlations between the latent component and the kinematic and kinetic outcomes were weak. Therefore, individual hand dimensions had limited effect on thumb kinematics or kinetics during smartphone use, which is consistent with prior research (Gustafsson et al., 2018).

4.4.1.4. Implications

The results of this study suggest that ergonomic risk of smartphone use is affected more by an individual's interaction strategy with the touchscreen as they engage with information at specific locations on the screen than by device size. For typing, the progressive increase in thumb flexion and adduction when reaching toward lateral and lower key positions indicated that interface regions located further from the neutral thumb posture may impose greater cumulative strain during prolonged use. For swiping, the distinction between vertical and horizontal gestures demonstrated that movement direction, rather than device dimensions, drove postural change. These findings suggest that the design of phone interfaces, such as the placement of frequently used functions, and user instruction on grip strategies might be more effective for ergonomic intervention than prescribing device size. Moreover, the weak associations between hand dimensions and biomechanical outcomes reinforce that ergonomic solutions should prioritise universal design principles, rather than tailoring devices to specific hand sizes.

The dataset generated in this study can also support further research into potential

pathology of the thumb joints from smartphone use. MSk and FE simulations are used commonly for the study of joint mechanics and joint pathology; they require experimentally derived boundary conditions, including joint kinematics and kinetics. The synchronised motion and force data collected here offer a reproducible set of inputs that can be incorporated into such models to explore internal joint loading during smartphone use.

4.4.1.5. Limitations

Several limitations should be acknowledged. Participants were instructed to perform all tasks with their right thumb; for all participants the right hand was their dominant hand. While this ensured consistency across conditions, it did not fully reflect natural smartphone use, in which individuals often switch hands or use both thumbs to perform tasks. Participants were also instructed to ensure the stability of the force plate during task performance. When one-handed operation was insufficient, the non-dominant hand was used to support the base of the device. While this approach improved measurement reliability, it might have reduced ecological validity, as real-world smartphone interactions are not always performed under stable holding conditions. In addition, the extent of stabilisation varied, which may have influenced the forces measured, particularly in the small device condition.

The exclusive inclusion of right-handed participants was also influenced by practical constraints. Incorporating both left- and right-handed conditions would have required repeated mirroring and recalibration of the motion capture system, increasing experimental complexity and potential sources of error.

Furthermore, the results showed that interactions with keys located further from the task-performing thumb were associated with more extreme joint kinematics and increased biomechanical demand. It is therefore reasonable to expect that a similar pattern would be observed for left-handed users, with higher demands occurring at positions further from the thumb in their respective usage configuration. However, this

was not directly investigated in the present study. Future work should include left-handed and bimanual interactions to provide a more comprehensive understanding of smartphone use behaviours.

As reviewed in Chapter 2, soft tissue artefact (STA) is known to depend on marker location and is primarily caused by skin movement and deformation of the underlying soft tissues relative to the bone (Camomilla et al., 2015). STA has been reported to be more pronounced in regions closer to joints, where greater skin motion and deformation occur (Cappozzo et al., 1996). This influence could be reduced through the use of rigid supports (Leardini et al., 2005). Accordingly, in the present study, markers were arranged as rigid clusters and positioned over the shafts of the bones, along the longitudinal axis of each segment, where soft tissue motion is relatively limited compared to joint regions.

The use of custom-built force plates also introduces limitations. Although the size and weight closely replicated commercial smartphones, and a screen protector was attached to simulate the feel of a smartphone screen, these features could not reproduce perfectly the tactile and haptic feedback of real devices, which might have altered how participants interacted with the surface. These factors should be considered when interpreting the results, and future studies incorporating realistic touchscreen feedback would provide further physiological validity.

The difference between the ideal and experimental boundary conditions of the force plate should also be acknowledged. During the calibration of the force plate, loads were applied using an indenter onto the force plate, which was fixed on a rigid base. In contrast, during experimental use, the device was supported by the hand, introducing a more compliant and less controlled boundary condition. Despite this difference, the force measurement was fundamentally governed by the deformation of the load-cell structure. Provided that the applied thumb force is fully transmitted to the force plate without significant loss, as per the intended design of the load cell, the measured

response is primarily determined by the structural deformation of the load cell. As such, the influence of the supporting condition (rigid base versus hand-held) on the force measured is expected to be limited.

The demographic characteristics of the participants limits generalisability. The sample consisted solely of young adults, who typically exhibit high thumb mobility and frequent smartphone use. However, it is unclear whether their hand spans and thumb-reach characteristics reflect those of the wider population. Older adults, whose hand mobility, muscle strength, and motor strategies can differ substantially from those of young, healthy adults, may exhibit distinct thumb kinematics or loading patterns. As smartphone use becomes increasingly widespread in older populations (Pew Research Center, 2024, 2014), future studies should include a wider age range.

Another consideration is the short duration of the experimental tasks. Participants completed the requested tasks in approximately 30 minutes, which limits the ability to observe fatigue-related adjustments in thumb motion. Extended smartphone use, over hours or days, may alter kinematics or muscle loading and could contribute to the development of MSk symptoms. Future investigations should consider examining thumb biomechanics after prolonged, real-world device use.

4.5. Conclusion

This study examined thumb kinematics and kinetics during typing and swiping on three smartphone sizes in 20 healthy participants. By synchronising custom-designed, phone-like force plates with an optical motion capture system, the experimental setup preserved natural grip strategies while simultaneously recording joint motion and applied forces across common tasks. It was found that device size had a limited effect on thumb-joint angles but influenced the forces applied to the screen, particularly during swiping. In typing, the location at which the participants tapped in order to press

specific keys had a stronger influence on thumb posture than device size, with increased flexion of the IP, MCP, and TMC joints, and increased TMC adduction, observed when reaching towards keys positioned in the direction of the gripping hand. There was no discernible correlation between hand dimensions and biomechanical outcomes, indicating that reachable workspace and applied forces during smartphone interactions are not strongly determined by individual morphology.

The findings from this work suggest that ergonomic risk during smartphone use is determined primarily by the participant's interaction strategy with the smartphone and the interface layout rather than device dimensions, irrespective of hand size. Furthermore, the resulting data provide boundary conditions for MSk and FE simulations, which can be used to estimate internal joint stresses, evaluate long-term risks of overuse injury, and support the development of evidence-based ergonomic guidelines for smartphone design and use.

4.6. Chapter conclusion

The synchronised kinetic and kinematic dataset generated in this chapter provides a robust foundation for further biomechanical analysis. In the subsequent chapters, these data will be implemented as boundary conditions within a FE model of the TMC joint. Key loading scenarios identified in this study, including extreme joint postures and high applied forces, will be examined to quantify the resulting stress distribution across the joint. This approach will provide direct insight into the mechanical factors contributing to joint degeneration and overuse-related injury during smartphone use.

Chapter 5

Sensitivity analysis of finite element modelling of the trapeziometacarpal joint

In Chapter 4 kinetic and kinematic data during smartphone use were collected, providing physiologically realistic boundary conditions for computational modelling. Before applying these data to the finite element (FE) model of the trapeziometacarpal (TMC) joint in Chapter 6, Chapter 5 presents the development of FE models of the TMC joint and evaluates the robustness of the models through comprehensive sensitivity analyses. These analyses investigate the influence of CT-based bone geometry selection, ligament delineation methods, inter-digitisation operator variability in ligament attachment selection, and mesh density on model predictions. Collectively, the results establish the reliability of the FE modelling framework for subsequent application in Chapter 6 to smartphone-specific loading conditions obtained in Chapter 4.

5.1. Introduction

Understanding how smartphone activities influence joint stresses requires a computational approach capable of estimating internal joint mechanics that cannot be measured directly *in vivo*. FE modelling provides a suitable framework for evaluating the biomechanical behaviour of the TMC joint.

In the TMC joint, stability is primarily provided by the surrounding ligaments due to the limited bony constraint; therefore, the accurate representation of ligament mechanics is essential when simulating joint behaviour. However, modelling the TMC joint presents challenges that are not typically encountered in larger joints, such as the hip and knee. Unlike these joints, the TMC ligaments are small, overlapping structures that are not clearly visualised using computed tomography (CT) and magnetic resonance imaging (MRI), requiring their attachment sites to be inferred from anatomical literature and operator interpretation (Bajuri et al., 2012; Synek et al., 2012).

As reviewed in Chapter 2, section 2.7.5.1, one-dimensional (1D) spring elements are suitable when the primary aim is to examine the joint cartilage stress rather than ligament-specific stress (Gislason et al., 2009; Synek et al., 2012). However, the accuracy of predicted joint loading may depend on how the ligament attachment sites are selected. Anatomical studies differ in the number of TMC ligaments described and in the reported insertion positions, leading to inconsistencies in ligament representation within computational models (Bettinger et al., 1999; Ladd et al., 2012; Nanno et al., 2006).

In particular, while Bettinger et al. (1999) and Nanno et al. (2006) distinguished between superficial and deep components of the anterior oblique ligament (AOL), as well as between the intermetacarpal ligament (IML) and dorsal intermetacarpal ligament (dIML). Ladd et al. (2012) modelled the AOL and IML as a single structure and additionally included the dorsocentral ligament (DCL), which was absent in the other two anatomical studies. Moreover, substantial differences were observed in the

reported ligament dimensions across all studies, particularly for the dorsoradial ligament (DRL) and ulnar collateral ligament (UCL). These differences reflect distinct ligament delineation methods, referring to how individual ligaments are identified, subdivided, and assigned anatomical insertion regions based on cadaveric descriptions. Detailed comparisons of ligament dimensions reported in these three studies are provided in Appendix Tables A.3-A.5.

Additionally, ligament digitisation inherently depends on the digitisation operator's knowledge and interpretation of anatomical studies, introducing further variability in model creation and predicted outcomes.

Furthermore, considerable geometric variability has been reported in both the trapezium and the first metacarpal across specimens (Flanagan et al., 2022; Rusli and Kedgley, 2020); however, previous FE studies either relied on a single CT scan (Dong et al., 2023; Kurosawa et al., 2024; Synek et al., 2012) or averaged statistical geometry (Schneider et al., 2017), making it difficult to determine whether observed responses are robust or dependent on subject-specific morphology.

Accordingly, this study aims to evaluate how variability in ligament delineation methods, digitiser interpretation, and bone geometry influences TMC joint mechanics, as predicted in FEA. This sensitivity analysis provides important reference to improve the reliability and generalisability of FE modelling approaches.

5.2. Method

Three digitisation operators, three ligament delineation methods (Bettinger et al., 1999; Nanno et al., 2006; and Ladd et al., 2012), hereafter referred to as method B, N, and L, respectively, and three CT-based bone geometries were evaluated using a full factorial design. For each combination of ligament delineation method and bone geometry, ligament attachment sites were digitised independently by all three operators, resulting

in a total of 3×3×3=27 FE models.

Translation of the first metacarpal is an indication of TMC joint stability (Halilaj et al., 2015; Rusli et al., 2021; Ward et al., 2000). In vivo kinematic studies have shown that during daily functional activities, such as key pinch and jar grasp, the first metacarpal commonly undergoes volar translation relative to the trapezium (Halilaj et al., 2015; Ladd et al., 2013). Anatomically, the AOL and DRL have been identified as the primary stabilisers of the TMC joint, acting predominantly to resist dorsal-volar translation of the metacarpal (Bettinger et al., 1999; Esplugas et al., 2016; Ladd et al., 2012). Laxity of these two ligaments can lead to dorsal subluxation of the first metacarpal, which has been associated with altered joint mechanics and the development of TMC osteoarthritis (McCann et al., 2018; Pellegrini, 1991).

Since the sensitivity analyses in this study focus on modelling factors related to ligament delineation and representation, this study conducted translation simulations to examine how these factors affect the stress distribution over the articular cartilage. The first metacarpal was translated by 2 mm in volar and dorsal directions, corresponding approximately to the range of translation observed during daily activities (Halilaj et al., 2014). A consistent modelling workflow was applied to all models, and the procedures are described in the following sections (Figure 5.1).

Von Mises stress distribution over the trapezial cartilage was evaluated. As a widely adopted criterion for assessing yielding in ductile materials, Von Mises stress is based on the distortion energy theory and provides a scalar measure that enabled direct comparison across different loading conditions.

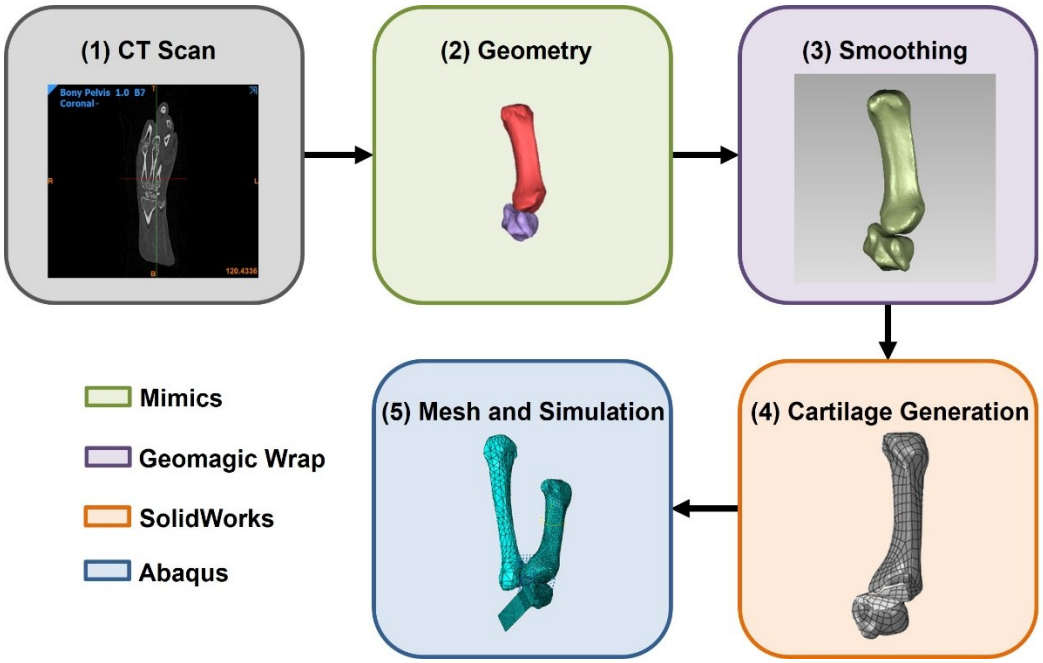


Figure 5.1 Workflow for developing finite element models of the trapeziometacarpal joint and the associated software used at each step

5.2.1. Geometry creation

FE models were created in Abaqus 2023 (SIMULIA, Dassault Systèmes, France) using CT scans of TMC joints from cadaveric specimens from anonymous donors held within the research group (in-plane pixel size: 0.525 mm; slice thickness: 1 mm; Rusli and Kedgley, 2020). The CT scan was imported into Mimics 24.0 (Materialize, Belgium) where the geometry of the first metacarpal, the second metacarpal and the trapezium were detected and segmented. The segmented bone geometries were then smoothed and converted into surface meshes in Geomagic Wrap 2017 (Artec 3D, Luxembourg). Smoothing removed surface irregularities from the segmented geometry, and the resulting surface mesh helped minimise element distortion during volumetric meshing.

As the soft tissues were not discernible in CT scans, cartilage and ligaments were modelled manually. The cartilage layers were extruded from the articular surface of the first metacarpal and the trapezium with a uniform thickness of 0.7 mm (Schneider et

al., 2017) in SolidWorks 2023 (Dassault Systèmes, France). Ligaments were created directly in Abaqus by no-compression spring elements distributed over their anatomical insertion regions. The number of spring elements per ligament therefore varied depending on the ligament width. Ligament insertion areas were determined by digitisation operators based on published anatomical descriptions (Bettinger et al., 1999; Ladd et al., 2012; Nanno et al., 2006). Finally, volumetric meshes were generated for all bone and cartilage geometries in Abaqus.

5.2.2. Position setup

The first metacarpal and the trapezium were initially positioned in neutral following the recommendation of the International Society of Biomechanics (ISB) (Wu et al., 2005). The neutral position is defined as the configuration in which the local coordinate systems of the first metacarpal and the trapezium are aligned. The ISB recommendations adopted the trapezium-based coordinate system and the description of TMC joint motion from the work of Cooney et al. (1981), while further supplementing and formalising the definition of the first metacarpal local coordinate system (Table 5.1).

However, the definition of the metacarpal coordinate system was not explicitly described, and the use of the terms “centre of the metacarpal head” and “centre of the metacarpal base” did not provide clear guidance on how these points were identified. Therefore, the surface-based method described by Halilaj et al. (2013) was adopted to define the first metacarpal coordinate system.

The articular surface nodes of the first metacarpal were imported into MATLAB R2023a (MathWorks, USA) and fitted with a fifth-order polynomial surface. The saddle point and central ridge of the articular surface were identified by calculating the surface gradient, and the principal curvature directions at the saddle point were used to define

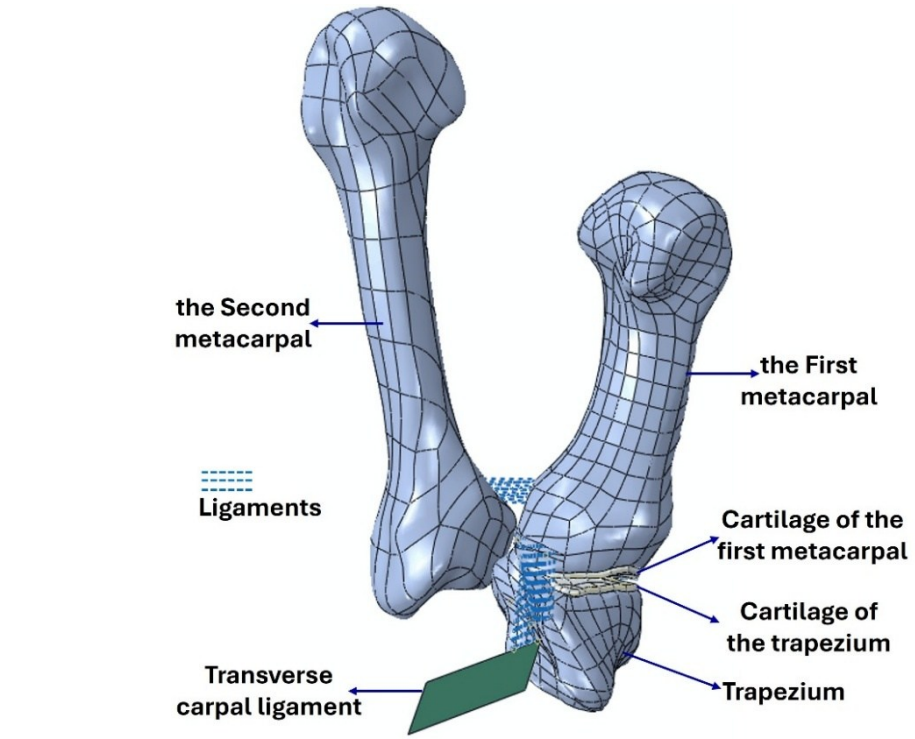
the metacarpal segment axis directions. The central ridge of the trapezial articular surface was identified with the same approach, and the local segment coordinate system of the trapezium was constructed following the ISB recommendation.

After neutral alignment, the first metacarpal was translated along the Y-direction to introduce a small gap between the metacarpal and trapezial cartilage surfaces, thereby preventing initial cartilage penetration. Three CT-scan based FE models in neutral position are shown in Figure 5.2

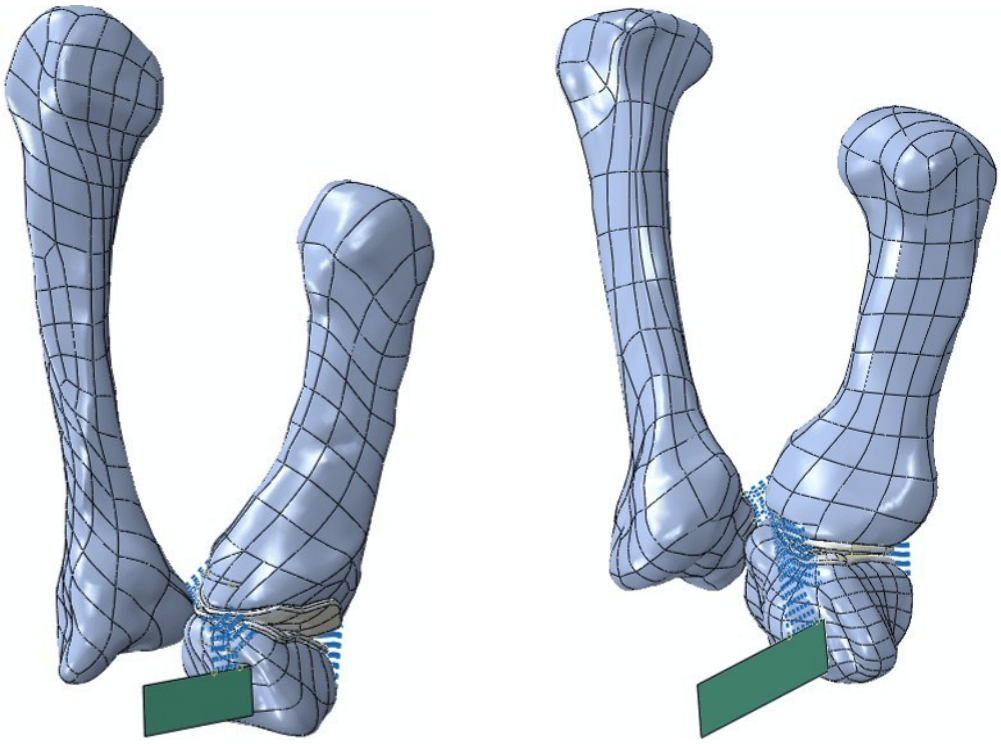
	The first metacarpal $\boldsymbol{SYS_{M1}}$	Trapezium $\boldsymbol{SYS_T}$
Origin	Midpoint of the line connecting the centre of the metacarpal base and the centre of the metacarpal head.	Midpoint of the central ridge.
X	Defined such that the X-Y forms the sagittal plane, dividing the first metacarpal into symmetric radial and ulnar halves.	Defined in the dorsal–volar direction, perpendicular to the central ridge and Y axis.
Y	Oriented parallel to the line connecting the centre of the distal metacarpal head to the centre of the metacarpal base, representing the longitudinal axis of the bone.	Defined as a proximodistal axis passing through the centre of the midpoint of the central ridge and the centre of the triscaphoid joint.
Z	Defined as the axis orthogonal to X-Y plane, completing a right-handed coordinate system.	Defined as orthogonal to X-Y plane and oriented approximately parallel to the central ridge.

*The central ridge refers to the ridge of the saddle-shaped trapezial articular surface that runs along the principal curvature direction and separates the concave and convex regions articulating with the base of the first metacarpal.

Table 5.1 Definitions of the local segment coordinate systems of the first metacarpal and the trapezium (Cooney et al., 1981; Wu et al., 2005).



(a)



(b) (c)

Figure 5.2 Geometry of the model components derived from (a) CT-scan 1, (b) CT-scan 2 and (c) CT-scan 3, represented as surfaces in Geomagic Wrap before meshing. The transverse carpal ligament is represented by the green shell, which was modelled as a rigid structure and served as a reference for the insertion of the ulnar collateral ligament.

5.2.3. Simulation type

The simulations were performed using an implicit dynamic solver, which was suitable for quasi-static analyses. This approach was adopted to improve numerical stability during contact interactions between the cartilage surfaces, particularly when large relative sliding and changing contact conditions were present. The applied displacements were prescribed gradually to minimise inertial effects.

5.2.4. Contact properties

Three contact interactions were defined in the FE model: two cartilage-bone interfaces and one cartilage-cartilage interface. The cartilage-bone contacts were modelled as tied constraints, preventing relative motion and penetration between the cartilage layers and their corresponding bony surfaces. The cartilage-cartilage contact was defined as a rough contact with a friction coefficient of 0.05 (Krakowski et al., 2024; Kurosawa et al., 2024), with penetration prohibited.

5.2.5. Material properties

5.2.5.1. Bone

The bones were assumed linear elastic, with the Young's modulus of 18 GPa and a Poisson ratio of 0.2 (Gislason et al., 2009).

5.2.5.2. Cartilage

Cartilage was also modelled as a linear elastic material, with a Young's modulus of 10 MPa and a Poisson's ratio of 0.49, despite its known hyperelastic and time-dependent behaviour (Yang et al., 2016). The objective of this study was to evaluate the sensitivity

of predicted cartilage stress distributions to modelling choices, including ligament delineation methods, geometry selection, and variability from digitisation operators. Consequently, the absolute magnitude of cartilage stress was not the primary outcome of interest. Instead, a consistent modelling framework was employed to enable comparison of relative stress magnitudes and spatial stress distributions of the cartilage across model variants.

5.2.5.3. Ligament

As reviewed in section 2.7.5.2, ligaments exhibit nonlinear mechanical behaviour, and there is currently no consensus dataset defining the stiffness of TMC ligaments. To address this, the present study combined the multi-stage nonlinear ligament description proposed by Carrigan et al. (2003) with the formulation introduced by (Gislason et al., 2009). Ligament force-strain behaviour was defined using Equation (5.1):

$$F = \begin{cases} \frac{a}{2\varepsilon_{ref}} \cdot x^2 & for\ 0 \le x \le \varepsilon_{ref} \\ ax - \frac{a\varepsilon_{ref}}{2} & for\ x > \varepsilon_{ref} \end{cases} \quad \text{Eq.5.1}$$

where a is a constant, F is the force, and x is the strain. ε_{ref} represents the nonlinear 'toe' region, which was 2% (Carrigan et al., 2003; Robi et al., 2013). When the strain is over 2%, it enters the linear zone.

Based on experimental findings reported by Bettinger et al. (1999) and Walker et al. (2025), ligament stiffness was assumed to be proportional to a geometric scaling factor representing the ratio of cross-sectional area to ligament length. This geometric term,

G, was defined as:

$$G = \frac{w_0 \times t_0}{l_0} \quad \text{Eq.5.2}$$

Where w_0, t_0 and l_0 represent width, thickness and length of ligament in the fully relaxed configuration, respectively. Ligament stiffness k was assumed to scale linearly with G.

The dimension and stiffness of the dorsal radial ligament (DRL) measured by Bettinger et al. (1999) were used as the reference values (Table 5.2)

Stiffness (N/mm)	Length (mm)	Width (mm)	Thickness (mm)
78.3	7.12	11.39	2.25

Table 5.2 Stiffness and dimensions of the dorsal radial ligament determined by Bettinger et al. (1999).

Accordingly, the stiffness k of each ligament was determined by scaling the DRL stiffness k_{DRL} using the corresponding geometric factor:

$$k = \frac{G}{G_{DRL}} k_{DRL} \quad \text{Eq.5.3}$$

At the transition point between the nonlinear and linear regions ($x = \varepsilon_{\text{ref}}$), Equation (5.1) yields:

$$F = ax - \frac{a\varepsilon_{ref}}{2} = \frac{a\varepsilon_{ref}}{2} \quad \text{Eq.5.4}$$

At the same strain level, the force can also be expressed using the linear stiffness definition:

$$F = k\varepsilon_{ref} l_0 \quad \text{Eq.5.5}$$

Equating these expressions gives:

$$a = 2kl_0 \quad \text{Eq.5.6}$$

Thus, the constant a for each ligament was determined directly from its scaled stiffness and relaxed length, ensuring that ligament force–strain behaviour was consistently defined based on both geometry and experimentally derived stiffness data.

The transverse carpal ligament (TCL) was represented as a shell structure. Although it did not directly constrain the TMC joint, it served as an anatomical reference for other

ligament attachments within the model; the ulnar collateral ligament (UCL), which is known to contribute to TMC-joint stability, was defined as inserting onto the TCL. The TCL was assumed to be rigid, as it was not a focus of the analysis.

5.2.6. Mesh

A mesh sensitivity test using CT-scan 1 (Figure 5.2 a) as a representative bone geometry was conducted by applying an axial displacement same as the pre-loading step on the first metacarpal with different element sizes of cartilage. Element sizes of 1.0 mm, 0.9 mm, 0.8 mm, 0.7 mm, 0.6 mm, 0.5 mm, 0.4 mm, 0.3 mm and 0.2 mm were tested.

5.2.7. Boundary conditions

The simulation consisted of three steps: contact, equilibration, and translation. In the first step, the gap preventing the penetration was closed to establish initial contact between the cartilage surfaces. In the second step, the Y-direction constraint was released, allowing the cartilage to relax to a state of just-contact. In the final step, the first metacarpal was translated in the volar and dorsal directions to assess whether cartilage stress distributions were consistent across different bone geometries, digitisers, and ligament delineation methods.

The trapezium and the second metacarpal were fully constrained throughout the simulation. During the contact step, the first metacarpal was displacement-controlled and translated proximally (positive Y-direction) by 2 mm to ensure contact between the two cartilage surfaces. In the equilibration step, all the constraints of the first metacarpal were removed, and the model reached the equilibrium with the two cartilages just in contact. Subsequently, two independent translation simulations were performed. In each simulation, the first metacarpal was translated by 2 mm in a single anatomical

direction, including volar and dorsal directions. The displacement was applied to a reference point (red cross) that was rigidly coupled to the top surface (highlighted in yellow) (Figure 5.3).

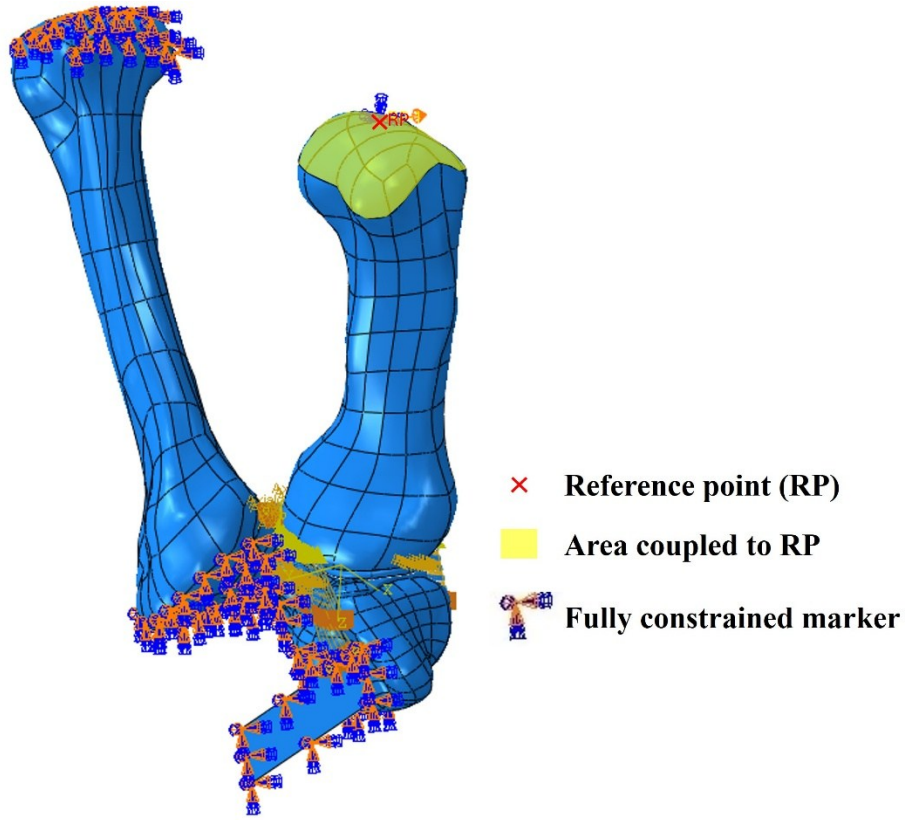


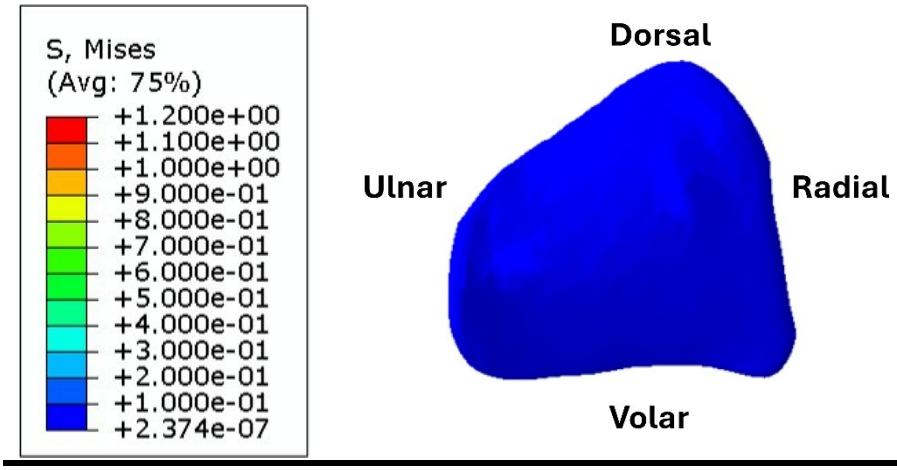
Figure 5.3 Boundary conditions of CT scan-3 during dorsal translation.

5.3. Results

5.3.1. Mesh sensitivity

It was found that when the element size was less than 0.5 mm, there was little difference in the stress distribution on the cartilage (Figure 5.4). For element sizes between 0.5 mm and 0.2 mm, the maximum von Mises stress varied by less than 2%. Consequently, the cartilage meshed with 10-node quadratic tetrahedral (C3D10) elements with element edge length of 0.5 mm. Because the stress over bones was not examined and to save the computational cost, the bones were meshed with 10-node quadratic

tetrahedral (C3D10) elements of 1.0 mm.



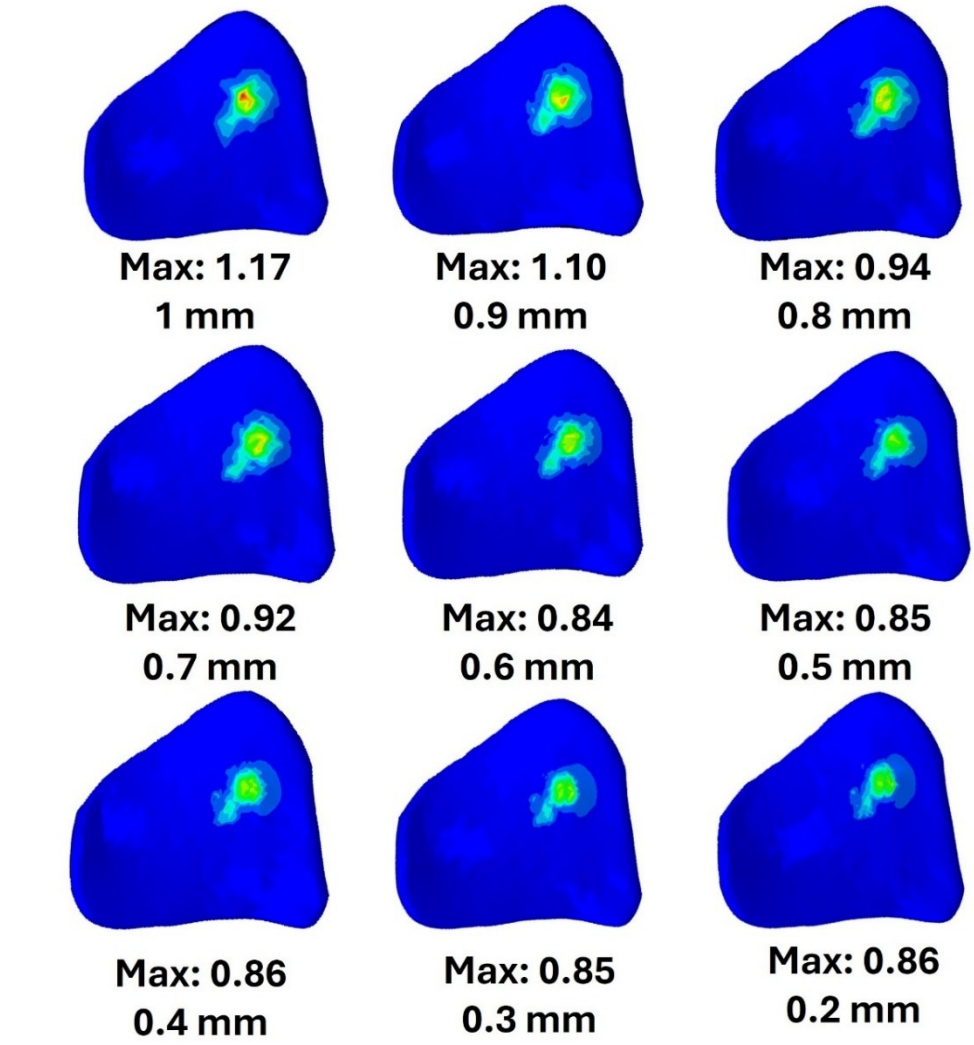


Figure 5.4 Stress distribution on the trapezial cartilage for CT-scan 1 with different mesh element sizes. Maximum stress (Max) is indicated in the unit of MPa.

5.3.2. Stress distribution of the trapezial cartilage

Figures 5.5–5.7 and Figures 5.8-5.10 illustrate the von Mises stress distribution on the trapezial cartilage following a 2 mm dorsal and volar translation, respectively, of the first metacarpal for the three CT-based geometries. To enable direct comparison, a consistent colour scale was applied across all models.

For a given ligament delineation method and CT-scan geometry, stress distributions were spatially similar across digitisation operators, with differences observed primarily in stress magnitude.

Although peak stress locations were similar across ligament delineation methods within the same CT scan, differences were observed in the spatial extent of high-stress regions. For example, in Figure 5.7 (CT-scan 1, volar translation), for digitisation operator 2, ligament delineation methods B and N produced comparable peak stresses (1.65 MPa and 1.64 MPa, respectively), while the high-stress region associated with method N was larger than that of method B. Similarly, in Figure 5.9 (CT-scan 3, volar translation), for digitisation operator 3, the method L produced a lower peak stress (1.13 MPa) than the N method (1.34 MPa), yet the associated high-stress region for the L method was broader, whereas the N method exhibited a more localised stress concentration.

CT-based bone geometry had a pronounced effect on both the distribution and magnitude of cartilage stress. During dorsal translation, CT-scans 2 and 3 exhibited high-stress concentrations predominantly in the volar-ulnar region of the trapezial cartilage, whereas CT-scan 1 showed peak stress primarily in the volar region. During volar translation, CT-scans 2 and 3 demonstrated high-stress regions on the dorsal side of the trapezial cartilage, while CT-scan 1 exhibited more centrally located stress concentrations.

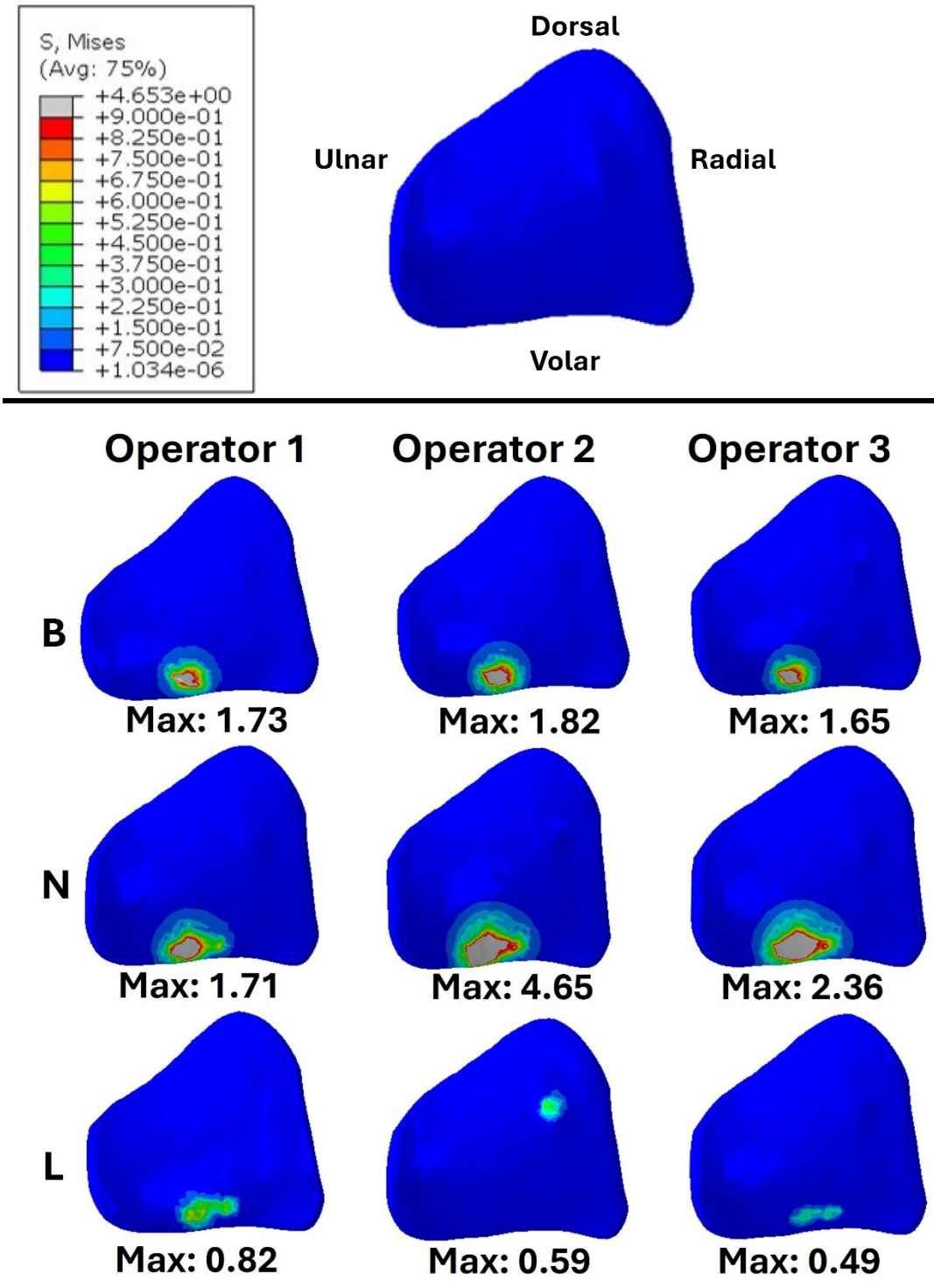


Figure 5.5 Stress distribution on the trapezial cartilage for CT-scan 1 after dorsal translation of 2 mm. From left to right, the results correspond to digitisation operators 1–3. From top to bottom, the results correspond to ligament delineation methods of Bettinger et al. (1999), Nanno et al. (2006) and Ladd et al. (2012). Maximum von Mises stress was indicated in the unit of MPa.

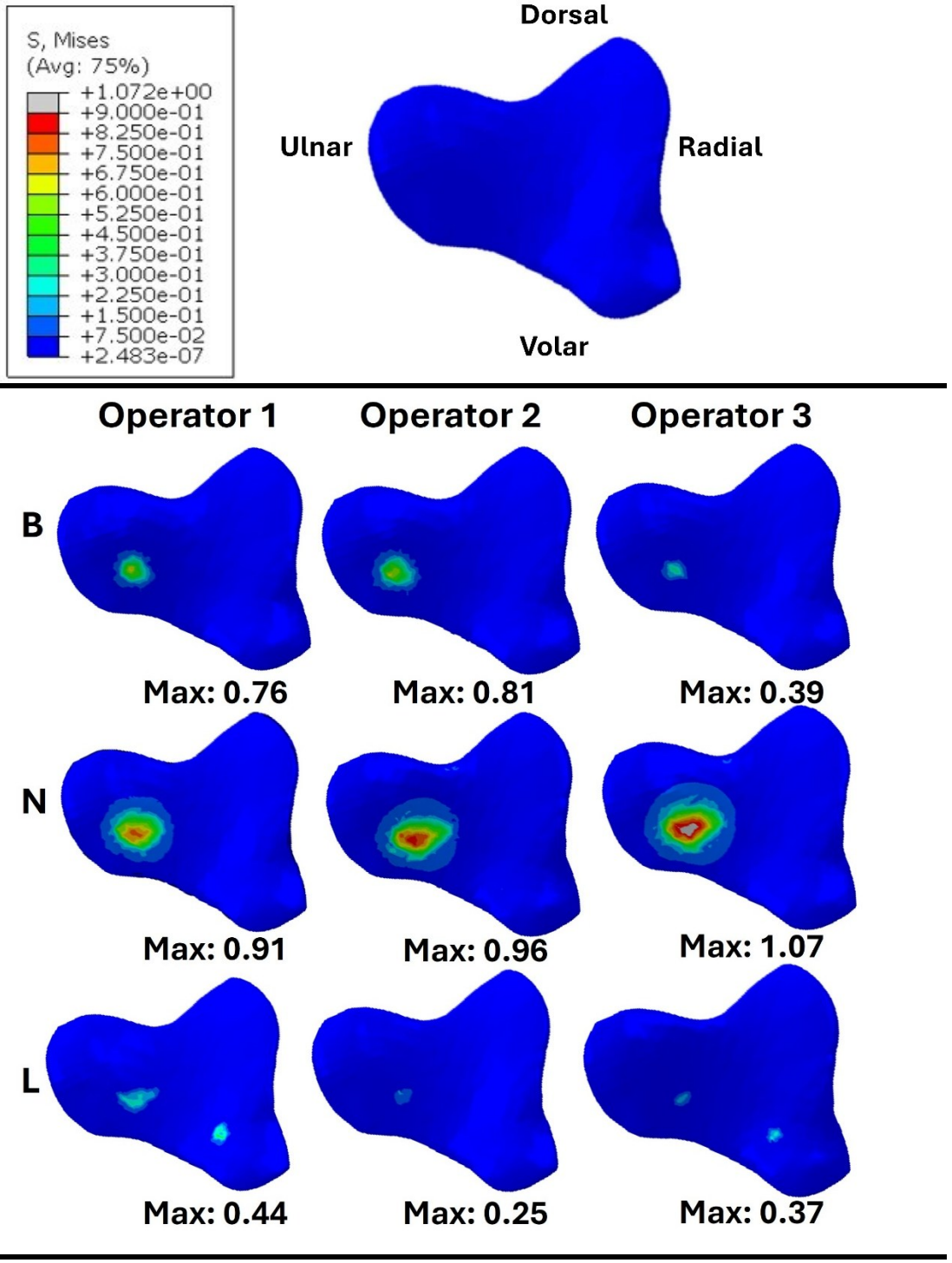


Figure 5.6 Stress distribution on the trapezial cartilage for CT-scan 2 after dorsal translation of 2 mm. From left to right, the results correspond to digitisation operators 1–3. From top to bottom, the results correspond to ligament delineation methods of Bettinger et al. (1999), Nanno et al. (2006) and Ladd et al. (2012). Maximum von Mises stress was indicated in the unit of MPa.

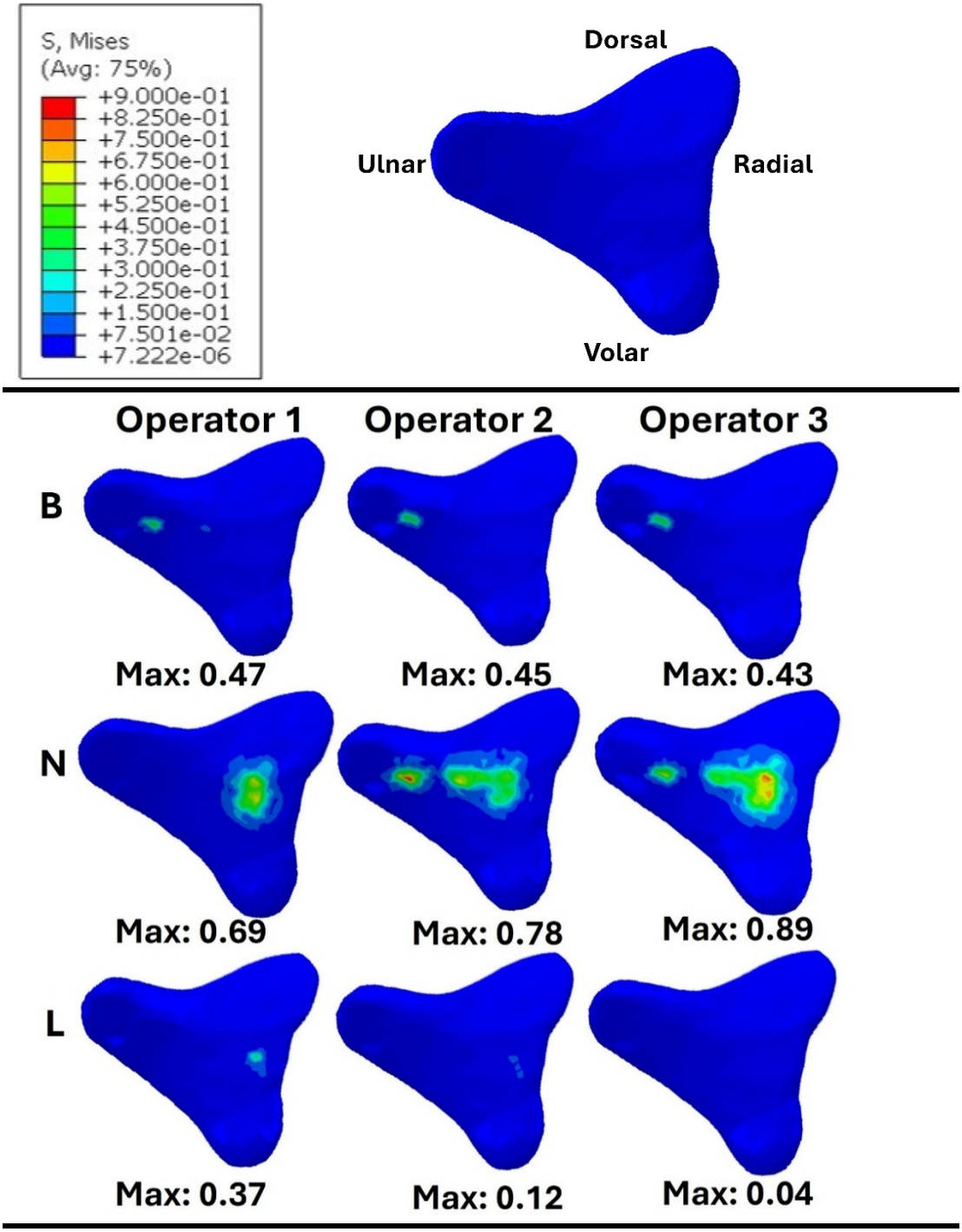


Figure 5.7 Stress distribution on the trapezial cartilage for CT-scan 3 after dorsal translation of 2 mm. From left to right, the results correspond to digitisation operators 1–3. From top to bottom, the results correspond to ligament delineation methods of Bettinger et al. (1999), Nanno et al. (2006) and Ladd et al. (2012). Maximum von Mises stress was indicated in the unit of MPa.

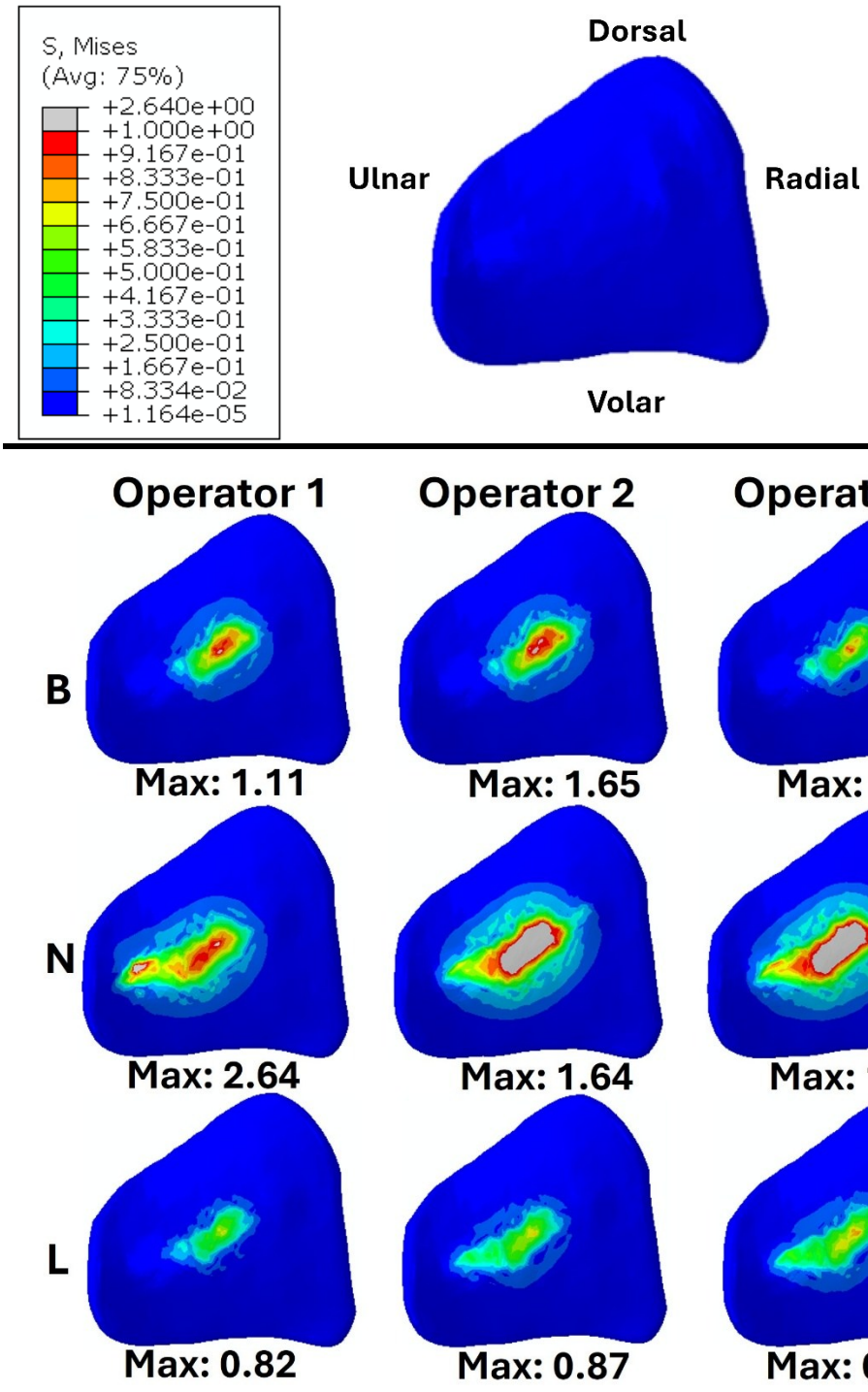


Figure 5.8 Stress distribution on the trapezial cartilage for CT-scan 1 after volar translation of 2 mm. From left to right, the results correspond to digitisation operators 1–3. From top to bottom, the results correspond to ligament delineation methods of Bettinger et al. (1999), Nanno et al. (2006) and Ladd et al. (2012). Maximum von Mises stress was indicated in the unit of MPa.

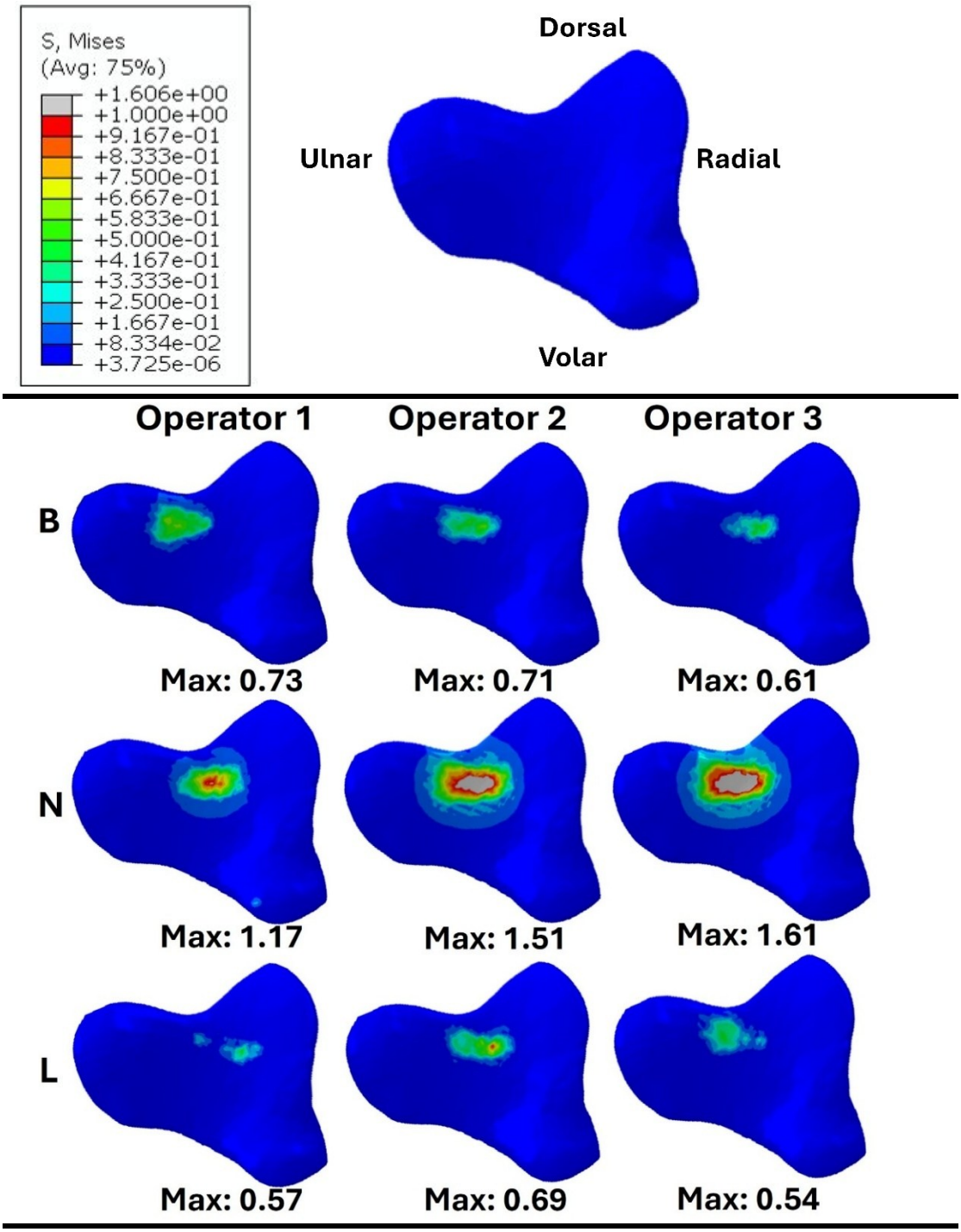


Figure 5.9 Stress distribution on the trapezial cartilage for CT-scan 2 after volar translation of 2 mm. From left to right, the results correspond to digitisation operators 1–3. From top to bottom, the results correspond to ligament delineation methods of Bettinger et al. (1999), Nanno et al. (2006) and Ladd et al. (2012). Maximum von Mises stress was indicated in the unit of MPa.

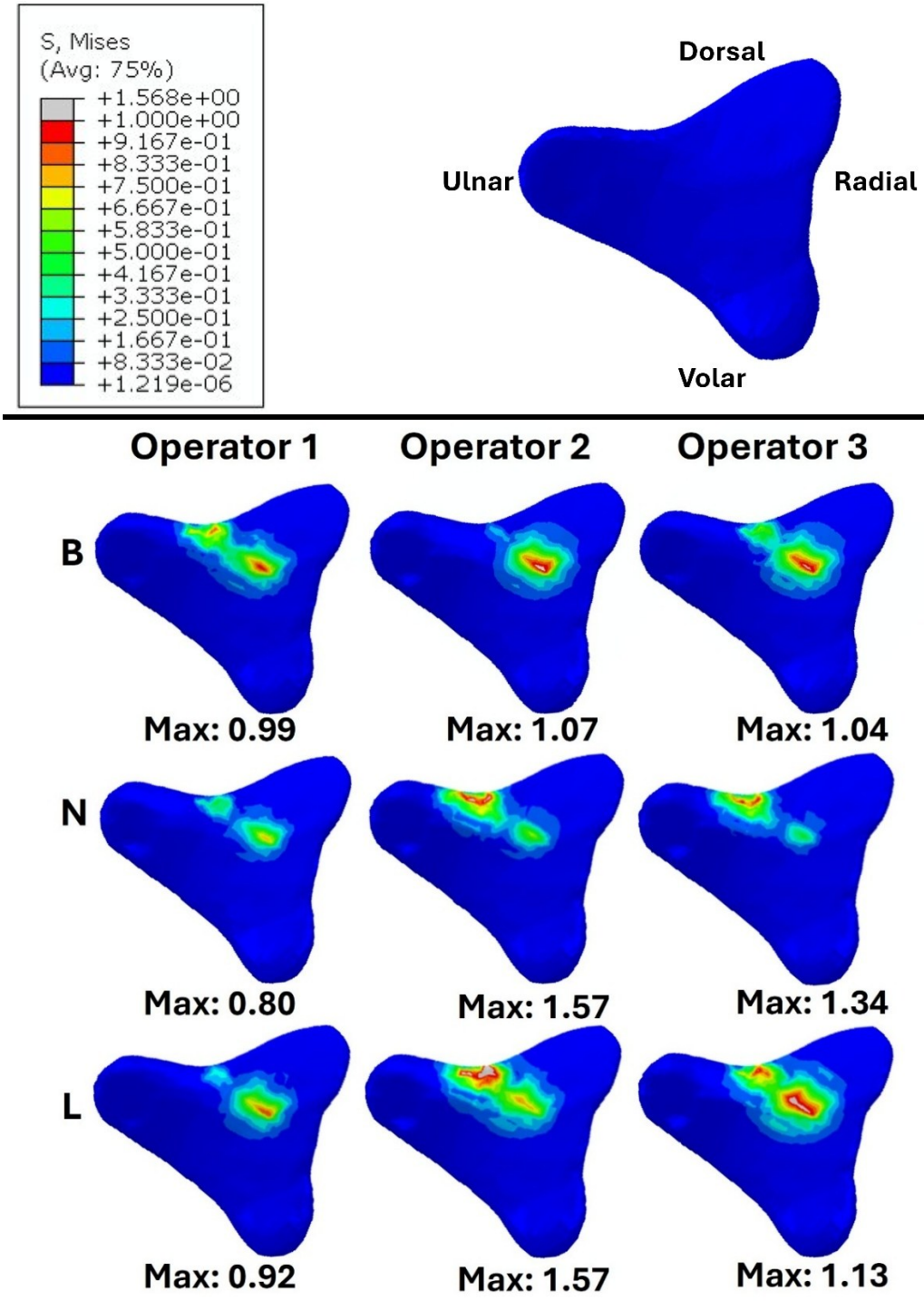


Figure 5.10 Stress distribution on the trapezial cartilage for CT-scan 3 after volar translation of 2 mm. From left to right, the results correspond to digitisation operators 1–3. From top to bottom, the results correspond to ligament delineation methods of Bettinger et al. (1999), Nanno et al. (2006) and Ladd et al. (2012). Maximum von Mises stress was indicated in the unit of MPa.

5.4. Discussion

Minimal variation in stress distribution across digitisation operators indicates that existing anatomical descriptions provide sufficient guidance for consistent ligament attachment placement. From a modelling perspective, the absolute magnitudes of FE-predicted cartilage stress cannot be directly interpreted as physiological values due to the simplified material representations and modelling assumptions. Instead, the model is most appropriate for use in evaluating relative differences in stress magnitude and spatial distribution. Under this framework, operator-dependent variability is unlikely to compromise comparative assessments of joint mechanics, and extensive operator-specific refinement is not required when the primary objective is to compare relative stress patterns within a consistent modelling approach.

Variations introduced by different ligament delineation methods primarily affected FE model predictions by altering both the mechanical properties assigned to individual ligaments and the manner in which these ligaments constrain relative bone motion. Differences in reported ligament numbers, and ligament dimensions directly affect ligament stiffness. In addition, variations in the anatomical descriptions of ligament insertion regions changed the spatial distribution of ligament constraints on the TMC joint, thereby influencing joint stability and load transfer. Furthermore, Bettinger et al. (1999) reported that the dAOL and the dIML were not present in all specimens, indicating inter-individual variability in the configuration of TMC ligaments. Collectively, these factors demonstrate that ligament delineation methods introduce variability in both ligament force generation and joint constraint, underscoring the importance of systematically evaluating ligament delineations when developing FE models of the TMC joint.

Cartilage stress predictions were highly sensitive to CT-based bone geometry, emphasising the dominant role of articular morphology in governing TMC joint contact mechanics. Variations in geometry led to substantial differences in the predicted

mechanical response. Previous morphological studies of the trapezium have identified three distinct categories of trapezial articular surface shape: quadrilateral, bean and heart (Flanagan et al., 2022). Based on this classification, the CT-based geometries studies in this study can be grouped accordingly, with CT-scan 1 corresponding to a bean-shaped trapezium, and CT-scans 2 and 3 corresponding to a heart-shaped trapezium. Notably, CT-scans sharing similar trapezial morphology exhibited comparable distribution patterns, whereas distinct shapes were associated with different locations and magnitudes of peak stress. These findings underscore the influence of trapezial shape on joint contact behaviour and reinforce the limitations of single-specimen or averaged geometries and support the use of subject-specific models when investigating TMC joint mechanics or comparing loading conditions across individuals.

A displacement-driven approach was adopted in this study in preference to a force-driven method, based on both physiological considerations and the availability of literature data. As outlined in Section 5.2, ligaments primarily function to constrain joint translation, and previous studies have reported physiological TMC-joint translations during daily activities of approximately 2 mm, providing a well-defined basis for prescribing displacement. In contrast, there was limited quantitative evidence regarding the force thresholds at which ligament constraints were engaged *in vivo*. Consequently, a force-driven approach would require additional assumptions regarding ligament properties and loading conditions, introducing greater uncertainty. Therefore, a displacement-driven approach was considered more appropriate, as it enables the model to be grounded in experimentally reported physiological constraints.

In this study, CT imaging was used to generate the geometric models, primarily due to its availability and suitability for capturing bony anatomy. However, CT provides limited contrast for soft tissues, and cartilage geometry therefore had to be defined based on assumptions rather than direct segmentation. Alternative imaging modalities, such as magnetic resonance imaging (MRI) or micro-computed tomography (μCT), offer improved soft tissue resolution and may enable direct visualisation of cartilage.

For example, MRI has been widely used to segment cartilage in larger joints such as the knee, providing subject-specific representations of articular cartilage (Satapure et al., 2017). Similar approaches could potentially be extended to the thumb, although the small size of the TMC joint presents additional challenges in resolution and image quality (Ikumi et al., 2022). While μCT can provide high-resolution imaging, its in vivo application is largely limited to small animal studies due to radiation dose and field-of-view constraints, and it is therefore more commonly used for ex vivo imaging of human tissues (Badea et al., 2008). In the present study, CT was selected as a pragmatic choice, but future work could explore MRI-based modelling to improve anatomical accuracy of cartilage representation.

5.5. Chapter conclusion

This chapter evaluated the sensitivity of FE models of the TMC joint to key modelling factors, including digitisation-operator variability, ligament delineation methods, and CT-based bone geometries. The results demonstrated that variation introduced by digitisation operators had a minimal influence on predicted cartilage stress distribution, indicating robustness of the modelling framework to operator-dependent ligament digitisation. In contrast, both ligament delineation method selection and specimen-specific bone geometry produced differences in predicted joint mechanics and therefore cannot be neglected.

Building on these findings, the FE models used in Chapter 6 to investigate joint mechanics during smartphone use will incorporate three CT-based bone geometries and three ligament delineation methods, enabling assessment of joint loading under functional conditions while accounting for the primary sources of modelling variability identified in this chapter.

Chapter 6

Finite element modelling of the trapeziometacarpal joint during smartphone typing and swiping

Building on the sensitivity analyses in Chapter 5, Chapter 6 focuses on simulating the trapeziometacarpal joint under loading conditions experienced during smartphone use. The primary aim is to investigate cartilage stress of the trapezial articular cartilage during typing and swiping activities. Boundary conditions for the simulations are derived from the thumb kinematics and kinetics measured in Chapter 4.

Nine finite element models developed in Chapter 5 are employed, comprising three CT-based geometries and three ligament delineation methods each. Cartilage stress distributions are presented and compared across loading conditions, geometries, and ligament delineation methods.

6.1. Introduction

Smartphone interaction has been characterised by repetitive thumb use, placing high mechanical demands on the TMC joint, which is clinically relevant as TMC osteoarthritis has been associated with elevated cartilage stress (Shi et al., 1995). FE modelling is particularly suited to characterising this problem, as it enables prediction and comparison of articular cartilage stress across loading conditions, which cannot be measured directly *in vivo* and are considered key mechanical factors associated with cartilage degeneration.

Limited studies have investigated the articular mechanics of the TMC joint using FE modelling. Schneider et al. (2017) developed population-based FE models to investigate sex- and age-related variations in TMC-joint contact area and peak stress location during isometric tasks, including pinch, grasp, and jar-twist tasks. More recently, muscle-driven FE thumb models have been used to study TMC contact stress during lateral pinch and to evaluate how therapy exercises and ligament reconstructive surgeries alter cartilage stress (Dong et al., 2023). Valerio et al. (2024) examined the effect of TMC-joint passive stiffness provided by the ligaments on cartilage stress during pinch, identifying joint hypermobility resulting from insufficient joint constraints as an osteoarthritis-relevant risk factor.

Overall, existing TMC FE studies have focused on pinch and grasp tasks, often in the context of ligament laxity or rehabilitation. To the authors' knowledge, there are no FE studies investigating contact stresses of the TMC joint due to smartphone activities. This Chapter applies experimentally measured smartphone-specific kinematics and kinetics to quantify trapezial cartilage stress under representative smartphone interaction conditions.

6.2. Method

The FE models used in this chapter were developed using the same modelling methodology described in Chapter 5, with modifications to simulate smartphone loading conditions.

As demonstrated in Chapter 5, the spatial distribution of cartilage stresses between digitisation operators were similar, but ligament delineation and anatomical variability were not. As the focus in this Chapter is the contact stresses due to smartphone-relevant loading, only models generated by a single digitisation operator were used. Three variations of anatomical geometries (CT scans 1–3) and three ligament delineation methods (B: Bettinger et al., N: Nanno et al., and L: Ladd et al.) were used to develop a total of nine FE models.

Based on the data from Chapter 4, differences between force-plate sizes were not significant; therefore, only data obtained using the medium-sized force plate were taken forward here to develop the FE models. Simulation conditions associated with extreme TMC-joint angles and high forces were selected. These included typing at key 1, typing at key 7, and swiping to the left. Typing at key 6 was included as a control condition, as joint angles were close to neutral and thumb forces were low compared to typing at other keys.

Each FE simulation represented a static loading condition defined by prescribed joint kinematics and the corresponding applied thumb force. For each loading condition, joint angles corresponding to the 75^{th} percentile of the kinematic dataset collected from 20 participants in Chapter 4 were applied (Table 6.1). The 75th percentile was selected to represent consistently high, yet physiologically plausible joint angles while reducing the influence of outliers.

In the adopted coordinate system, extension, abduction, and external rotation were defined as negative rotations (Figure 4.4). Therefore, when determining the 75th

percentile of these joint angles, absolute values were taken rather than signed values.

A full factorial design was employed, comprising three CT-based geometries, three ligament delineation methods, and four loading conditions, resulting in 3 × 3 × 4 = 36 FE simulations.

Condition	A-A (°)	I-E (°)	F-E (°)	F_x (N)	F_y (N)	F_z (N)
Typing at 6	-13	12	-1	-0.06	-0.31	0.58
Typing at 1	-36	11	-24	-0.36	-0.10	0.68
Typing at 7	-54	8	-31	-0.60	-0.20	0.36
Swiping to left	46	10	47	-0.61	-0.69	-1.41

*Angles and forces were expressed in the local coordinate system of the trapezium.

Table 6.1 Kinematic and kinetic boundary conditions of selected loading conditions, representing 75% joint angles used by the population assessed in Chapter 4 to achieve each task. A-A: adduction–abduction; I-E: internal–external rotation; F-E: flexion–extension.

6.2.1. Setup of relative bone orientation

As described in Chapter 5, the first metacarpal and the trapezium were initially positioned in a neutral position, defined as 0° for all joint angles, following the recommendations for coordinate-frame creation and joint-angle calculation prescribed by the International Society of Biomechanics (ISB) (Wu et al., 2005). To simulate the loading conditions described in Table 6.1, TMC-joint angles were achieved by rotating the first metacarpal relative to the trapezium prior to the simulation.

Elemental rotations of Euler angles can be defined as either extrinsic or intrinsic. In an extrinsic representation, rotations are applied about the axes of a space-fixed reference frame, which remains stationary throughout the motion. In contrast, intrinsic rotations are applied about the axes of a body-fixed frame, which rotates with the moving body and changes orientation after each rotation.

Although the ISB recommendations defined TMC joint angles using a body-fixed

reference frame, implementing intrinsic rotations would complicate the practical application of rotations within the FE environment. Therefore, in this study, rotations were implemented using the space-fixed frame, in which the local coordinate system of the trapezium was aligned with the global coordinate system in Abaqus. All rotations were applied from the neutral position and executed sequentially about the fixed axes of the trapezium-embedded frame, such that each rotation component represented a consistent anatomical motion direction independent of prior rotations. It should be noted that, regardless of whether a space-fixed or body-fixed reference frame was used, the final joint orientation and, thus, the simulation results, remain unchanged; only the sequence of rotations differed. A small gap between the first metacarpal and the trapezium was left to ensure there was no penetration between bones. As the cartilage layers were generated manually, the geometries of the opposing cartilage surfaces did not articulate with each other perfectly, and the gap could ensure a well-defined contact interaction during the simulation. Figure 6.1 shows the position setup of four loading conditions illustrated by CT-scan 1.

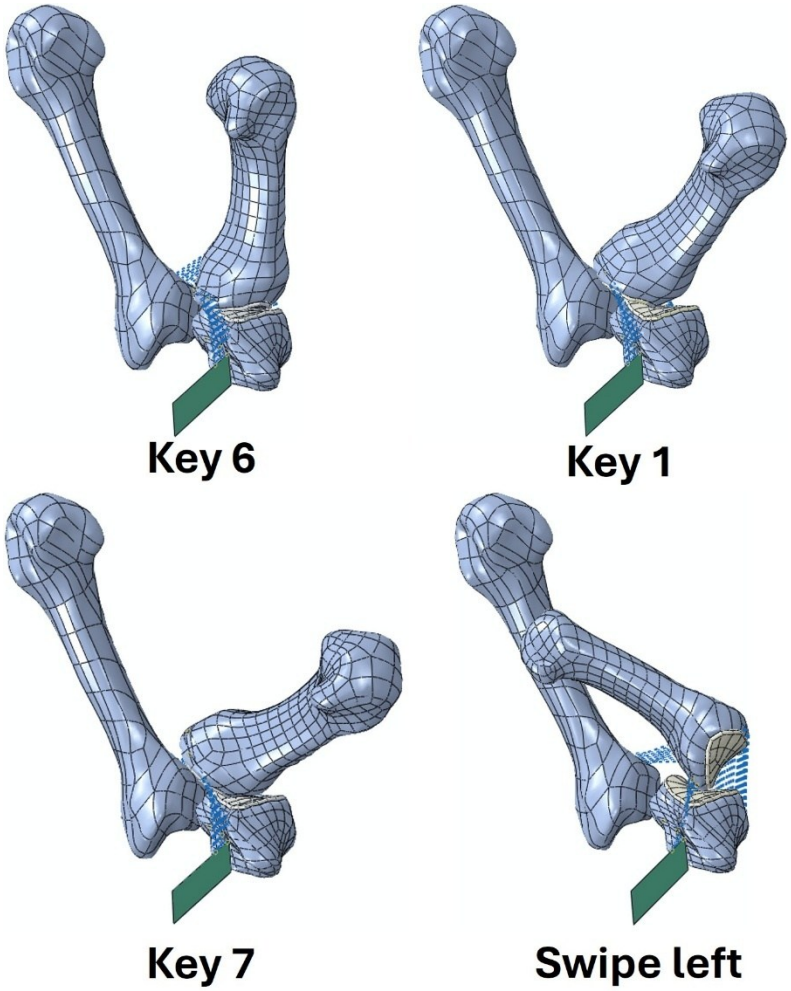


Figure 6.1 Prescribed trapeziometacarpal joint kinematics used in the finite element simulations for the four loading conditions: typing at key 6, typing at key 1, typing at key 7, and swiping to the left.

6.2.2. Boundary conditions

All prescribed motions and forces were defined in the local coordinate system of the trapezium. The trapezium and the second metacarpal were fixed throughout the simulation. The relative angles between the trapezium and the first metacarpal were set to reproduce the TMC joint kinematics measured in Chapter 4; therefore, rotations of the first metacarpal were constrained. Translational degrees of freedom of the first

metacarpal were left unconstrained to allow joint seating under the combined effects of contact and ligament constraints.

Forces measured at the thumb tip in Chapter 4 were transformed into the local coordinate system of the trapezium and applied to the first metacarpal. The force measured by the force plate was denoted as F^{FP}, where the superscript indicates the coordinate system in which the force vector is expressed. The rotation matrix R_B^A was defined as the transformation that expresses a vector from coordinate system B in coordinate system A. Accordingly, the rotation matrices relating adjacent segments in the kinematic chain were defined as R_{FP}^{DP}, R_{DP}^{PP}, R_{PP}^{Meta}, and R_{Meta}^{Trap}, representing transformations from the force plate to the distal phalanx, distal phalanx to proximal phalanx, proximal phalanx to first metacarpal, and first metacarpal to trapezium coordinate systems, respectively.

The orientation of the trapezium coordinate system expressed in the force-plate coordinate system was obtained by successive multiplication:

$$R_{FP}^{Trap} = R_{Meta}^{Trap} \times R_{PP}^{Meta} \times R_{DP}^{PP} \times R_{FP}^{DP} \quad \text{Eq.6.1}$$

The force expressed in the trapezium coordinate system was then calculated as:

$$F^{Trap} = R_{FP}^{Trap} \times F^{FP} \quad \text{Eq.6.2}$$

All rotation matrices described above were obtained from the thumb kinematic and kinetic data collected in Chapter 4.

A reference point (RP) (red cross) was defined at the centre of the first metacarpal head, and the metacarpal head surfaces (shaded in yellow) were rigidly tied to this RP, forming a rigid body. The transformed forces (Table 6.1) were then applied to the RP, ensuring uniform load transfer to the first metacarpal. Figure 6.2 shows an example using CT scan 1 under the typing-at-key-6 loading condition.

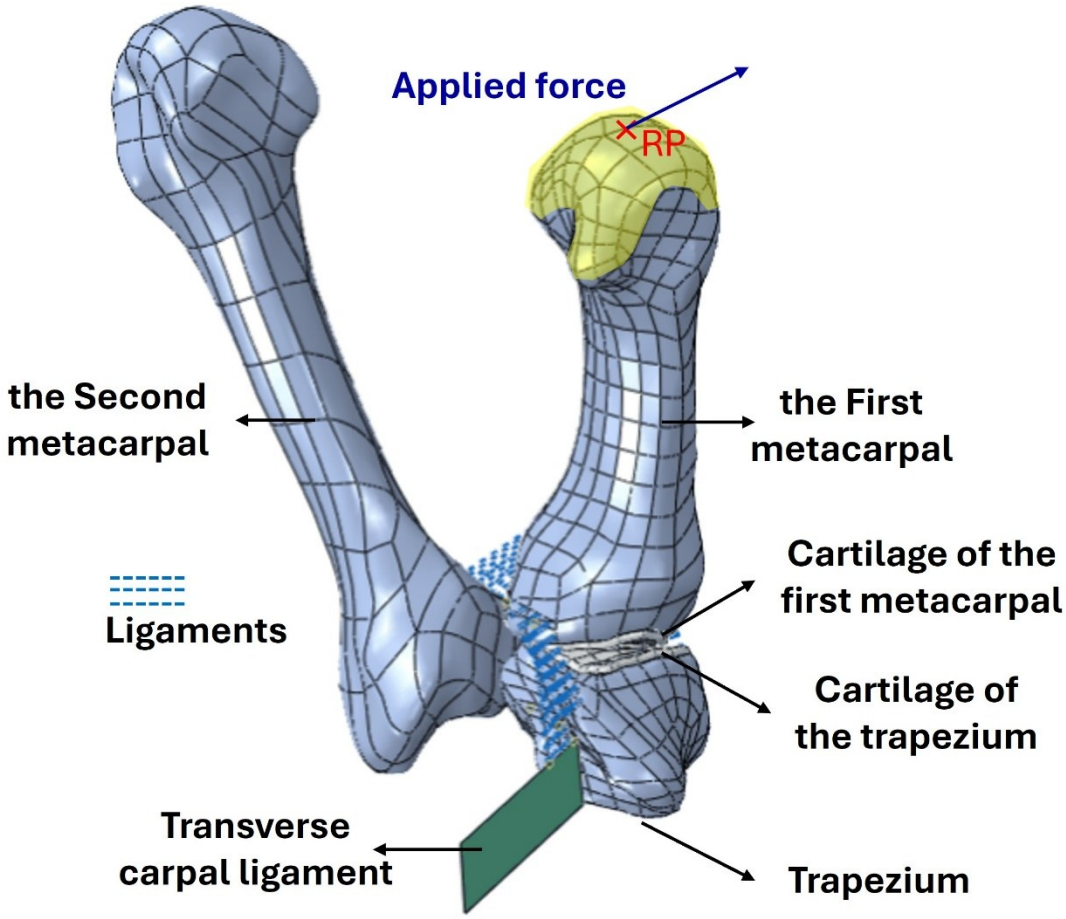


Figure 6.2 Demonstration of the reference point (red cross) and rigid coupling of the first metacarpal head surface (yellow shade) in the FE model shown as surfaces in Geomagic Wrap before meshing. The transverse carpal ligament is represented by the green shell, which was modelled as a rigid structure and served as a reference for the insertion of the ulnar collateral ligament.

6.2.3. Analysis

The FE results were analysed by examining the von Mises stress distribution on the trapezial articular cartilage for each simulation. The magnitude of the maximum cartilage stress was identified, and the location of peak stress on the articular surface was recorded. In addition, the spatial extent of regions exhibiting relatively high stress was assessed qualitatively to characterise differences in stress-distribution patterns.

6.3. Results

Figures 6.3–6.5 present the von Mises stress distribution on the trapezial cartilage for CT scans 1–3 under four smartphone loading conditions (typing at keys 6, 1, and 7, and leftward swiping) and three ligament delineation methods (B, N, and L). Distinct differences in stress magnitude and distribution were observed between loading conditions.

Typing at key 6 consistently resulted in low stress magnitudes across all simulations, with peak values of 0.62–1.39 MPa for CT scans 1–2 and 0.79–1.70 MPa for CT scan 3.

Typing at key 1 consistently produced higher maximum stress magnitudes than typing at key 6 except for CT-scan 2 when using ligament delineation method L; Peak stresses ranged from approximately 0.9–1.9 MPa for CT scan 1, 0.9–1.1 MPa for CT scan 2, and 2.3–2.7 MPa for CT scan 3, indicating moderate cartilage loading compared with the more extreme conditions including typing at 7 and swiping to left.

Typing at key 7 and leftward swiping consistently produced the highest cartilage stresses. For typing at key 7, peak stresses ranged from approximately 2.2–2.5 MPa in CT scan 1, 1.6–2.3 MPa in CT scan 2, and 1.9–3.2 MPa in CT scan 3. Leftward swiping generated comparable or higher peak stresses, with values reaching approximately 1.7–3.6 MPa in CT scan 1, 1.4–2.2 MPa in CT scan 2, and up to 5.2 MPa in CT scan 3.

Across all bone geometries and loading conditions, ligament delineation methods B and N demonstrated highly consistent stress distribution patterns, with similar locations and relative magnitudes of peak stress. In contrast, ligament delineation method L exhibited greater variability under specific conditions. For CT scan 2 with method L, typing at key 6 produced higher stress than typing at key 1, which differed from the trend observed in the other ligament delineation methods. For CT scan 3, method L also

resulted in a different stress distribution pattern during typing at key 7 compared with methods B and N.

Across different bone geometries, the location of peak stress varied for the same loading condition. For example, during typing at key 7, peak stress was centrally located in CT scans 1 and 3 but shifted towards the volar region in CT scan 2. When swiping to the left, peak stress was located on the volar side of the trapezial cartilage in CT scans 2 and 3, whereas a more central stress concentration was observed in CT scan 1.

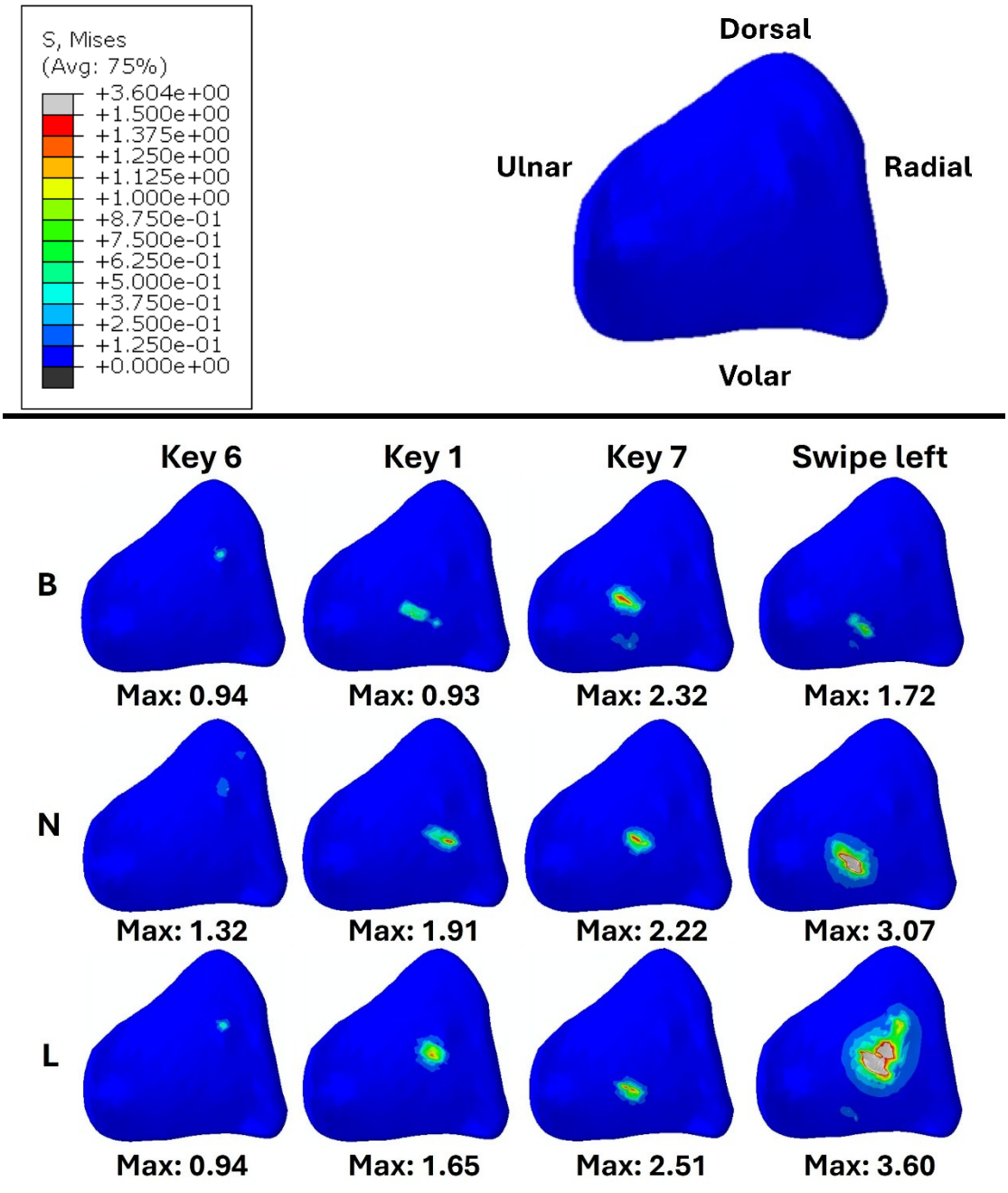


Figure 6.3 Stress distribution on the trapezial cartilage for CT-scan 1 during different loading conditions. From left to right, the results correspond to loading conditions: typing at key 6, key 1, key 7 and swiping to left. From top to bottom, the results correspond to ligament delineation methods of Bettinger et al. (1999), Nanno et al. (2006) and Ladd et al. (2012).

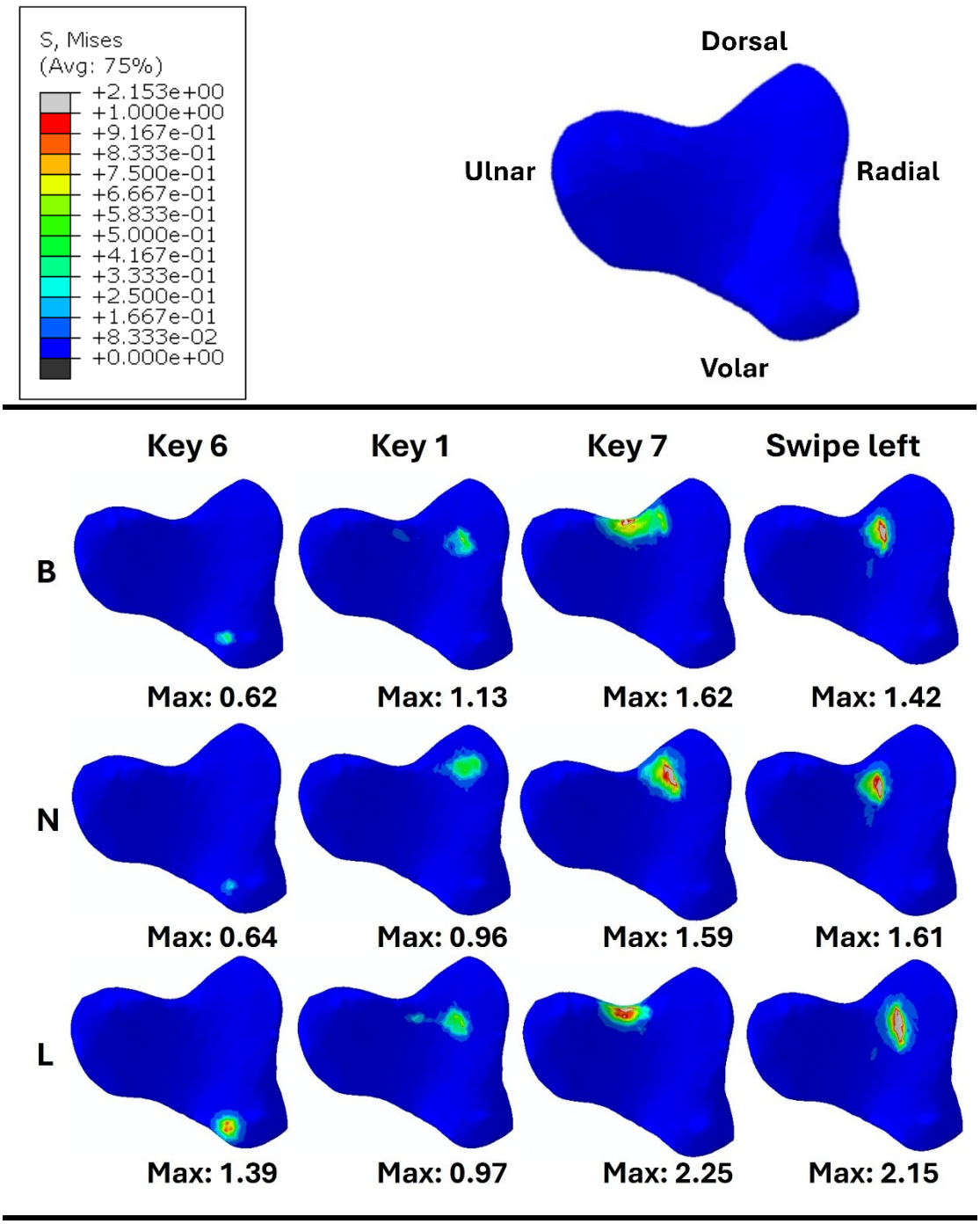


Figure 6.4 Stress distribution on the trapezial cartilage for CT-scan 2 during different loading conditions. From left to right, the results correspond to loading conditions: typing at key 6, key 1, key 7 and swiping to left. From top to bottom, the results correspond to ligament delineation methods of Bettinger et al. (1999), Nanno et al. (2006) and Ladd et al. (2012).

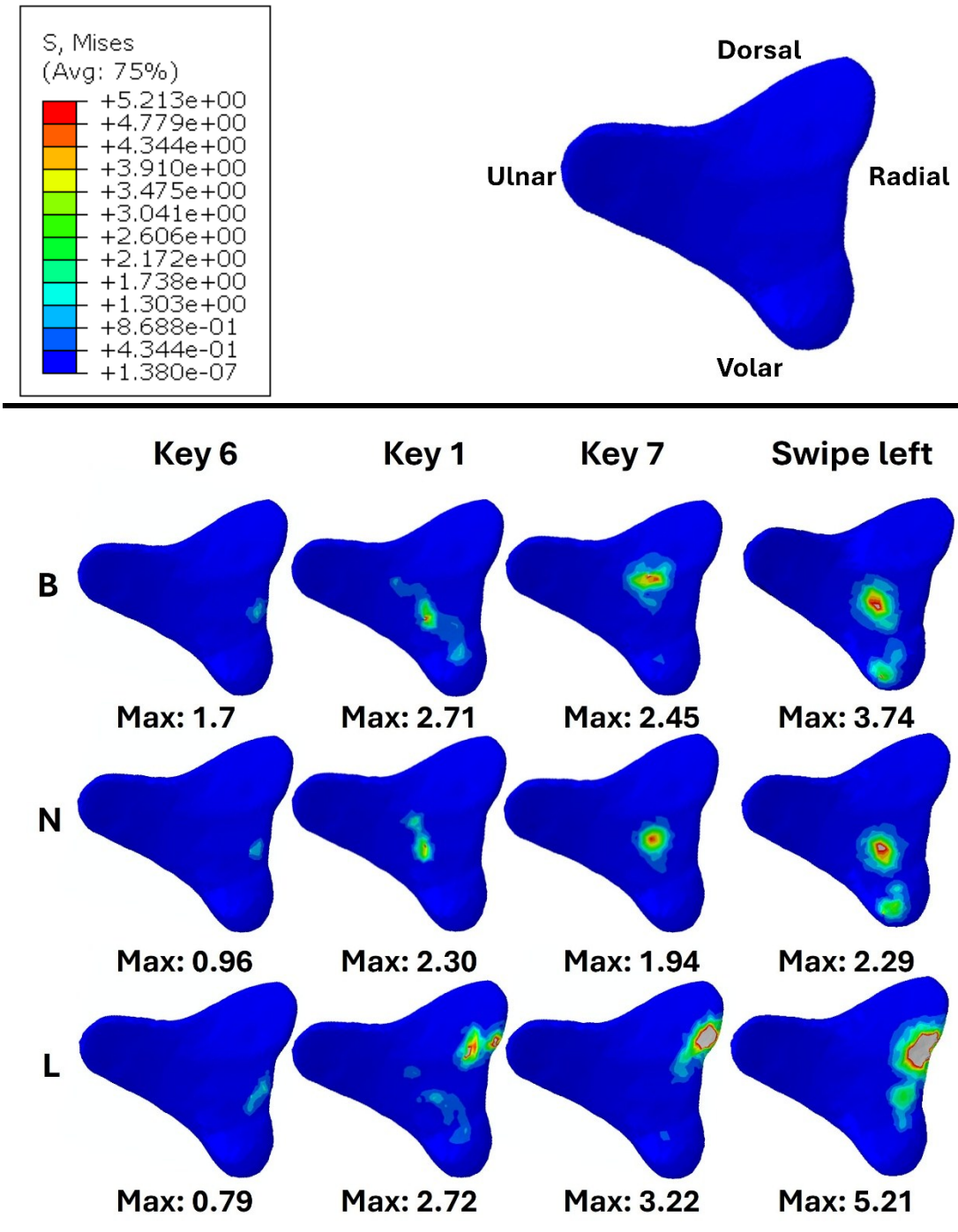


Figure 6.5 Stress distribution on the trapezial cartilage for CT-scan 3 during different loading conditions. From left to right, the results correspond to loading conditions: typing at key 6, key 1, key 7 and swiping to left. From top to bottom, the results correspond to ligament delineation methods of Bettinger et al. (1999), Nanno et al. (2006) and Ladd et al. (2012).

6.4. Discussion

6.4.1. Evaluation of variability in ligament delineation methods

When different ligament delineation methods were applied within the FE models of this study, the resulting predictions of joint contact stress were not always consistent. Ligament delineation methods B and N produced similar stress patterns across loading conditions, whereas method L yielded differing predictions, including reversals in the relative ranking of stress magnitude under certain conditions. As discussed in Chapter 5, these delineation methods differ in both the number of TMC ligaments represented and their geometric dimensions, which directly affect ligament stiffness and overall joint stability. In particular, method L does not include the dAOL or dIML, but instead includes the DCL, which is not represented in methods B and N; this difference may contribute to the observed discrepancies in stress predictions. However, due to the lack of definitive experimental validation, it is not possible to determine which ligament delineation method provides the most accurate representation. Nevertheless, these findings demonstrate that ligament delineation can influence simulation outcomes, highlighting the need for further studies to establish comprehensive and validated TMC ligament definitions.

6.4.2. Evaluation of variability in CT-scan based geometry

The geometry of the FE model played a central role in determining the location of peak stress. Variations in bone geometry influenced the shape of the articular surface and, consequently, the contact mechanics at the joint. In addition, joint alignment was affected by geometry, as the local segment coordinate systems of the first metacarpal and trapezium were defined based on bony landmarks that vary between individuals. Consequently, rotations applied between these segment coordinate systems may introduce inconsistencies across different CT-scan based geometries.

6.4.3. Risk of osteoarthritis

Previous research has shown that one-handed smartphone interactions involve substantial thumb movement and muscle activation, particularly when reaching for keys or performing complex touch tasks (Xiong and Muraki, 2014). These hand postures correspond to the more extreme kinematics at the TMC joint associated with higher stress on the articular surface observed in this study. With similar magnitudes of the force applied to the thumb, typing at key 7 and leftward swiping, which involved more extreme TMC joint angles compared with typing at key 1 and typing at key 6, consistently produced higher stress. This indicates that increasingly extreme joint postures lead to a mechanically less favourable loading condition at the TMC joint.

These findings suggest that applying loads in extreme TMC joint kinematics may alter joint congruency and contact mechanics, concentrating load over smaller regions of cartilage and increasing peak stress. Such stress concentrations are considered relevant to osteoarthritis development, as excessive articular stresses have been widely implicated in cartilage degeneration and osteoarthritis progression (Buckwalter et al., 2013).

6.4.4. Ergonomic implication

From an ergonomic perspective, these results highlight the potential benefit of interface layouts that minimise the demand for large thumb excursions, especially during repetitive tasks such as typing. Placing frequently used keys or interactive regions within the natural reach envelope of the thumb or encouraging two-handed device handling, may help reduce exposure to extreme TMC joint angles. Similarly, usage strategies that limit prolonged or repetitive one-handed interaction, may contribute to reduced cumulative joint loading.

While this work focused on a standard QWERTY keyboard layout, alternative input systems used in other languages, such as Mandarin, may involve different interaction patterns. For example, commonly used Chinese input methods employ a 9-key layout in which multiple letters are grouped under a single key and are used in combination with word prediction, allowing input over a larger touch area and reducing the need for precise finger movements. In addition, predictive text can reduce typing frequency by minimising the number of required key presses. These differences may influence thumb kinematics and loading patterns. Future studies should investigate how such input methods affect thumb biomechanics and TMC joint loading.

6.4.5. Exclusion of muscle force

A limitation of this study is that the FE model was not muscle-driven, and muscle forces acting across the TMC joint were not included. Instead, joint kinematics were prescribed to reproduce thumb postures identified from the experimental data, and joint rotations were fixed during each simulation.

Although muscle forces can be estimated using MSk models and applied to FE analyses, existing MSk models have been primarily validated for static or isometric tasks such as pinch and grip (Barry et al., 2018; Dong et al., 2023; McFarland et al., 2023), Their applicability to dynamic, low-force, multi-directional activities such as smartphone typing and swiping remains limited and typically requires task-specific muscle-activation data. As electromyography (EMG) data were not collected in this study, reliable estimation of muscle forces during smartphone interaction was not possible, and a muscle-driven modelling approach was therefore not adopted. Future work integrating validated MSk-FE frameworks and smartphone task-specific EMG measurements may enable more physiologically comprehensive simulation of the TMC joint during smartphone activities.

6.4.6. Exclusion of resulting moment

Force application at the thumb tip can generate additional moments at the TMC joint. In the present study, these moments were not included, based on the modelling approach adopted. The simulations were kinematically prescribed, with rotational degrees of freedom constrained. Under these conditions, externally applied moments did not alter the joint kinematics, as rotational motion was fully restricted. Therefore, these moments did not affect the defined loading condition and were not explicitly applied. This was consistent with the primary objective of the study, which was to evaluate the stress distribution under prescribed kinematic conditions.

Nevertheless, neglecting the moment component may influence the stress distribution within the joint. This represents a modelling simplification and should be acknowledged. Future work could incorporate both force and moment components, for example through MSk modelling, which can estimate the muscle forces acting on the bones to drive the joint to the prescribed kinematic conditions, thereby providing a more comprehensive representation of joint loading.

6.4.7. Material property

A range of material modelling options exists for both ligaments and articular cartilage, including nonlinear, viscoelastic, and biphasic formulations, as reviewed in Chapter 2. In this study, simplified material models were adopted for both tissues to support the primary objective of comparative analysis across loading conditions, bone geometries, and ligament delineation methods. Ligament properties were defined based on the stiffness of a reference ligament (DRL), with stiffness scaled according to ligament dimensions to ensure consistency when evaluating different delineation methods. Articular cartilage was modelled as linear elastic, providing a computationally efficient

representation suitable for relative comparisons of stress distribution. However, if actual stress magnitudes or time-dependent tissue responses become a primary focus, future work should consider incorporating nonlinear or viscoelastic material models to more accurately capture the mechanical behaviour of ligaments and cartilage.

6.4.8. Representation of loading conditions

The swiping motion in this study was represented using discrete static loading conditions corresponding to selected joint configurations during touchscreen interaction. While this approach enabled controlled evaluation of joint stress at the moment of contact, it did not capture the full biomechanical demands of the swiping motion. During swiping, the thumb underwent large kinematic excursions even when not in contact with the screen, which were driven by muscle forces. As such, biomechanical loading may arise not only from contact forces but also from the muscle forces associated with moving the thumb through extreme postures. Consequently, approaches that consider only contact-based loading are likely to underestimate the cumulative joint loading and potential overuse during repetitive touchscreen interactions.

Therefore, alternative approaches could model the swiping motion as a continuous process, incorporating time-dependent kinematics and muscle-driven loading. For example, MSk modelling could be used to estimate muscle forces throughout the movement, which could then be applied to FE models to evaluate joint loading across the entire motion.

However, such approaches would introduce additional complexity and uncertainty, particularly as appropriate MSk models of the thumb are not well established. In the present study, a static approach was adopted to enable systematic comparison of joint stress under controlled conditions.

6.5. Chapter conclusion

This chapter completed the study objective by simulating high-risk smartphone loading conditions identified from the kinetic and kinematic dataset in Chapter 4. The FE analyses demonstrated that thumb kinematics strongly influenced articular stress at the TMC joint. Loading conditions involving more extreme joint angles produced higher articular cartilage stresses than near-neutral postures, indicating an increased risk of TMC osteoarthritis. These findings underline the importance of smartphone interface layout and device shape in reducing extreme thumb kinematics, which may be explored further in future research. The following Chapter synthesises the key findings of this thesis, discusses their implications and limitations, and outlines directions for future research.

Chapter 7

Summary, Discussion, and Future Work

Chapter 7 summarises the research presented in this thesis and discusses its findings. It then outlines future research directions to improve understanding of the trapeziometacarpal joint loading during smartphone use and to guide the development of practical ergonomic interventions.

7.1. Summary

This thesis investigated how smartphone activities influence the mechanical loading of the TMC joint, which is located at the base of the thumb, and which allows the large range of the thumb motion. During smartphone use, the thumb is primarily engaged in navigation rather than its traditional stabilising role in tasks such as gripping; this increased range of motion and repetitive use may elevate joint contact stress and contribute to the development of osteoarthritis. Accordingly, a comprehensive methodological framework was developed that combined *in vivo* measurement of kinematics and kinetics of the thumb with FE analysis.

A thorough review of existing literature identified several limitations that motivated the thesis. First, despite growing concern regarding thumb osteoarthritis associated with repetitive touchscreen interactions. No experimental studies have directly measured cartilage stresses *in vivo*. FE simulations therefore provide an appealing approach for examining contact stress within the TMC joint. FE analyses require synchronised acquisition of thumb joint kinematics and thumb-tip forces to define physiologically relevant boundary conditions. However, no existing device allowed for accurate capture of low-magnitude fingertip forces during touchscreen interaction without compromising natural hand posture. This highlighted the need for a customised force plate that could resolve thumb forces while closely replicating the size, weight, and feel of an actual smartphone. During model development, inconsistencies in ligament descriptions across anatomical studies emerged as a critical source of uncertainty, and documented variability in bone geometry was expected to introduce further modelling ambiguity. As a result, it was necessary to systematically assess the sensitivity of FE model predictions to these anatomical and methodological uncertainties before applying the model to simulate smartphone-related loading conditions.

A novel experimental platform was designed, constructed, and calibrated to replicate

the size and handling characteristics of a typical smartphone while enabling accurate kinetic data collection. FE analysis was employed to optimise structural stiffness and strain gauge placement. Validation experiments confirmed that the device could resolve thumb forces with high sensitivity and low crosstalk. The resulting system enabled synchronised measurement of interaction forces and motion capture, laying the foundation for realistic boundary conditions in downstream computational modelling of TMC joint loading.

Kinematic and kinetic data were collected using a motion capture system and the custom-designed force plate to quantify thumb joint angles and interaction forces during representative smartphone tasks including typing and swiping. This integrated dataset enabled simultaneous characterisation of thumb movement patterns and external loading, providing physiologically realistic boundary conditions for subsequent FE simulations of TMC joint mechanics during smartphone use.

Before applying the FE models to smartphone-use conditions, the sensitivity of model predictions to key uncertainties was evaluated, including variability in ligament definition across anatomical datasets, digitisation-operator interpretation of ligament attachment sites, and differences in CT-based bone geometry. These analyses quantified how each factor influenced the predicted articular cartilage stress distribution, demonstrating that ligament dataset selection and anatomical variability in terms of bone geometry were influential parameters that should be carefully controlled. Conversely, digitisation-operator differences had minimal impact on joint mechanics and therefore were not considered in subsequent smartphone-loading simulations.

Four representative smartphone-use conditions were simulated using the FE method; these included three cases characterised by large TMC-joint angles and high applied forces to the thumb, and one near-neutral condition which was selected as a control case. By comparing the resulting von Mises stress distributions on the articular cartilage, the simulations showed that the studied cases generated higher cartilage stresses than

the control condition; this was consistent across the three joint geometries tested. This finding suggests that the specific interactions with the smartphone put an increased mechanical demand on the TMC joint and so, potentially, put it at a high risk of developing TMC osteoarthritis. These findings also highlight the importance of ergonomic smartphone interface design, particularly the arrangement and reachability of touchscreen buttons, and provide biomechanical guidance for designing more user-friendly device layouts.

7.2. Discussion and future work

7.2.1. Ligament dataset refinement

The sensitivity of cartilage stress predictions to the ligament delineation method observed in this thesis reflects an issue of variability in the delineation of TMC ligaments. As demonstrated in Chapter 5, differences in predicted joint mechanics arise from inconsistencies in reported ligament configurations across anatomical studies of TMC ligaments. These inconsistencies include differences in the number of ligaments identified and substantial variation in reported dimensions and insertion regions.

Importantly, absence of specific ligaments, such as the dAOL or dIML, in a subset of specimens has been reported (Bettinger et al., 1999), suggesting that inter-individual variability in ligament structure may be a genuine anatomical feature rather than a limitation of individual studies. When considered alongside the pronounced sensitivity to CT-based bone geometry demonstrated in Chapter 5, these findings indicate that anatomical variability at the TMC joint spans both ligament structure and bony morphology, and that these factors jointly determine joint stability and cartilage loading.

From this perspective, the objective of future anatomical research should not be limited to defining a single standardised ligament dataset, but rather to characterising the spectrum of anatomical variability across populations. Differences related to sex,

ethnicity, and population background remain largely unexplored for the TMC joint, despite analogous variability being well recognised in other joints such as the knee (Hosseinzadeh and Kiapour, 2020; Kim et al., 2017).

The modelling framework developed in this thesis is specifically suited to addressing this challenge. Enabling systematic evaluation of joint mechanics across multiple ligament configurations and bone geometries provides a platform for investigating how anatomical variability influences cartilage stress under functional loading. This capability represents a key contribution of the present work and supports future efforts toward population-based and subject-specific assessment of TMC joint mechanics and osteoarthritis risk.

7.2.2. Population CT-based FE Modelling and Machine Learning Surrogate Prediction

Bone geometry strongly influenced cartilage stress predictions and contact mechanics. In addition, sex-related differences in TMC contact area during daily activities have been reported (Schneider et al., 2017). Morphological variability in both the first metacarpal and trapezium has also been demonstrated (Rusli and Kedgley, 2020). Flanagan et al., (2022) further identified multiple shape types of the trapezial articular surface. Therefore, developing a population-based anatomical dataset would improve the generalisability of FE predictions and facilitate clinical translation rather than reliance on a single representative model.

Before large-scale simulation libraries are developed, an important prerequisite is determining the level of model complexity required. As discussed in Chapter 6, the present framework prescribes experimentally measured thumb kinematics and applies externally measured forces but does not include muscle forces. Future work should therefore evaluate, across a range of anatomical geometries, whether incorporating

MSk-modelling derived muscle forces alters cartilage stress predictions for low-force, high-repetition tasks such as smartphone interaction, or whether the current approach provides an adequate and computationally efficient approximation.

Once an appropriate modelling framework is established, future research should focus on collecting a large clinical CT dataset of the trapezium and first metacarpal from individuals with different sex, age, and joint morphologies, enabling generation of multiple individual-based FE models. Once a high-throughput simulation library is established by running consistent loading scenarios such as representative smartphone tasks, lateral pinch, jar-opening postures, the resulting FE outputs, including peak von Mises stress, and stress distribution patterns, can be used to train surrogate machine-learning models that rapidly predict cartilage stress outcomes for any geometry. Deep learning has already been demonstrated as an accurate surrogate capable of predicting full-field stress distributions as a fast alternative to conventional FE computation, providing a clear methodological precedent for stress-map prediction (Frazer et al., 2024; Liang et al., 2018).

Such a framework would enable clinically and ergonomically relevant applications, including rapid patient-specific assessment of joint loading and osteoarthritis susceptibility, evaluation of how individual anatomy interacts with smartphone usage patterns, and optimisation of device design to reduce excessive thumb joint demand. By integrating experimental data, anatomically informed FE modelling, and data-driven surrogates, future work could support both personalised joint health assessment and evidence-based design strategies for safer smartphone use.

7.2.3. Ergonomic improvement for smartphone use

As reviewed in Chapter 2, The TMC joint permits a large range of motion, with reported mean values of approximately 40° for flexion–extension, 50° for abduction–adduction,

and 20° for axial rotation (Barakat et al., 2013; Goubier et al., 2009). In this study, touchscreen interactions associated with larger joint excursions, such as typing at key 7 (abduction-adduction: -54°, flexion-extension: -31°) and leftward swiping (abduction–adduction: 46°, flexion–extension: 47°), involved joint angles toward the upper range of the measured kinematic conditions and were associated with higher predicted cartilage stress compared with more neutral tasks such as typing at key 6.This indicates that interaction locations associated with more extreme joint angles impose greater mechanical demand on the TMC joint.

Informed by these findings, interaction strategy and interface design may influence the mechanical loading of the TMC joint during smartphone use. Previous studies have shown that using a two-handed grip can improve thumb motor performance and alter thumb posture compared with one-handed use, suggesting a more stable and potentially less demanding interaction strategy for the thumb (Trudeau et al., 2016). In addition, a curved keyboard layout has been proposed to improve one-handed usability by placing more keys within the reachable region of the thumb (Wang et al., 2023).

Building on these concepts, future research could develop interface layout that reduce extreme thumb reach, such as adaptive keyboard repositioning frequently used keys towards the lower-central region of the screen. The kinetic-kinematic data collection framework and FE modelling developed in this thesis could be used to quantitatively evaluate the effects of such designs on TMC joint mechanics.

7.2.4. Ergonomic Smartphone Case Design to Reduce Thumb Loading

Similar to ergonomic mouse design, where device geometry supports neutral posture and reduces sustained muscle demand, smartphone hardware could be adapted to promote a more stable and less demanding grip. Future studies could compare features of phone cases, such as edge curvature, thickness, surface friction, and integrated grip

aids (e.g., finger loops, straps, or grip rings), which may reduce stabilisation forces and extreme thumb motions during typing and swiping. These designs could be evaluated across common smartphone tasks using outcomes including user comfort, thumb kinematics and kinetics, and FE-predicted cartilage stress to provide evidence-based guidance for joint-protective, user-friendly smartphone support design.

7.2.5. Prospective study on joint health

Smartphone use is now prevalent across all age groups, with many individuals beginning intensive thumb-based interaction at a young age and continuing over several decades. As a result, current younger users may accumulate a lifetime of exposure to repetitive thumb loading, yet little is known about the long-term implications of this exposure for TMC joint health.

Future research should therefore move beyond laboratory studies to include longitudinal clinical study designs in which individuals are periodically assessed for thumb kinematics, applied forces, and joint health, and followed up across years or decades. By combining repeated experimental measurements with clinical assessments and self-reported smartphone usage patterns, it would be possible to establish correlations between cumulative exposure metrics, such as intensity, frequency, posture, and force, and the development of TMC-joint pathology. Integrating FE modelling into such longitudinal studies would further enable evaluation of whether mechanically derived stress metrics are predictive of long-term joint health outcomes.

7.3. Conclusion

This thesis established an integrated experimental-computational framework to examine how smartphone typing and swiping affect the mechanical response of the

TMC joint. The framework enabled physiologically realistic estimation of articular cartilage stresses during representative smartphone interactions and revealed loading patterns associated with increased joint demand. Overall, the findings provide a robust basis for evaluating TMC joint loading during smartphone use and support the design of smartphone interfaces, usage strategies, and assistive accessories aimed at minimising thumb joint loading and reducing long-term osteoarthritis risk.

References

Acosta-Flores, M., Contreras-Valenzuela, M.R., Velásquez-Aguilar, J.G., Cuenca-Jiménez, F., Eraña-Díaz, M.L., 2024. Triaxial Load Cell for Ergonomic Risk Assessment: A Study Case of Applied Force of Thumb. Appl. Sci. 14, 3981. https://doi.org/10.3390/app14103981

Al-Dhafer, B.A.A., Alessa, H.A., Albesher, M.A., Alnaim, M.F., Albawardi, S.K., Albesher, M., 2023. The Association Between Smartphone Addiction/Overuse With Hand and Wrist Musculoskeletal Complaints, Saudi Arabia. Cureus. https://doi.org/10.7759/cureus.48752

Ancillao, A., Aertbeliën, E., De Schutter, J., 2021. Effect of the soft tissue artifact on marker measurements and on the calculation of the helical axis of the knee during a gait cycle: A study on the CAMS-Knee data set. Hum. Mov. Sci. 80, 102866. https://doi.org/10.1016/j.humov.2021.102866

Anwar, A., Hu, Z., Zhang, Y., Gao, Y., Tian, C., Wang, X., Nazir, M.U., Wang, Y., Zhao, Z., Lv, D., Zhang, Z., Zhang, H., Lv, G., 2020. Multiple Subchondral Bone Cysts Cause Deterioration of Articular Cartilage in Medial OA of Knee: A 3D Simulation Study. Front. Bioeng. Biotechnol. 8, 573938. https://doi.org/10.3389/fbioe.2020.573938

Armstrong, A.L., Hunter, J.B., Davis, T.R.C., 1994. The Prevalence of Degenerative Arthritis of the Base of the Thumb in Post-Menopausal Women. J. Hand Surg. 19, 340–341. https://doi.org/10.1016/0266-7681(94)90085-X

Asakawa, D.S., Crocker, G.H., Schmaltz, A., Jindrich, D.L., 2017. Fingertip forces and completion time for index finger and thumb touchscreen gestures. J. Electromyogr. Kinesiol. 34, 6–13. https://doi.org/10.1016/j.jelekin.2017.02.007

Athar, M., Hashmi, J., Saleem, M.M., Azam, J., Umar, S.A., Mahmmoud Fadelallah Eljack, M., 2025. Impact of excessive phone usage on hand functions and incidence of

hand disorders. Ann. Med. Surg. 87, 1794–1797. https://doi.org/10.1097/ms9.0000000000003143

Austin, E.F., Kearney, C.P., Chacon, P.J., Winges, S.A., Acharya, P., Choi, J.-W., 2022. A Fabricated Force Glove That Measures Hand Forces during Activities of Daily Living. Sensors 22, 1330. https://doi.org/10.3390/s22041330

Autumn, K., Hsieh, S.T., Dudek, D.M., Chen, J., Chitaphan, C., Full, R.J., 2006. Dynamics of geckos running vertically. J. Exp. Biol. 209, 260–272. https://doi.org/10.1242/jeb.01980

Baabdullah, A., Bokhary, D., Kabli, Y., Saggaf, O., Daiwali, M., Hamdi, A., 2020. The association between smartphone addiction and thumb/wrist pain: A cross-sectional study. Medicine (Baltimore) 99, e19124. https://doi.org/10.1097/MD.0000000000019124

Badea, C.T., Drangova, M., Holdsworth, D.W., Johnson, G.A., 2008. In vivo small-animal imaging using micro-CT and digital subtraction angiography. Phys. Med. Biol. 53, R319-350. https://doi.org/10.1088/0031-9155/53/19/R01

Bajuri, M.N., Kadir, M.R.A., Raman, M.M., Kamarul, T., 2012. Mechanical and functional assessment of the wrist affected by rheumatoid arthritis: A finite element analysis. Med. Eng. Phys. 34, 1294–1302. https://doi.org/10.1016/j.medengphy.2011.12.020

Bamberg, S., Benbasat, A.Y., Scarborough, D.M., Krebs, D.E., Paradiso, J.A., 2008. Gait Analysis Using a Shoe-Integrated Wireless Sensor System. IEEE Trans. Inf. Technol. Biomed. 12, 413–423. https://doi.org/10.1109/TITB.2007.899493

Barakat, M.J., Field, J., Taylor, J., 2013. The range of movement of the thumb. Hand N. Y. N 8, 179–182. https://doi.org/10.1007/s11552-013-9492-y

Barry, A.J., Murray, W.M., Kamper, D.G., 2018. Development of a dynamic index

finger and thumb model to study impairment. J. Biomech. 77, 206–210. https://doi.org/10.1016/j.jbiomech.2018.06.017

Bazira, P.J., 2022. Surgical anatomy of the hand. Surg. Oxf. 40, 155–162. https://doi.org/10.1016/j.mpsur.2022.01.001

Benedetti, M., Catani, F., Leardini, A., Pignotti, E., Giannini, S., 1998. Data management in gait analysis for clinical applications. Clin. Biomech. 13, 204–215. https://doi.org/10.1016/S0268-0033(97)00041-7

Bergmann, G., Deuretzbacher, G., Heller, M., Graichen, F., Rohlmann, A., Strauss, J., Duda, G.N., 2001. Hip contact forces and gait patterns from routine activities. J. Biomech. 34, 859–871. https://doi.org/10.1016/S0021-9290(01)00040-9

Berolo, S., Wells, R.P., Amick, B.C., 2011. Musculoskeletal symptoms among mobile hand-held device users and their relationship to device use: A preliminary study in a Canadian university population. Appl. Ergon. 42, 371–378. https://doi.org/10.1016/j.apergo.2010.08.010

Bettinger, P.C., Linscheid, R.L., Berger, R.A., Cooney, W.P., An, K.-N., 1999. An Anatomic Study of the Stabilizing Ligaments of the Trapezium and Trapeziometacarpal Joint. J. Hand Surg. 24, 786–798. https://doi.org/10.1053/jhsu.1999.0786

Bettinger, P.C., Smutz, W.P., Linscheid, R.L., Cooney, W.P., An, K.-N., 2000. Material properties of the trapezial and trapeziometacarpal ligaments. J. Hand Surg. 25, 1085–1095. https://doi.org/10.1053/jhsu.2000.18487

Betzl, J., Kraneburg, U., Megerle, K., 2020. Overuse syndrome of the hand and wrist in musicians: a systematic review. J. Hand Surg. Eur. Vol. 45, 636–642. https://doi.org/10.1177/1753193420912644

Boehm, K.M., Pugh, A., 2009. A New Variant of Wiiitis. J. Emerg. Med. 36, 80. https://doi.org/10.1016/j.jemermed.2007.11.104

Brown, C.P., Nguyen, T.C., Moody, H.R., Crawford, R.W., Oloyede, A., 2009. Assessment of common hyperelastic constitutive equations for describing normal and osteoarthritic articular cartilage. Proc. Inst. Mech. Eng. [H] 223, 643–652. https://doi.org/10.1243/09544119JEIM546

Bruna-Rosso, C., Arnoux, P.-J., Bianco, R.-J., Godio-Raboutet, Y., Fradet, L., Aubin, C.-É., 2016. Finite Element Analysis of Sacroiliac Joint Fixation under Compression Loads. Int. J. Spine Surg. 10, 16. https://doi.org/10.14444/3016

Buckwalter, J.A., Anderson, D.D., Brown, T.D., Tochigi, Y., Martin, J.A., 2013. The Roles of Mechanical Stresses in the Pathogenesis of Osteoarthritis: Implications for Treatment of Joint Injuries. CARTILAGE 4, 286–294. https://doi.org/10.1177/1947603513495889

Camomilla, V., Bonci, T., Dumas, R., Chèze, L., Cappozzo, A., 2015. A model of the soft tissue artefact rigid component. J. Biomech. 48, 1752–1759. https://doi.org/10.1016/j.jbiomech.2015.05.007

Canillas, F., Colino, A., Menéndez, P., 2014. Cellular Phone Overuse as A Cause for Trapeziometacarpal Osteoarthritis: A Two Case Report. J. Orthop. Case Rep. 4, 6–8. https://doi.org/10.13107/jocr.2250-0685.213

Cao, M.Y., Laws, S., Baena, F.R.Y., 2021. Six-Axis Force/Torque Sensors for Robotics Applications: A Review. IEEE Sens. J. 21, 27238–27251. https://doi.org/10.1109/JSEN.2021.3123638

Cappozzo, A., Catani, F., Della Croce, U., Leardini, A., 1995. Position and orientation in space of bones during movement: anatomical frame definition and determination. Clin. Biomech. 10, 171–178. https://doi.org/10.1016/0268-0033(95)91394-T

Cappozzo, A., Catani, F., Leardini, A., Benedetti, M., Della Croce, U., 1996. Position and orientation in space of bones during movement: experimental artefacts. Clin.

Biomech. 11, 90–100. https://doi.org/10.1016/0268-0033(95)00046-1

Carducci, J., Olds, K., Krakauer, J.W., Xu, J., Brown, J.D., 2022. Novel Planar Strain Sensor Design for Capturing 3-Dimensional Fingertip Forces from Patients Affected by Hand Paralysis. Sensors 22, 7441. https://doi.org/10.3390/s22197441

Carrigan, S.D., Whiteside, R.A., Pichora, D.R., Small, C.F., 2003. Development of a Three-Dimensional Finite Element Model for Carpal Load Transmission in a Static Neutral Posture. Ann. Biomed. Eng. 31, 718–725. https://doi.org/10.1114/1.1574027

Choi, M.J., Bustos, V.P., Xu, K.Y., 2025. The Impact of Handheld Device Use on Hand Biomechanics. Bioengineering 12.

Cook, J.R., Baker, N.A., Cham, R., Hale, E., Redfern, M.S., 2007. Measurements of Wrist and Finger Postures: A Comparison of Goniometric and Motion Capture Techniques. J. Appl. Biomech. 23, 70–78.

Cooney, W.P., Chao, E.Y., 1977. Biomechanical analysis of static forces in the thumb during hand function. J. Bone Joint Surg. Am. 59, 27–36.

Cooney, W.P., Lucca, M.J., Chao, E.Y., Linscheid, R.L., 1981. The kinesiology of the thumb trapeziometacarpal joint. J. Bone Joint Surg. Am. 63, 1371–1381.

Crisco, J.J., Morton, A.M., Moore, D.C., Kahan, L.G., Ladd, A.L., Weiss, A.-P.C., 2019. Osteophyte growth in early thumb carpometacarpal osteoarthritis. Osteoarthritis Cartilage 27, 1315–1323. https://doi.org/10.1016/j.joca.2019.05.008

D'Agostino, P., Kerkhof, F.D., Shahabpour, M., Moermans, J.-P., Stockmans, F., Vereecke, E.E., 2014. Comparison of the Anatomical Dimensions and Mechanical Properties of the Dorsoradial and Anterior Oblique Ligaments of the Trapeziometacarpal Joint. J. Hand Surg. 39, 1098–1107. https://doi.org/10.1016/j.jhsa.2014.02.025

Dai, Z., Wang, Z., Ji, A., 2011. Dynamics of gecko locomotion: a force-measuring array to measure 3D reaction forces. J. Exp. Biol. 214, 703–708. https://doi.org/10.1242/jeb.051144

Damm, P., Graichen, F., Rohlmann, A., Bender, A., Bergmann, G., 2010. Total hip joint prosthesis for *in vivo* measurement of forces and moments. Med. Eng. Phys. 32, 95–100. https://doi.org/10.1016/j.medengphy.2009.10.003

D'Lima, D.D., Patil, S., Steklov, N., Slamin, J.E., Colwell, C.W., 2006. Tibial Forces Measured In Vivo After Total Knee Arthroplasty. J. Arthroplasty 21, 255–262. https://doi.org/10.1016/j.arth.2005.07.011

Dong, M., Kerkhof, F., Deleu, G., Vereecke, E., Ladd, A., 2023. Using a finite element model of the thumb to study Trapeziometacarpal joint contact during lateral pinch. Clin. Biomech. 101, 105852. https://doi.org/10.1016/j.clinbiomech.2022.105852

Dzidek, B.M., Adams, M.J., Andrews, J.W., Zhang, Z., Johnson, S.A., 2017. Contact mechanics of the human finger pad under compressive loads. J. R. Soc. Interface 14, 20160935. https://doi.org/10.1098/rsif.2016.0935

Eaton, R.G., Littler, J.W., 1973. Ligament reconstruction for the painful thumb carpometacarpal joint. J. Bone Joint Surg. Am. 55, 1655–1666.

Edmunds, J.O., 2011. Current Concepts of the Anatomy of the Thumb Trapeziometacarpal Joint. J. Hand Surg. 36, 170–182. https://doi.org/10.1016/j.jhsa.2010.10.029

El-shennawy, M., Nakamura, K., Patterson, R.M., Viegas, S.F., 2001. Three-dimensional kinematic analysis of the second through fifth carpometacarpal joints. J. Hand Surg. 26, 1030–1035. https://doi.org/10.1053/jhsu.2001.28761

Eschweiler, J., Horn, N., Rath, B., Betsch, M., Baroncini, A., Tingart, M., Migliorini, F., 2021. The Biomechanics of Cartilage—An Overview. Life 11, 302.

https://doi.org/10.3390/life11040302

Esplugas, M., Lluch-Bergada, A., Mobargha, N., Llusa-Perez, M., Hagert, E., Garcia-Elias, M., 2016. Trapeziometacarpal Ligaments Biomechanical Study: Implications in Arthroscopy. J. Wrist Surg. 5, 277–283. https://doi.org/10.1055/s-0036-1581052

Esrafilian, A., Stenroth, L., Mononen, M.E., Tanska, P., Avela, J., Korhonen, R.K., 2020. EMG-Assisted Muscle Force Driven Finite Element Model of the Knee Joint with Fibril-Reinforced Poroelastic Cartilages and Menisci. Sci. Rep. 10, 3026. https://doi.org/10.1038/s41598-020-59602-2

Fang, H., Shi, R., Xu, J., 2024. Triaxial ground reaction forces of earthworm rectilinear locomotion: measurement, analysis, and implications for robot modeling. Acta Mech. Sin. 40, 223198. https://doi.org/10.1007/s10409-023-23198-x

Fernandez-Guerrero, I.M., 2014. “WhatsAppitis.” The Lancet 383, 1040. https://doi.org/10.1016/S0140-6736(14)60519-5

Flanagan, C.D., Tamer, P., Cooperman, D.R., Crisco, J.J., Ladd, A.L., Liu, R.W., 2022. An Anatomical Evaluation of the Trapezium and Its Relationship to Basilar Joint Osteophytic Change. HAND 17, 714–722. https://doi.org/10.1177/1558944720946490

Frazer, L., Kote, V., Hostetler, Z., Davis, M., Nicolella, D.P., 2024. A comparative analysis of dimensionality reduction surrogate modeling techniques for full human body finite element impact simulations. Comput. Methods Biomech. Biomed. Engin. 27, 1250–1263. https://doi.org/10.1080/10255842.2023.2236747

Fu, L., Łukasz, K., Jiang, C., Gu, Y., 2023. A Region-Based Statistical Shape Modeling on the First Trapezoid-Metacarpal. Appl. Bionics Biomech. 2023, 1–8. https://doi.org/10.1155/2023/3257460

Galbusera, F., Freutel, M., DÃ¼rselen, L., Dâ€™Aiuto, M., Croce, D., Villa, T., Sansone, V., Innocenti, B., 2014. Material Models and Properties in the Finite Element

Analysis of Knee Ligaments: A Literature Review. Front. Bioeng. Biotechnol. 2. https://doi.org/10.3389/fbioe.2014.00054

Gillis, J., Calder, K., Williams, J., 2011. Review of Thumb Carpometacarpal Arthritis Classification, Treatment and Outcomes. Can. J. Plast. Surg. 19, 134–138. https://doi.org/10.1177/229255031101900409

Gislason, M.K., Nash, D.H., Nicol, A., Kanellopoulos, A., Bransby-Zachary, M., Hems, T., Condon, B., Stansfield, B., 2009. A three-dimensional finite element model of maximal grip loading in the human wrist. Proc. Inst. Mech. Eng. [H] 223, 849–861. https://doi.org/10.1243/09544119JEIM527

Gíslason, M.K., Stansfield, B., Nash, D.H., 2010. Finite element model creation and stability considerations of complex biological articulation: The human wrist joint. Med. Eng. Phys. 32, 523–531. https://doi.org/10.1016/j.medengphy.2010.02.015

Gómez, C.L., Gondolbeu, A.M., Martí, R.M., Renart, I.P., Pérez, M.L., 2017. The Role Of The Carpometacarpal Ligaments Of The Thumb In Stability And The Development Of Osteoarthritis Lesions : An Anatomical Study. Acta Orthop. Belg. 83, 449–457.

Goubier, J.-N., Devun, L., Mitton, D., Lavaste, F., Papadogeorgou, E., 2009. Normal range-of-motion of trapeziometacarpal joint. Chir. Main 28, 297–300. https://doi.org/10.1016/j.main.2009.07.003

Gray, H., Standring, S., Anhand, N. (Eds.), 2021. Gray's Anatomy: the anatomical basis of clinical practice, 42nd edition. ed. Elsevier, Amsterdam.

Greiner, T.M., 1991. Hand anthropometry of US army personnel (No. NATICK/TR-92/011). U.S. Army Natick Research, Development & Engineering Center.

Guilak, F., 2011. Biomechanical factors in osteoarthritis. Best Pract. Res. Clin. Rheumatol. 25, 815–823. https://doi.org/10.1016/j.berh.2011.11.013

Guo, X., Fan, Y., Li, Z.-M., 2009. Effects of dividing the transverse carpal ligament on the mechanical behavior of the carpal bones under axial compressive load: A finite element study. Med. Eng. Phys. 31, 188–194. https://doi.org/10.1016/j.medengphy.2008.08.001

Gustafsson, E., Coenen, P., Campbell, A., Straker, L., 2018. Texting with touchscreen and keypad phones - A comparison of thumb kinematics, upper limb muscle activity, exertion, discomfort, and performance. Appl. Ergon. 70, 232–239. https://doi.org/10.1016/j.apergo.2018.03.003

Gustafsson, E., Johnson, P.W., Hagberg, M., 2010. Thumb postures and physical loads during mobile phone use – A comparison of young adults with and without musculoskeletal symptoms. J. Electromyogr. Kinesiol. 20, 127–135. https://doi.org/10.1016/j.jelekin.2008.11.010

Haara, M.M., Heliövaara, M., Kröger, H., Arokoski, J.P.A., Manninen, P., Kärkkäinen, A., Knekt, P., Impivaara, O., Aromaa, A., 2004. Osteoarthritis in the carpometacarpal joint of the thumb: Prevalence and association with disability and mortality. J. Bone Jt. Surg.-Am. Vol. 86, 1452–1457. https://doi.org/10.2106/00004623-200407000-00013

Hair, J.F., Ringle, C.M., Sarstedt, M., 2011. PLS-SEM: Indeed a Silver Bullet. J. Mark. Theory Pract. 19, 139–152. https://doi.org/10.2753/MTP1069-6679190202

Halilaj, E., Moore, D.C., Patel, T.K., Ladd, A.L., Weiss, A.C., Crisco, J.J., 2015. Early osteoarthritis of the trapeziometacarpal joint is not associated with joint instability during typical isometric loading. J. Orthop. Res. 33, 1639–1645. https://doi.org/10.1002/jor.22936

Halilaj, E., Rainbow, M.J., Got, C., Schwartz, J.B., Moore, D.C., Weiss, A.-P.C., Ladd, A.L., Crisco, J.J., 2014. In Vivo Kinematics of the Thumb Carpometacarpal Joint During Three Isometric Functional Tasks. Clin. Orthop. 472, 1114–1122. https://doi.org/10.1007/s11999-013-3063-y

Halilaj, E., Rainbow, M.J., Got, C.J., Moore, D.C., Crisco, J.J., 2013. A thumb carpometacarpal joint coordinate system based on articular surface geometry. J. Biomech. 46, 1031–1034. https://doi.org/10.1016/j.jbiomech.2012.12.002

Hamidrad, S., Abdollahi, M., Badali, V., Nikkhoo, M., Naserkhaki, S., 2021. Biomechanical modeling of spinal ligaments: finite element analysis of L4-L5 spinal segment. Comput. Methods Biomech. Biomed. Engin. 24, 1807–1818. https://doi.org/10.1080/10255842.2021.1919885

Han, G., Hess, C., Eriten, M., Henak, C.R., 2018. Uncoupled poroelastic and intrinsic viscoelastic dissipation in cartilage. J. Mech. Behav. Biomed. Mater. 84, 28–34. https://doi.org/10.1016/j.jmbbm.2018.04.024

Han, Y., Vallerini, F.M., Holdsworth, F., Wanglertpanich, K., Kedgley, A.K., Masouros, S.D., n.d. A custom force plate for quantifying the force applied by the finger during smartphone usage.

Heglund, N.C., 1981. A Simple Design for A Force-Plate to Measure Ground Reaction Forces. J. Exp. Biol. 93, 333–338. https://doi.org/10.1242/jeb.93.1.333

Hosseinzadeh, S., Kiapour, A.M., 2020. Sex Differences in Anatomic Features Linked to Anterior Cruciate Ligament Injuries During Skeletal Growth and Maturation. Am. J. Sports Med. 48, 2205–2212. https://doi.org/10.1177/0363546520931831

Ikumi, A., Kohyama, S., Okuwaki, S., Tatsumura, M., Hara, Y., Mammoto, T., Ogawa, T., Yoshii, Y., Kawamura, H., Yamazaki, M., 2022. Effects of Magnetic Resonance Imaging With Axial Traction of the Thumb Carpometacarpal Joint on Articular Cartilage Visibility: A Feasibility Study. Cureus. https://doi.org/10.7759/cureus.22421

Imaeda, T., An, K.-N., Cooney, W.P., 1992. Functional Anatomy and Biomechanics of the Thumb. Hand Clin. 8, 9–15. https://doi.org/10.1016/S0749-0712(21)00688-0

Imaeda, T., An, K.-N., Cooney, W.P., Linscheid, R., 1993. Anatomy of

trapeziometacarpal ligaments. J. Hand Surg. 18, 226–231. https://doi.org/10.1016/0363-5023(93)90352-4

Imai, K., 2015. Computed tomography-based finite element analysis to assess fracture risk and osteoporosis treatment. World J. Exp. Med. 5, 182–187. https://doi.org/10.5493/wjem.v5.i3.182

Incze-Bartha, Z., Incze-Bartha, S., Simon Szabó, Z., Feier, A.M., Vunvulea, V., Nechifor-Boilă, I.A., Pastorello, Y., Szasz, D., Dénes, L., 2023. Finite Element Analysis of Normal and Dysplastic Hip Joints in Children. J. Pers. Med. 13, 1593. https://doi.org/10.3390/jpm13111593

Jindrich, D.L., Balakrishnan, A.D., Dennerlein, J.T., 2004. Finger joint impedance during tapping on a computer keyswitch. J. Biomech. 37, 1589–1596. https://doi.org/10.1016/j.jbiomech.2004.01.001

Jonsson, P., Johnson, P.W., Hagberg, M., 2007. Accuracy and feasibility of using an electrogoniometer for measuring simple thumb movements. Ergonomics 50, 647–659. https://doi.org/10.1080/00140130601164490

Kaewpradit, K., Ngamchaliew, P., Buathong, N., 2025. Digital screen time usage, prevalence of excessive digital screen time, and its association with mental health, sleep quality, and academic performance among Southern University students. Front. Psychiatry 16, 1535631. https://doi.org/10.3389/fpsyt.2025.1535631

Kanai, A., Kiyama, T., Genda, E., Suzuki, Y., 2008. Biomechanical investigation of ambulatory training in patients with acetabular dysplasia. Gait Posture 28, 52–57. https://doi.org/10.1016/j.gaitpost.2007.09.012

Karakostis, F.A., Haeufle, D., Anastopoulou, I., Moraitis, K., Hotz, G., Tourloukis, V., Harvati, K., 2021. Biomechanics of the human thumb and the evolution of dexterity. Curr. Biol. 31, 1317-1325.e8. https://doi.org/10.1016/j.cub.2020.12.041

Kiapour, A.M., Kaul, V., Kiapour, A., Quatman, C.E., Wordeman, S.C., Hewett, T.E., Demetropoulos, C.K., Goel, V.K., 2013. The Effect of Ligament Modeling Technique on Knee Joint Kinematics: A Finite Element Study. Appl. Math. 04, 91–97. https://doi.org/10.4236/am.2013.45A011

Kim, J.H., Aulck, L., Bartha, M.C., Harper, C.A., Johnson, P.W., 2014. Differences in typing forces, muscle activity, comfort, and typing performance among virtual, notebook, and desktop keyboards. Appl. Ergon. 45, 1406–1413. https://doi.org/10.1016/j.apergo.2014.04.001

Kim, S.H., Kim, Y.H., Lee, C.-H., Lee, Y., 2024. Smartphone usage and overdependence risk among middle-aged and older adults: a cross-sectional study. BMC Public Health 24, 413. https://doi.org/10.1186/s12889-024-17873-8

Kim, T.K., Phillips, M., Bhandari, M., Watson, J., Malhotra, R., 2017. What Differences in Morphologic Features of the Knee Exist Among Patients of Various Races? A Systematic Review. Clin. Orthop. 475, 170–182. https://doi.org/10.1007/s11999-016-5097-4

Kim, W., Kim, Y., Park, H., 2019. In Vivo Measurement of Thumb Joint Reaction Forces During Smartphone Manipulation: A Biomechanical Analysis. J. Orthop. Res. 37, 2437–2444. https://doi.org/10.1002/jor.24405

Kjartan, M., H., D., 2012. Finite Element Modelling of a Multi-Bone Joint: The Human Wrist, in: Ebrahimi, F. (Ed.), Finite Element Analysis - New Trends and Developments. InTech. https://doi.org/10.5772/50560

Kobsar, D., Charlton, J.M., Tse, C.T.F., Esculier, J.-F., Graffos, A., Krowchuk, N.M., Thatcher, D., Hunt, M.A., 2020. Validity and reliability of wearable inertial sensors in healthy adult walking: a systematic review and meta-analysis. J. NeuroEngineering Rehabil. 17, 62. https://doi.org/10.1186/s12984-020-00685-3

Krakowski, P., Rejniak, A., Sobczyk, J., Karpiński, R., 2024. Cartilage Integrity: A Review of Mechanical and Frictional Properties and Repair Approaches in Osteoarthritis. Healthcare 12, 1648. https://doi.org/10.3390/healthcare12161648

Kumban, W., Cetthakrikul, S., Santiworakul, A., 2025. Smartphone Addiction, Screen Time, and Physical Activity of Different Academic Majors and Study Levels in University Students. Int. J. Environ. Res. Public. Health 22, 237. https://doi.org/10.3390/ijerph22020237

Kuo, L.-C., Cooney, W.P., Oyama, M., Kaufman, K.R., Su, F.-C., An, K.-N., 2003. Feasibility of using surface markers for assessing motion of the thumb trapeziometacarpal joint. Clin. Biomech. 18, 558–563. https://doi.org/10.1016/S0268-0033(03)00074-3

Kurosawa, A., Higuchi, M., Tachiya, H., Tada, K., Murai, A., Tamai, A., Kawashima, H., 2024. Finite element analysis to clarify stress on articular surface of thumb carpometacarpal joint in static loading conditions by using CT images. J. Biomech. Sci. Eng. 19, 23-00296-23–00296. https://doi.org/10.1299/jbse.23-00296

Ladd, A.L., Lee, J., Hagert, E., 2012. Macroscopic and microscopic analysis of the thumb carpometacarpal ligaments: a cadaveric study of ligament anatomy and histology. J. Bone Joint Surg. Am. 94, 1468–1477. https://doi.org/10.2106/JBJS.K.00329

Ladd, A.L., Weiss, A.-P.C., Crisco, J.J., Hagert, E., Wolf, J.M., Glickel, S.Z., Yao, J., 2013. The thumb carpometacarpal joint: anatomy, hormones, and biomechanics. Instr. Course Lect. 62, 165–179.

Lampen, N., Su, H., Chan, D.D., Yan, P., 2021. T_2 Mapping Refined Finite Element Modeling to Predict Knee Osteoarthritis Progression, in: 2021 43rd Annual International Conference of the IEEE Engineering in Medicine & Biology Society (EMBC). Presented at the 2021 43rd Annual International Conference of the IEEE Engineering in Medicine & Biology Society (EMBC), IEEE, Mexico, pp. 4592–4595.

https://doi.org/10.1109/EMBC46164.2021.9629780

Leardini, A., Chiari, L., Croce, U.D., Cappozzo, A., 2005. Human movement analysis using stereophotogrammetry. Gait Posture 21, 212–225. https://doi.org/10.1016/j.gaitpost.2004.05.002

Lee, Songil, Kyung, G., Yi, J., Choi, D., Park, S., Choi, B., Lee, Seungbae, 2019. Determining Ergonomic Smartphone Forms With High Grip Comfort and Attractive Design. Hum. Factors J. Hum. Factors Ergon. Soc. 61, 90–104. https://doi.org/10.1177/0018720818792758

Lewis, C., Jackson, J.A., Stjernbrandt, A., Andersson, G., Mukka, S., Wahlström, J., Liv, P., 2025. Occupational risk factors for thumb carpometacarpal joint osteoarthritis: a register-based study of construction workers. Occup. Environ. Med. 82, 14–20. https://doi.org/10.1136/oemed-2024-109949

Liang, L., Liu, M., Martin, C., Sun, W., 2018. A deep learning approach to estimate stress distribution: a fast and accurate surrogate of finite-element analysis. J. R. Soc. Interface 15, 20170844. https://doi.org/10.1098/rsif.2017.0844

Lin, J.D., Karl, J.W., Strauch, R.J., 2014. Trapeziometacarpal joint stability: the evolving importance of the dorsal ligaments. Clin. Orthop. 472, 1138–1145. https://doi.org/10.1007/s11999-013-2879-9

Logozzo, S., Valigi, M.C., Malvezzi, M., 2022. Modelling the human touch: A basic study for haptic technology. Tribol. Int. 166, 107352. https://doi.org/10.1016/j.triboint.2021.107352

Lou, C., Xiang, G., Weng, Q., Chen, Z., Chen, D., Wang, Q., Zhang, D., Zhou, B., He, D., Chen, H., 2016. Menopause is associated with articular cartilage degeneration: a clinical study of knee joint in 860 women. Menopause 23, 1239–1246. https://doi.org/10.1097/GME.0000000000000697

Lung, B.E., Burns, B., 2026. Anatomy, Shoulder and Upper Limb, Hand Flexor Digitorum Profundus Muscle, in: StatPearls. StatPearls Publishing, Treasure Island (FL).

Marqués, R., Melchor, J., Sánchez-Montesinos, I., Roda, O., Rus, G., Hernández-Cortés, P., 2022. Biomechanical Finite Element Method Model of the Proximal Carpal Row and Experimental Validation. Front. Physiol. 12, 749372. https://doi.org/10.3389/fphys.2021.749372

McCann, M.R., Rust, P.A., Wallace, R., 2018. The Stabilising Effect of the Anterior Oblique Ligament to Prevent Directional Subluxation at the Trapeziometacarpal Joint of the Thumb: A Biomechanical Cadaveric Study. Arch. Bone Jt. Surg. 6, 105–111.

McFarland, D.C., Binder-Markey, B.I., Nichols, J.A., Wohlman, S.J., De Bruin, M., Murray, W.M., 2023. A Musculoskeletal Model of the Hand and Wrist Capable of Simulating Functional Tasks. IEEE Trans. Biomed. Eng. 70, 1424–1435. https://doi.org/10.1109/TBME.2022.3217722

Mellors, B., Allen, P., Lavecchia, C.E., Mountcastle, S., Cooke, M.E., Lawless, B.M., Cox, S.C., Jones, S., Espino, D.M., 2023. Development and experimental validation of a dynamic numerical model for human articular cartilage. Proc. Inst. Mech. Eng. [H] 237, 879–889. https://doi.org/10.1177/09544119231180901

Metcalf, C.D., Phillips, C., Forrester, A., Glodowski, J., Simpson, K., Everitt, C., Darekar, A., King, L., Warwick, D., Dickinson, A.S., 2020. Quantifying Soft Tissue Artefacts and Imaging Variability in Motion Capture of the Fingers. Ann. Biomed. Eng. 48, 1551–1561. https://doi.org/10.1007/s10439-020-02476-2

Muybridge, E., 1887. Animal locomotion. Capo Press Oxf. 534.

Nagano, A., Noritake, H., Luo, Z.-W., 2010. An analysis of directional changes in the center of pressure trajectory during stance. Gait Posture 31, 400–402.

https://doi.org/10.1016/j.gaitpost.2010.01.007

Nanno, M., Buford, W.L., Patterson, R.M., Andersen, C.R., Viegas, S.F., 2006. Three-Dimensional Analysis of the Ligamentous Attachments of the First Carpometacarpal Joint. J. Hand Surg. 31, 1160–1170. https://doi.org/10.1016/j.jhsa.2006.05.007

Neumann, D.A., Bielefeld, T., 2003. The Carpometacarpal Joint of the Thumb: Stability, Deformity, and Therapeutic Intervention. J. Orthop. Sports Phys. Ther. 33, 386–399. https://doi.org/10.2519/jospt.2003.33.7.386

Nowalk, M.D., Logan, S.E., 1991. Distinguishing Biomechanical Properties of Intrinsic and Extrinsic Human Wrist Ligaments. J. Biomech. Eng. 113, 85–93. https://doi.org/10.1115/1.2894089

Odella, S., 2018. Anatomy of the Trapeziometacarpal Joint, in: Trapeziometacarpal Joint Osteoarthritis. Springer International Publishing, Cham, pp. 1–8. https://doi.org/10.1007/978-3-319-44336-2_1

Olson, J.A., Sandra, D.A., Colucci, É.S., Al Bikaii, A., Chmoulevitch, D., Nahas, J., Raz, A., Veissière, S.P.L., 2022. Smartphone addiction is increasing across the world: A meta-analysis of 24 countries. Comput. Hum. Behav. 129, 107138. https://doi.org/10.1016/j.chb.2021.107138

Palmer, K.T., 2003. Pain in the forearm, wrist and hand. Best Pract. Res. Clin. Rheumatol. 17, 113–135. https://doi.org/10.1016/S1521-6942(02)00100-6

Parmar, S., Khodasevych, I., Troynikov, O., 2017. Evaluation of Flexible Force Sensors for Pressure Monitoring in Treatment of Chronic Venous Disorders. Sensors 17, 1923. https://doi.org/10.3390/s17081923

Paul Smutz, W., Kongsayreepong, A., Hughes, R.E., Niebur, G., Cooney, W.P., An, K.-N., 1998. Mechanical advantage of the thumb muscles. J. Biomech. 31, 565–570. https://doi.org/10.1016/S0021-9290(98)00043-8

Pellegrini, Vincent D., 2001. Pathomechanics of the thumb trapeziometacarpal joint. Hand Clin. 17, 175–184. https://doi.org/10.1016/S0749-0712(21)00238-9

Pellegrini, V. D., 2001. Pathomechanics of the thumb trapeziometacarpal joint. Hand Clin. 17, 175–184, vii–viii.

Pellegrini, V.D., 1991. Osteoarthritis of the trapeziometacarpal joint: The pathophysiology of articular cartilage degeneration. I. Anatomy and pathology of the aging joint. J. Hand Surg. 16, 967–974. https://doi.org/10.1016/S0363-5023(10)80054-1

Peng, Y., Du, X., Huang, L., Li, J., Zhan, R., Wang, W., Xu, B., Wu, S., Peng, C., Chen, S., 2018. Optimizing bone cement stiffness for vertebroplasty through biomechanical effects analysis based on patient-specific three-dimensional finite element modeling. Med. Biol. Eng. Comput. 56, 2137–2150. https://doi.org/10.1007/s11517-018-1844-x

Pérez Ubeda, R., Gutiérrez Rubert, S.C., Zotovic Stanisic, R., Perles Ivars, Á., 2018. Design and Manufacturing of an Ultra-Low-Cost Custom Torque Sensor for Robotics. Sensors 18, 1786. https://doi.org/10.3390/s18061786

Pew Research Center, 2024. Mobile Fact Sheet. Pew Research Center.

Pew Research Center, 2014. Older Adults and Technology Use. Pew Research Center.

Popplewell, H., Carré, M., Lewis, R., 2017. Measurement of finger pad forces and friction using finger nail mounted strain gauges. Wear 376–377, 295–304. https://doi.org/10.1016/j.wear.2016.11.010

Punnett, L., Wegman, D.H., 2004. Work-related musculoskeletal disorders: the epidemiologic evidence and the debate. J. Electromyogr. Kinesiol. 14, 13–23. https://doi.org/10.1016/j.jelekin.2003.09.015

Rath, S., 2011. Hand kinematics: Application in clinical practice. Indian J. Plast. Surg.

Off. Publ. Assoc. Plast. Surg. India 44, 178–185. https://doi.org/10.4103/0970-0358.85338

Reinhardt, L., Blickhan, R., 2013. Ultra miniature force plate for measuring triaxial forces in the micro newton range. J. Exp. Biol. jeb.094177. https://doi.org/10.1242/jeb.094177

Robi, K., Jakob, N., Matevz, K., Matjaz, V., 2013. The Physiology of Sports Injuries and Repair Processes, in: Hamlin, M. (Ed.), Current Issues in Sports and Exercise Medicine. InTech. https://doi.org/10.5772/54234

Roman-Blas, J.A., Castañeda, S., Largo, R., Herrero-Beaumont, G., 2009. Osteoarthritis associated with estrogen deficiency. Arthritis Res. Ther. 11, 241. https://doi.org/10.1186/ar2791

Rostamzadeh, S., Saremi, M., Vosoughi, S., Bradtmiller, B., Janani, L., Farshad, A.A., Taheri, F., 2021. Analysis of hand-forearm anthropometric components in assessing handgrip and pinch strengths of school-aged children and adolescents: a partial least squares (PLS) approach. BMC Pediatr. 21, 39. https://doi.org/10.1186/s12887-020-02468-0

Rusli, W.M.R., Kedgley, A.E., 2020. Statistical shape modelling of the first carpometacarpal joint reveals high variation in morphology. Biomech. Model. Mechanobiol. 19, 1203–1210. https://doi.org/10.1007/s10237-019-01257-8

Rusli, W.M.R., Mirza, E., Tolerton, S., Yong, S., Johnson, R., Horwitz, M.D., Kedgley, A.E., 2021. Ligamentous constraint of the first carpometacarpal joint. J. Biomech. 128, 110789. https://doi.org/10.1016/j.jbiomech.2021.110789

Sakuma, A., Matsuura, Y., Ohtori, S., 2025. Finite element analysis: study of better osteotomy angle of the first metacarpal for thumb carpometacarpal osteoarthritis. Comput. Methods Biomech. Biomed. Engin. 1–9.

https://doi.org/10.1080/10255842.2025.2566247

Sampath, A., Kulkarni, A., G, R., Patel, M., Rathinam, B.A., 2022. Assessment of the Effect of Smartphone Usage on the Range of Motion and Fatigability of the Joints and Muscles of the Thumb Among Users: A Cross-Sectional Study in Central India. Cureus. https://doi.org/10.7759/cureus.23199

Santos, C.C., Marinho, D.A., Costa, M.J., 2022. Reliability of using a pressure sensor system to measure in-water force in young competitive swimmers. Front. Bioeng. Biotechnol. 10, 903753. https://doi.org/10.3389/fbioe.2022.903753

Satapure, P.S., Rajurkar, A.M., Kottawar, V.G., 2017. Automatic articular cartilage segmentation with multiple models, in: 2017 1st International Conference on Intelligent Systems and Information Management (ICISIM). Presented at the 2017 1st International Conference on Intelligent Systems and Information Management (ICISIM), IEEE, Aurangabad, India, pp. 30–37. https://doi.org/10.1109/ICISIM.2017.8122143

Schneider, M.T.Y., Zhang, J., Crisco, J.J., Weiss, A.-P.C., Ladd, A.L., Mithraratne, K., Nielsen, P., Besier, T., 2017. Trapeziometacarpal joint contact varies between men and women during three isometric functional tasks. Med. Eng. Phys. 50, 43–49. https://doi.org/10.1016/j.medengphy.2017.09.002

Schrand, D., 2007. Cross-Talk Compensation Using Matrix Methods. Sens. Transducers J. 79, 1157–1163.

Seesaard, T., Wongchoosuk, C., 2023. Flexible and Stretchable Pressure Sensors: From Basic Principles to State-of-the-Art Applications. Micromachines 14, 1638. https://doi.org/10.3390/mi14081638

Sengupta, D., Kamat, A.M., Smit, Q., Jayawardhana, B., Kottapalli, A.G.P., 2022. Piezoresistive 3D graphene–PDMS spongy pressure sensors for IoT enabled wearables

and smart products. Flex. Print. Electron. 7, 015004. https://doi.org/10.1088/2058-8585/ac4d0e

Shi, Q., Hashizume, H., Inoue, H., Miyake, T., Nagayama, N., 1995. Finite element analysis of pathogenesis of osteoarthritis in the first carpometacarpal joint. https://doi.org/10.18926/AMO/30414

Soltani, Z., Xu, M., Radovitzky, R., Stadelmann, M.A., Hackney, D., Alkalay, R.N., 2024. CT-based finite element simulating spatial bone damage accumulation predicts metastatic human vertebrae strength and stiffness. Front. Bioeng. Biotechnol. 12, 1424553. https://doi.org/10.3389/fbioe.2024.1424553

Sophia Fox, A.J., Bedi, A., Rodeo, S.A., 2009. The Basic Science of Articular Cartilage: Structure, Composition, and Function. Sports Health Multidiscip. Approach 1, 461–468. https://doi.org/10.1177/1941738109350438

Strack, D., Rayudu, N.M., Kirschke, J.S., Baum, T., Subburaj, K., 2024. Reduction of material groups for vertebral bone finite element simulation: cross comparison of grouping methods. Comput. Methods Biomech. Biomed. Engin. 1–11. https://doi.org/10.1080/10255842.2024.2422901

Strauch, R.J., Behrman, M.J., Rosenwasser, M.P., 1994. Acute dislocation of the carpometacarpal joint of the thumb: An anatomic and cadaver study. J. Hand Surg. 19, 93–98. https://doi.org/10.1016/0363-5023(94)90229-1

Synek, A., Settles, M., Stillfried, G., 2012. Multi-body simulation of a human thumb joint by sliding surfaces, in: 2012 4th IEEE RAS & EMBS International Conference on Biomedical Robotics and Biomechatronics (BioRob). Presented at the 2012 4th IEEE RAS & EMBS International Conference on Biomedical Robotics and Biomechatronics (BioRob 2012), IEEE, Rome, Italy, pp. 379–384. https://doi.org/10.1109/BioRob.2012.6290755

Toft, R., Berme, N., 1980. A biomechanical analysis of the joints of the thumb. J. Biomech. 13, 353–360. https://doi.org/10.1016/0021-9290(80)90015-9

Trudeau, M.B., Asakawa, D.S., Jindrich, D.L., Dennerlein, J.T., 2016. Two-handed grip on a mobile phone affords greater thumb motor performance, decreased variability, and a more extended thumb posture than a one-handed grip. Appl. Ergon. 52, 24–28. https://doi.org/10.1016/j.apergo.2015.06.025

Valerio, T., Milan, J.-L., Goislard De Monsabert, B., Vigouroux, L., 2024. The effect of trapeziometacarpal joint passive stiffness on mechanical loadings of cartilages. J. Biomech. 166, 112042. https://doi.org/10.1016/j.jbiomech.2024.112042

Valerio, T., Vigouroux, L., Goislard De Monsabert, B., De Villeneuve Bargemon, J.-B., Milan, J.-L., 2023. Relationship between trapeziometacarpal joint morphological parameters and joint contact pressure: a possible factor of osteoarthritis development. J. Biomech. 152, 111573. https://doi.org/10.1016/j.jbiomech.2023.111573

Venne, G., Tse, M.Y., Pang, S.C., Ellis, R.E., 2020. Mechanically-induced osteophyte in the rat knee. Osteoarthritis Cartilage 28, 853–864. https://doi.org/10.1016/j.joca.2020.02.834

Volz, R.G., Lieb, M., Benjamin, J., 1980. Biomechanics of the wrist. Clin. Orthop. 112–117.

Von Schroeder, H.P., Botte, M.J., 1997. FUNCTIONAL ANATOMY OF THE EXTENSOR TENDONS OF THE DIGITS. Hand Clin. 13, 51–62. https://doi.org/10.1016/S0749-0712(21)00080-9

Wadsworth, C.T., 1983. Clinical Anatomy and Mechanics of the Wrist and Hand. J. Orthop. Sports Phys. Ther. 4, 206–216. https://doi.org/10.2519/jospt.1983.4.4.206

Walker, L., Gordon, D., Chiaramonti, A., Wang, S., Meng, Z., Daley, D., Slate, E., Yao, H., Pellegrini, V.D., Wu, Y., 2025. Morphological and Mechanical Property Differences

in Trapeziometacarpal Ligaments of Healthy and Osteoarthritic Female Joints. Ann. Biomed. Eng. 53, 799–811. https://doi.org/10.1007/s10439-024-03660-4

Wang, M., Zhang, X., Tang, W., Wang, J., 2019. A Structure for Accurately Determining the Mass and Center of Gravity of Rigid Bodies. Appl. Sci. 9, 2532. https://doi.org/10.3390/app9122532

Wang, Y., Huo, J., Wu, D., Lin, T., Li, X., He, J., 2023. Usability of curved keyboard design on the large smartphone: An empirical study. Appl. Ergon. 113, 104013. https://doi.org/10.1016/j.apergo.2023.104013

Ward, L.D., Ambrose, C.G., Masson, M.V., Levaro, F., 2000. The role of the distal radioulnar ligaments, interosseous membrane, and joint capsule in distal radioulnar joint stability. J. Hand Surg. 25, 341–351. https://doi.org/10.1053/jhsu.2000.jhsu25a0341

Wei, Y., Zou, Z., Wei, G., Ren, L., Qian, Z., 2020. Subject-Specific Finite Element Modelling of the Human Hand Complex: Muscle-Driven Simulations and Experimental Validation. Ann. Biomed. Eng. 48, 1181–1195. https://doi.org/10.1007/s10439-019-02439-2

Weizel, A., Distler, T., Detsch, R., Boccaccini, A.R., Bräuer, L., Paulsen, F., Seitz, H., Budday, S., 2022. Hyperelastic parameter identification of human articular cartilage and substitute materials. J. Mech. Behav. Biomed. Mater. 133, 105292. https://doi.org/10.1016/j.jmbbm.2022.105292

Willing, R.T., Lalone, E.A., Shannon, H., Johnson, J.A., King, G.J.W., 2013. Validation of a finite element model of the human elbow for determining cartilage contact mechanics. J. Biomech. 46, 1767–1771. https://doi.org/10.1016/j.jbiomech.2013.04.001

Wolf, J.M., Turkiewicz, A., Atroshi, I., Englund, M., 2020. Occupational load as a risk

factor for clinically relevant base of thumb osteoarthritis. Occup. Environ. Med. 77, 168–171. https://doi.org/10.1136/oemed-2019-106184

Wu, G., van der Helm, F.C.T., (DirkJan) Veeger, H.E.J., Makhsous, M., Van Roy, P., Anglin, C., Nagels, J., Karduna, A.R., McQuade, K., Wang, X., Werner, F.W., Buchholz, B., 2005. ISB recommendation on definitions of joint coordinate systems of various joints for the reporting of human joint motion—Part II: shoulder, elbow, wrist and hand. J. Biomech. 38, 981–992. https://doi.org/10.1016/j.jbiomech.2004.05.042

Xiong, J., Muraki, S., 2014. An ergonomics study of thumb movements on smartphone touch screen. Ergonomics 57, 943–955. https://doi.org/10.1080/00140139.2014.904007

Yang, G., Partridge, K.A., Abdel-Mohti, A., McMullen, A.J., Shen, H., 2016. Finite Element Analysis of Osteotomy Treatment for Kienbock's Disease. J. Biomed. Sci. Eng. 09, 161–170. https://doi.org/10.4236/jbise.2016.910B021

Zaharie, D.T., Phillips, A.T.M., 2018. Pelvic Construct Prediction of Trabecular and Cortical Bone Structural Architecture. J. Biomech. Eng. 140, 091001. https://doi.org/10.1115/1.4039894

Zhang, A., Van Nortwick, S., Hagert, E., Ladd, A., 2013. Thumb Carpometacarpal Ligaments Inside and Out: A Comparative Study of Arthroscopic and Gross Anatomy from the Robert A. Chase Hand and Upper Limb Center at Stanford University. J. Wrist Surg. 02, 055–062. https://doi.org/10.1055/s-0033-1333683

Appendices

A.1 Electrical Circuit Design of the Strain Gauge

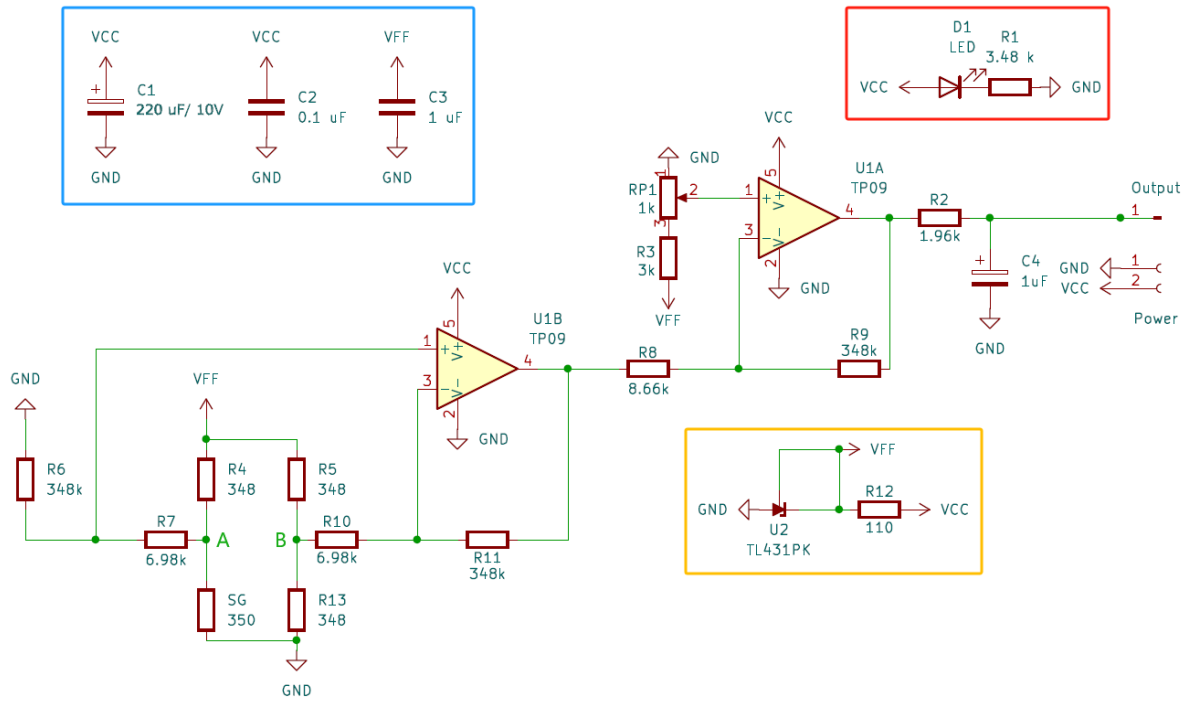


Figure A.1 circuit of strain gauge

Capacitors in parallel to generate stable power supply VCC and VFF

Generate V_{FF} from V_{cc}

$$V_{FF} = V_{cc} - I_{cc}R_{12}$$

V_{cc} and I_{cc} can be read from the power supply.

LED indicating if the circuit is powered

Main circuit:

$$V_{U1B,in,1} = V_A \frac{R_6}{R_6 + R_7} = V_{U1B,in,3}$$

Calculate the current going through R_{10}

$$I_{10} = \frac{V_B - V_{U1B,in,3}}{R_{10}} = \frac{V_B - V_A \frac{R_6}{R_6 + R_7}}{R_{10}}$$

Calculate the voltage drop of R_{11}, and $I_{10} = I_{11}$

$$\Delta V_{11} = I_{10} R_{11} = (V_B - V_A \frac{R_6}{R_6 + R_7}) \frac{R_{11}}{R_{10}}$$

$$V_{U1B,out,4} = V_{U1B,in,3} - \Delta V_{11} = V_A \frac{R_6}{R_6 + R_7} - \left(V_B - V_A \frac{R_6}{R_6 + R_7}\right) \frac{R_{11}}{R_{10}}$$

$$R_6 = R_{11};\ R_7 = R_{10}$$

$$V_A \frac{R_6}{R_6 + R_7} - \left(V_B - V_A \frac{R_6}{R_6 + R_7}\right) \frac{R_{11}}{R_{10}} = V_A \frac{R_6}{R_6 + R_7} - \left(V_B - V_A \frac{R_6}{R_6 + R_7}\right) \frac{R_6}{R_7}$$

$$V_A \frac{R_6}{R_6 + R_7} - \left(V_B - V_A \frac{R_6}{R_6 + R_7}\right) \frac{R_6}{R_7} = \frac{V_A R_6 R_7 - V_B R_6 (R_6 + R_7) + V_A {R_6}^2}{(R_6 + R_7) R_7}$$

$$\frac{V_A R_6 R_7 - V_B R_6 (R_6 + R_7) + V_A {R_6}^2}{(R_6 + R_7) R_7} = \frac{V_A R_6 (R_6 + R_7) - V_B R_6 (R_6 + R_7)}{(R_6 + R_7) R_7}$$

$$\frac{V_A R_6 (R_6 + R_7) - V_B R_6 (R_6 + R_7)}{(R_6 + R_7) R_7} = \frac{(V_A - V_B) R_6 (R_6 + R_7)}{(R_6 + R_7) R_7} = \frac{(V_A - V_B) R_6}{R_7}$$

$(V_A - V_B)$ is the voltage difference caused by strain gauge deformation.

$$Gain\ = \frac{R_6}{R_7} = \frac{348}{6.98} \approx 50$$

Look at U1A

$$V_{U1A,in,1} = \frac{RP_1}{3k + 1k - RP_1} V_{FF} = \frac{RP_1}{4k - RP_1} V_{FF} = V_{U1A,in,3}$$

$$I_8 = \frac{V_{U1B,out,4} - V_{U1A,in,3}}{R_8}$$

$$V_{U1A,out,4} = V_{U1A,in,3} - I_8 R_9 = \frac{RP_1}{4k - RP_1} V_{FF} - \frac{\frac{(V_A - V_B)R_6}{R_7} - \frac{RP_1}{4k - RP_1} V_{FF}}{R_8} R_9$$

Set $\frac{RP_1}{4k - RP_1}$ a constant n

$$V_{U1A,out,4} = nV_{FF} - \frac{\frac{(V_A - V_B)R_6}{R_7} - nV_{FF}}{R_8} R_9 = \left(1 + \frac{R_9}{R_8}\right) nV_{FF} - \frac{R_9}{R_8}\frac{R_6}{R_7}(V_A - V_B)$$

$$\Delta V = (V_A - V_B) = \left(\left(1 + \frac{R_9}{R_8}\right) nV_{FF} - V_{U1A,out,4}\right) \frac{R_8 R_7}{R_9 R_6} = \frac{(41nV_{FF} - V_{U1A,out,4})}{2000}$$

The difference was further amplified through U1A, resulting in the total gain being the product of the gains of both amplifiers.

$$Total\ gain\ = \frac{R_9}{R_8}\frac{R_6}{R_7} \approx 2000$$

Gauge factor: $\frac{\Delta R}{R} / \varepsilon = 2.11$

$$\Delta R_{SG} = 2.11 \varepsilon R_{SG,0}$$

$$R_{SG} = 2.11 \varepsilon R_{SG,0} + R_{SG,0} = 350(2.11\varepsilon + 1)$$

$$V_A = \frac{R_{SG}}{R_{SG} + R_4} V_{FF}$$

$$V_B = \frac{R_{13}}{R_{13} + R_5} V_{FF} = 0.5 V_{FF}$$

$$V_A - V_B = \left(\frac{R_{SG}}{R_{SG} + R_4} - 0.5\right) V_{FF} = \left(\frac{350(2.11\varepsilon + 1)}{350(2.11\varepsilon + 1) + 348} - 0.5\right) V_{FF}$$

$$\frac{V_A - V_B}{V_{FF}} + 0.5 = 1 - \frac{348}{350(2.11\varepsilon + 1) + 348}$$

$$\frac{348}{350(2.11\varepsilon + 1) + 348} = 0.5 - \frac{V_A - V_B}{V_{FF}}$$

$$\frac{348}{350(2.11\varepsilon+1)+348} = \frac{V_{FF}-2(V_A-V_{B)}}{2V_{FF}}$$

$$\frac{348}{350(2.11\varepsilon+1)+348} = \frac{V_{FF}-2(V_A-V_{B)}}{2V_{FF}}$$

$348 \approx 350$

$$2.11\varepsilon+2 = \frac{2V_{FF}}{V_{FF}-2(V_A-V_B)}$$

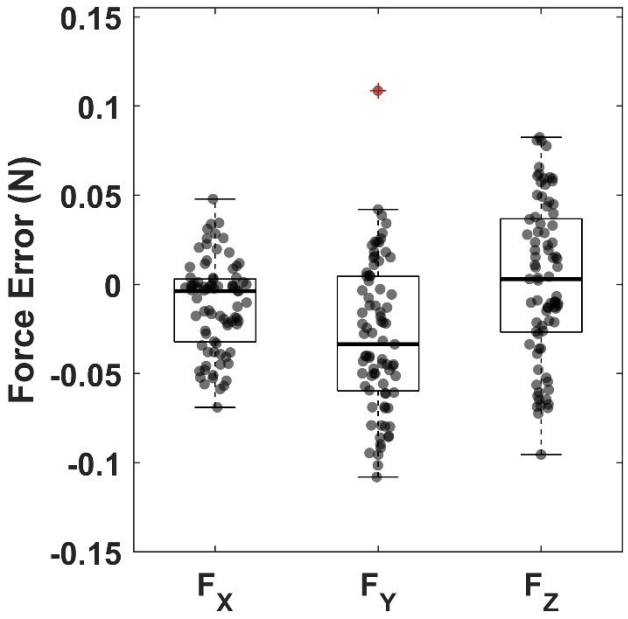
$$2.11\varepsilon = \frac{2V_{FF}}{V_{FF}-2(V_A-V_B)} - \frac{2V_{FF}-4(V_A-V_B)}{V_{FF}-2(V_A-V_B)} = \frac{4(V_A-V_B)}{V_{FF}-2(V_A-V_B)}$$

$$\varepsilon = \frac{1.9\Delta V}{V_{FF}-2\Delta V} = \frac{1.9\Delta V-0.95V_{FF}+0.95V_{FF}}{V_{FF}-2\Delta V} = \frac{0.95V_{FF}}{V_{FF}-2\Delta V} - 0.95$$

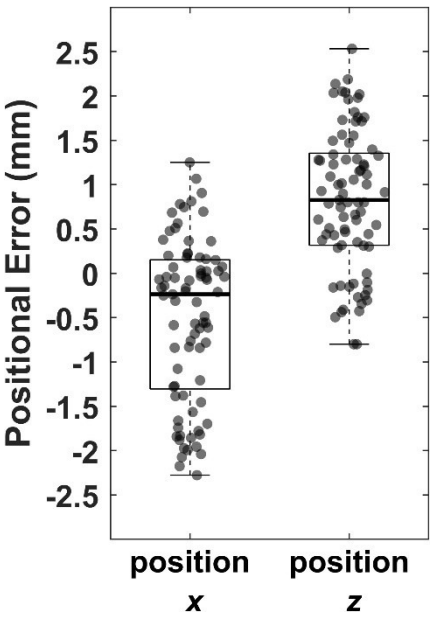
Since $\Delta V = \frac{(41nV_{FF}-V_{U1A,out,4})}{2000}$

$$\varepsilon = \frac{0.95V_{FF}}{V_{FF}-\frac{(41nV_{FF}-V_{U1A,out,4})}{1000}} - 0.95$$

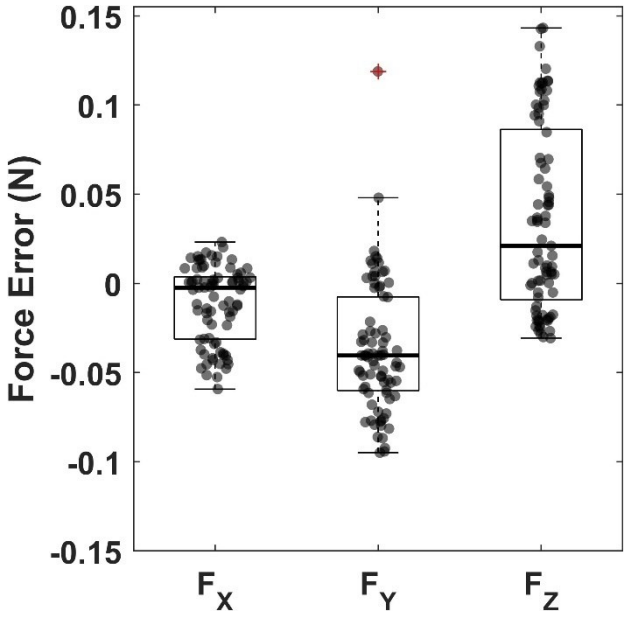
A.2 Error of selected strain gauge combinations



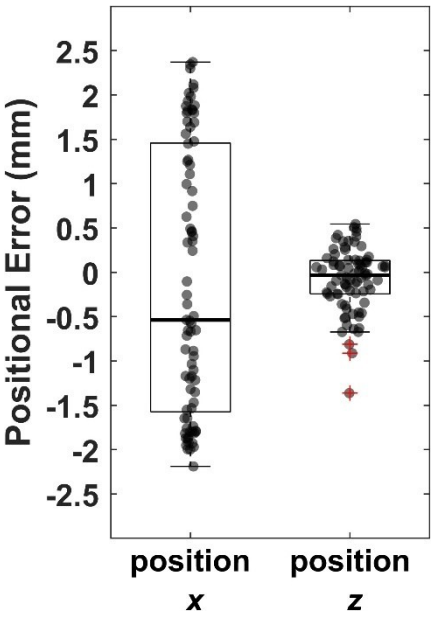
(a)



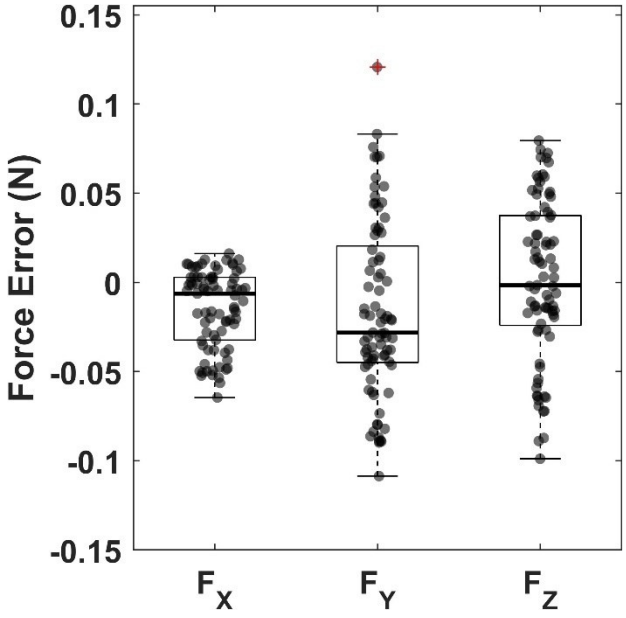
(b)



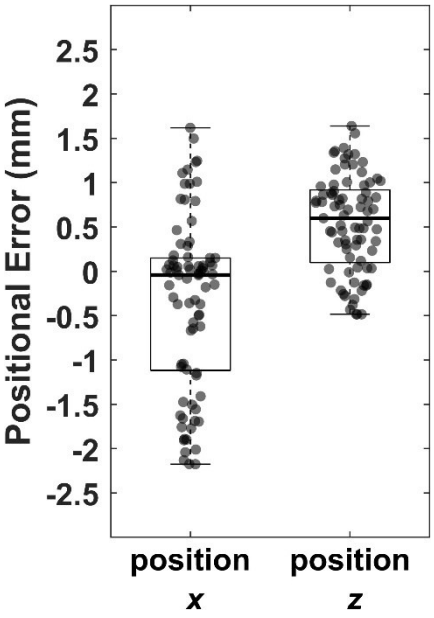
(c)



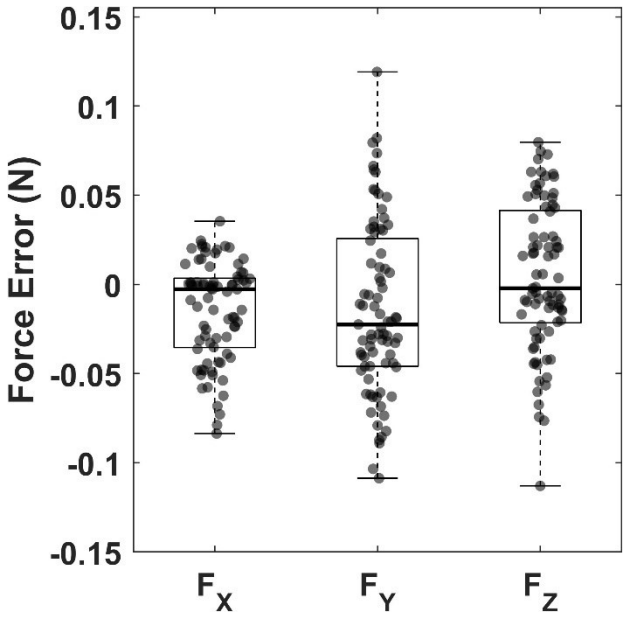
(d)


Force Error (N)
0.15
0.1
0.05
0
-0.05
-0.1
-0.15
F_X
F_Y
F_Z

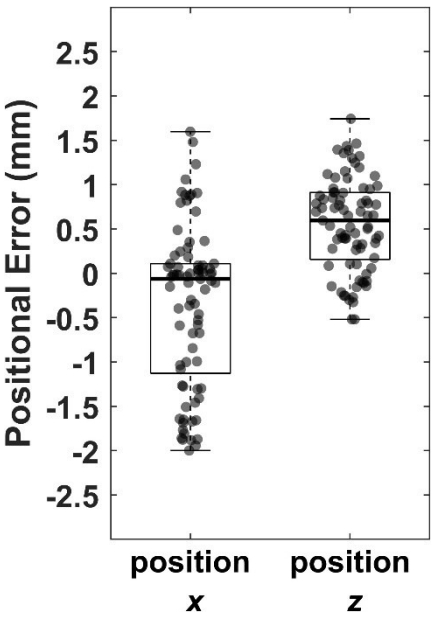
(e)


Positional Error (mm)
2.5
2
1.5
1
0.5
0
-0.5
-1
-1.5
-2
-2.5
position x
position z

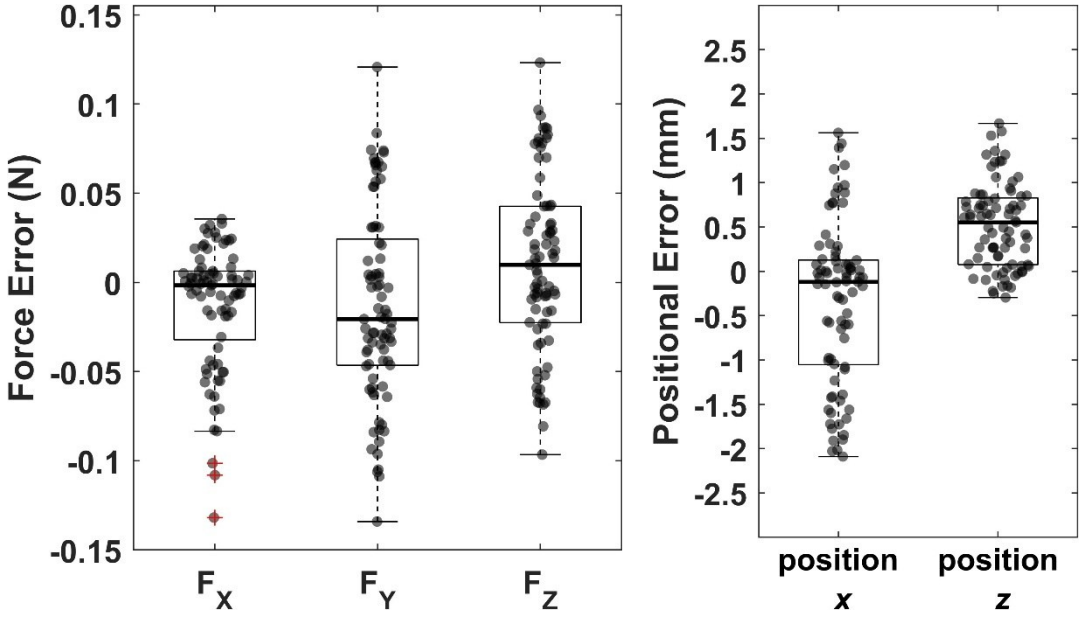
(f)


Force Error (N)
0.15
0.1
0.05
0
-0.05
-0.1
-0.15
F_X
F_Y
F_Z

(g)


Positional Error (mm)
2.5
2
1.5
1
0.5
0
-0.5
-1
-1.5
-2
-2.5
position x
position z

(h)



(i) (j)

Figure A.2 Errors between (A, C, E, G, I) the magnitude of the applied and measured force and (B, D, F, H, J) the applied and measured position for the following combinations: X_2, Y_1, Y_2, Y_4, Z_4; X_3, Y_1, Y_3, Y_4, Z_3; X_2, Y_2, Y_3, Y_4, Z_4; X_3, Y_2, Y_3, Y_4, Z_4; and X_4, Y_2, Y_3, Y_4, Z_4. Outliers, defined as values below the first quartile minus 1.5 times the interquartile range or above the third quartile plus 1.5 times the interquartile range, are denoted by red crosses.

A.3 Post-hoc results of position effect on primary degrees of freedom

Joint	DoF	Size	Pair (Position)	Significance Level
IP	F-E	Small	9 - *	***
IP	F-E	Small	7 - 9	***
IP	F-E	Small	6 - *	***
IP	F-E	Small	* - #	***
IP	F-E	Small	4 - 9	***
IP	F-E	Small	6 - 7	***
IP	F-E	Small	1 - 9	***
IP	F-E	Small	3 - *	***
IP	F-E	Small	7 - #	***
IP	F-E	Small	4 - 6	***
IP	F-E	Small	1 - 6	***
IP	F-E	Small	3 - 7	***
IP	F-E	Small	4 - #	***
IP	F-E	Small	1 - #	**
IP	F-E	Small	8 - *	**
IP	F-E	Small	3 - 4	**
IP	F-E	Small	1 - 3	**
IP	F-E	Small	* - 0	*
IP	F-E	Small	7 - 8	*
IP	F-E	Small	2 - 9	*
IP	F-E	Medium	7 - #	***
IP	F-E	Medium	7 - 9	***
IP	F-E	Medium	* - #	***
IP	F-E	Medium	4 - #	***
IP	F-E	Medium	9 - *	***
IP	F-E	Medium	4 - 9	***
IP	F-E	Medium	6 - 7	***
IP	F-E	Medium	1 - #	***
IP	F-E	Medium	1 - 9	***
IP	F-E	Medium	6 - *	***
IP	F-E	Medium	4 - 6	***
IP	F-E	Medium	1 - 6	**
IP	F-E	Medium	2 - #	*
IP	F-E	Medium	2 - 9	*
IP	F-E	Large	1 - 9	***
IP	F-E	Large	9 - *	***
IP	F-E	Large	7 - 9	***
IP	F-E	Large	1 - 6	***

IP	F-E	Large	4 - 9	***
IP	F-E	Large	1 - #	***
IP	F-E	Large	6 - *	***
IP	F-E	Large	6 - 7	***
IP	F-E	Large	* - #	***
IP	F-E	Large	1 - 3	***
IP	F-E	Large	7 - #	***
IP	F-E	Large	3 - *	**
IP	F-E	Large	3 - 7	**
IP	F-E	Large	4 - 6	**
IP	F-E	Large	4 - #	*
IP	F-E	Large	3 - 4	*
IP	F-E	Large	1 - 8	*
MCP	F-E	Small	1 - #	***
MCP	F-E	Small	4 - #	***
MCP	F-E	Small	7 - #	***
MCP	F-E	Small	1 - 9	***
MCP	F-E	Small	4 - 9	***
MCP	F-E	Small	1 - 0	***
MCP	F-E	Small	* - #	***
MCP	F-E	Small	1 - 6	***
MCP	F-E	Small	2 - #	***
MCP	F-E	Small	4 - 0	***
MCP	F-E	Small	4 - 6	***
MCP	F-E	Small	7 - 9	**
MCP	F-E	Small	7 - 0	**
MCP	F-E	Small	9 - *	*
MCP	F-E	Small	6 - 7	*
MCP	F-E	Small	2 - 9	*
MCP	F-E	Small	3 - #	*
MCP	F-E	Medium	1 - #	***
MCP	F-E	Medium	4 - #	***
MCP	F-E	Medium	1 - 9	***
MCP	F-E	Medium	7 - #	***
MCP	F-E	Medium	* - #	***
MCP	F-E	Medium	2 - #	***
MCP	F-E	Medium	1 - 0	***
MCP	F-E	Medium	4 - 9	***
MCP	F-E	Medium	1 - 6	***
MCP	F-E	Medium	1 - 8	***
MCP	F-E	Medium	4 - 0	***
MCP	F-E	Medium	7 - 9	**

MCP	F-E	Medium	4 - 6	**
MCP	F-E	Medium	5 - #	**
MCP	F-E	Medium	9 - *	**
MCP	F-E	Medium	3 - #	**
MCP	F-E	Medium	2 - 9	**
MCP	F-E	Medium	4 - 8	**
MCP	F-E	Medium	7 - 0	*
MCP	F-E	Medium	* - 0	*
MCP	F-E	Medium	2 - 0	*
MCP	F-E	Large	1 - #	***
MCP	F-E	Large	4 - #	***
MCP	F-E	Large	1 - 9	***
MCP	F-E	Large	2 - #	***
MCP	F-E	Large	4 - 9	***
MCP	F-E	Large	* - #	***
MCP	F-E	Large	2 - 9	***
MCP	F-E	Large	7 - #	***
MCP	F-E	Large	9 - *	***
MCP	F-E	Large	1 - 6	***
MCP	F-E	Large	1 - 0	**
MCP	F-E	Large	5 - #	**
MCP	F-E	Large	4 - 6	**
MCP	F-E	Large	7 - 9	**
MCP	F-E	Large	4 - 0	**
MCP	F-E	Large	3 - #	*
MCP	F-E	Large	2 - 6	*
MCP	F-E	Large	5 - 9	*
MCP	F-E	Large	1 - 8	*
MCP	F-E	Large	2 - 0	*
MCP	F-E	Large	6 - *	*
TMC	A-A	Small	3 - *	***
TMC	A-A	Small	6 - *	***
TMC	A-A	Small	3 - 7	***
TMC	A-A	Small	6 - 7	***
TMC	A-A	Small	9 - *	***
TMC	A-A	Small	3 - 4	***
TMC	A-A	Small	4 - 6	***
TMC	A-A	Small	2 - *	***
TMC	A-A	Small	3 - 0	***
TMC	A-A	Small	6 - 0	***
TMC	A-A	Small	7 - 9	***
TMC	A-A	Small	2 - 7	**

TMC	A-A	Small	4 - 9	*
TMC	A-A	Small	5 - *	*
TMC	A-A	Small	1 - *	*
TMC	A-A	Small	9 - 0	*
TMC	A-A	Small	3 - 8	*
TMC	A-A	Small	6 - 8	*
TMC	A-A	Medium	6 - *	***
TMC	A-A	Medium	3 - *	***
TMC	A-A	Medium	6 - 7	***
TMC	A-A	Medium	3 - 7	***
TMC	A-A	Medium	4 - 6	***
TMC	A-A	Medium	6 - 0	***
TMC	A-A	Medium	2 - *	***
TMC	A-A	Medium	3 - 4	***
TMC	A-A	Medium	3 - 0	***
TMC	A-A	Medium	9 - *	***
TMC	A-A	Medium	2 - 7	***
TMC	A-A	Medium	7 - 9	**
TMC	A-A	Medium	* - #	**
TMC	A-A	Medium	6 - 8	**
TMC	A-A	Medium	1 - 6	**
TMC	A-A	Medium	3 - 8	*
TMC	A-A	Medium	7 - #	*
TMC	A-A	Medium	2 - 4	*
TMC	A-A	Medium	1 - 3	*
TMC	A-A	Medium	5 - 6	*
TMC	A-A	Large	3 - *	***
TMC	A-A	Large	3 - 0	***
TMC	A-A	Large	3 - 7	***
TMC	A-A	Large	3 - 8	***
TMC	A-A	Large	6 - *	***
TMC	A-A	Large	3 - 4	**
TMC	A-A	Large	3 - 5	**
TMC	A-A	Large	6 - 0	**
TMC	A-A	Large	1 - *	*
TMC	A-A	Large	2 - *	*
TMC	A-A	Large	6 - 7	*
TMC	A-A	Large	9 - *	*
TMC	A-A	Large	6 - 8	*
TMC	A-A	Large	3 - #	*
TMC	I-E	Small	1 - *	**
TMC	I-E	Small	2 - *	*

TMC	I-E	Small	1 - 0	*
TMC	I-E	Medium	2 - *	***
TMC	I-E	Medium	1 - *	***
TMC	I-E	Medium	2 - 0	**
TMC	I-E	Medium	2 - 7	**
TMC	I-E	Medium	1 - 0	*
TMC	I-E	Medium	5 - *	*
TMC	I-E	Large	6 - *	*
TMC	F-E	Small	3 - *	***
TMC	F-E	Small	6 - *	***
TMC	F-E	Small	3 - 7	**
TMC	F-E	Small	3 - 0	**
TMC	F-E	Small	9 - *	**
TMC	F-E	Small	3 - 4	**
TMC	F-E	Small	6 - 7	**
TMC	F-E	Small	2 - *	**
TMC	F-E	Small	6 - 0	*
TMC	F-E	Small	4 - 6	*
TMC	F-E	Small	1 - *	*
TMC	F-E	Medium	6 - *	***
TMC	F-E	Medium	3 - *	***
TMC	F-E	Medium	6 - 7	***
TMC	F-E	Medium	6 - 0	***
TMC	F-E	Medium	2 - *	***
TMC	F-E	Medium	3 - 7	***
TMC	F-E	Medium	3 - 0	***
TMC	F-E	Medium	4 - 6	**
TMC	F-E	Medium	9 - *	**
TMC	F-E	Medium	6 - 8	*
TMC	F-E	Medium	3 - 4	*
TMC	F-E	Medium	* - #	*
TMC	F-E	Medium	2 - 7	*
TMC	F-E	Medium	2 - 0	*
TMC	F-E	Large	3 - 0	***
TMC	F-E	Large	3 - *	***
TMC	F-E	Large	3 - 8	**
TMC	F-E	Large	6 - 0	**
TMC	F-E	Large	6 - *	**
TMC	F-E	Large	1 - 0	*
TMC	F-E	Large	3 - #	*
TMC	F-E	Large	1 - *	*
TMC	F-E	Large	3 - 7	*

Table A.1 Post-hoc results of position effect on primary degrees of freedom (DoF). IP: interphalangeal joint; MCP: metacarpophalangeal joint; TMC: trapeziometacarpal joint; F–E: flexion–extension; A–A: adduction–abduction; I–E: internal–external rotation. Statistically different results are only shown (* p_{adj}<0.05, ** p_{adj}<0.01, * p_{adj}<0.001)**

A.4 Kinematics of thumb joints during swiping

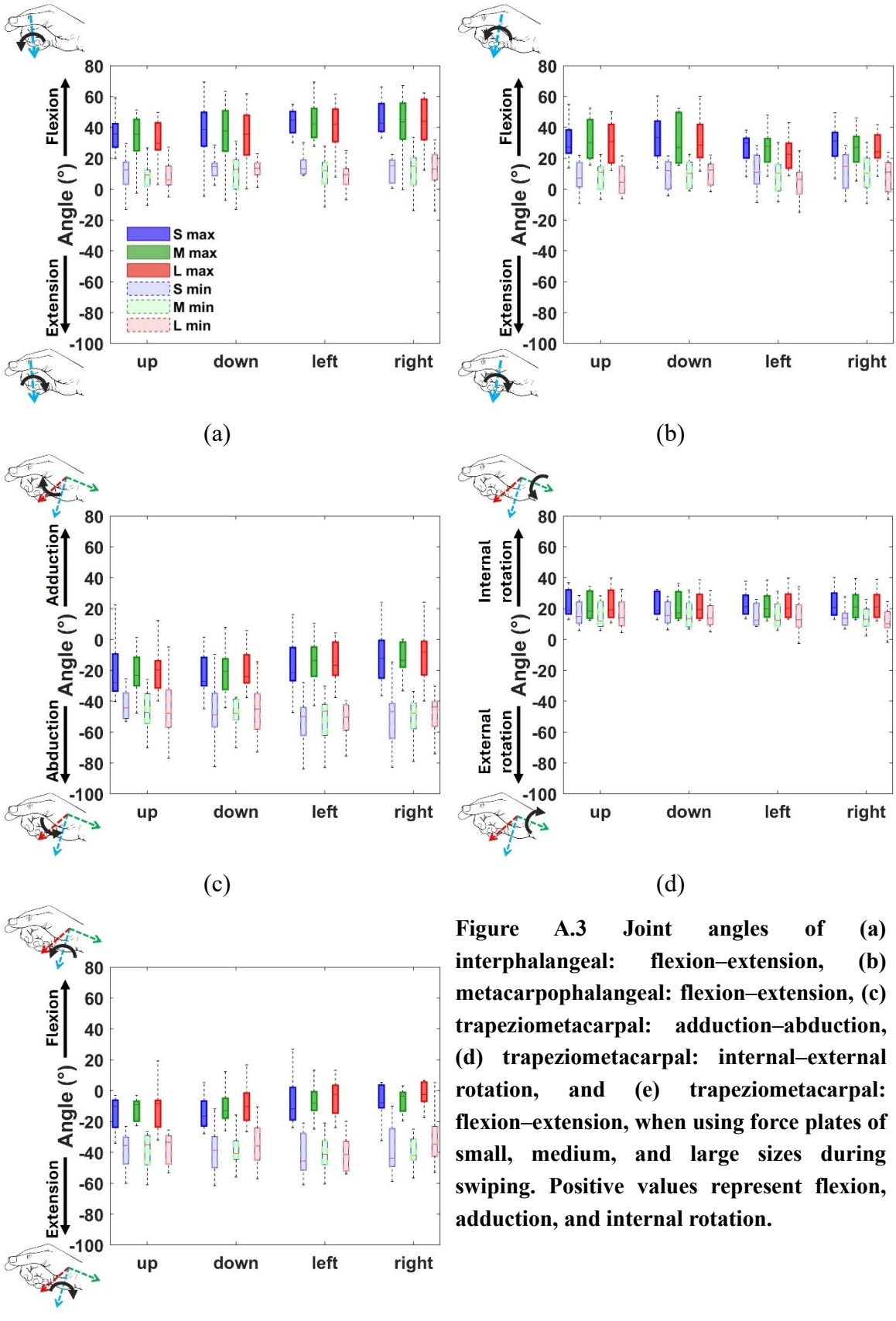


Figure A.3 Joint angles of (a) interphalangeal: flexion–extension, (b) metacarpophalangeal: flexion–extension, (c) trapeziometacarpal: adduction–abduction, (d) trapeziometacarpal: internal–external rotation, and (e) trapeziometacarpal: flexion–extension, when using force plates of small, medium, and large sizes during swiping. Positive values represent flexion, adduction, and internal rotation.

A.5 Coefficient of determination obtained from partial least squares regression

Condition	IP (F-E)	MCP (F-E)	TMC (A-A)	TMC (I-E)	TMC (F-E)	Force
Small-1	0.44	0.21	0.43	0.60	0.40	0.09
Small-2	0.16	0.47	0.52	0.57	0.45	0.25
Small-3	0.12	0.58	0.47	0.67	0.44	0.09
Small-4	0.38	0.42	0.42	0.57	0.46	0.05
Small-5	0.07	0.56	0.53	0.54	0.56	0.72
Small-6	0.03	0.67	0.44	0.59	0.47	0.05
Small-7	0.35	0.60	0.21	0.74	0.31	0.22
Small-8	0.09	0.65	0.43	0.58	0.51	0.36
Small-9	0.04	0.87	0.40	0.58	0.44	0.29
Small-*	0.22	0.42	0.35	0.73	0.31	0.55
Small-0	0.09	0.43	0.27	0.66	0.48	0.76
Small-#	0.10	0.64	0.23	0.61	0.41	0.26
Medium-1	0.49	0.18	0.37	0.67	0.15	0.10
Medium-2	0.49	0.24	0.48	0.51	0.33	0.10
Medium-3	0.36	0.44	0.60	0.53	0.47	0.30
Medium-4	0.37	0.40	0.46	0.71	0.36	0.13
Medium-5	0.19	0.45	0.41	0.60	0.29	0.07
Medium-6	0.18	0.39	0.48	0.49	0.33	0.30
Medium-7	0.35	0.38	0.45	0.75	0.31	0.33
Medium-8	0.10	0.52	0.43	0.72	0.35	0.15
Medium-9	0.19	0.60	0.52	0.54	0.35	0.26
Medium-*	0.57	0.39	0.53	0.81	0.50	0.20
Medium-0	0.13	0.38	0.34	0.78	0.34	0.35
Medium-#	0.15	0.49	0.35	0.65	0.33	0.13
Large-1	0.38	0.23	0.61	0.59	0.76	0.70
Large-2	0.25	0.37	0.70	0.62	0.78	0.58
Large-3	0.19	0.51	0.62	0.63	0.66	0.47
Large-4	0.42	0.40	0.51	0.57	0.77	0.59
Large-5	0.28	0.48	0.63	0.57	0.81	0.45
Large-6	0.08	0.57	0.59	0.67	0.53	0.40
Large-7	0.42	0.40	0.46	0.52	0.60	0.69
Large-8	0.23	0.47	0.61	0.65	0.80	0.28
Large-9	0.05	0.51	0.49	0.62	0.54	0.31
Large-*	0.64	0.32	0.29	0.81	0.37	0.62
Large-0	0.37	0.43	0.42	0.70	0.51	0.09
Large-#	0.10	0.47	0.37	0.53	0.49	0.11
Small-up	0.39	0.43	0.66	0.42	0.63	0.09
Small-down	0.27	0.36	0.45	0.54	0.54	0.07

Small-left	0.07	0.90	0.78	0.61	0.78	0.05
Small-right	0.59	0.75	0.60	0.39	0.70	0.03
Medium-up	0.38	0.31	0.56	0.42	0.51	0.15
Medium-down	0.30	0.37	0.46	0.14	0.56	0.20
Medium-left	0.03	0.80	0.51	0.79	0.51	0.08
Medium-right	0.26	0.73	0.28	0.51	0.35	0.50
Large-up	0.42	0.37	0.62	0.51	0.43	0.62
Large-down	0.25	0.23	0.74	0.29	0.74	0.20
Large-left	0.05	0.74	0.65	0.59	0.76	0.26
Large-right	0.41	0.76	0.27	0.36	0.37	0.41

Table A.2 R^2 obtained from partial least squares regression (PLS) for all experimental conditions.

A.6 Methods of delineating trapeziometacarpal ligaments

Ligament	Length (mm)	Width (mm)	Thickness (mm)
DRL	7.12 ± 1.67	11.39 ± 1.92	2.25 ± 0.33
POL	10.08 ± 1.41	4.97 ± 0.89	1.35 ± 0.28
sAOL	9.45 ± 1.61	8.59 ± 2.61	1.34 ± 0.25
dAOL	8.37 ± 1.68	5.45 ± 0.45	1.17 ± 0.15
UCL	8.05 ± 2.02	3.35 ± 0.33	0.83 ± 0.12
dIML	10.67 ± 1.65	3.70 ± 0.83	1.10 ± 0.08
IML	9.67 ± 2.26	3.47 ± 1.26	1.03 ± 0.18

*Values are presented as mean ± standard deviation

Table A.3 Dimensions of the TMC ligaments measured by Bettinger et al. (1999)

Ligament	Length (mm)	Width (mm)	Thickness (mm)
DRL	13.6 ± 2.7	5.9 ± 1.0	0.9 ± 0.2
POL	11.2 ± 1.2	12.6 ± 2.2	1.0 ± 0.1
sAOL	10.3 ± 3.3	15.3 ± 2.2	1.0 ± 0.1
dAOL	9.8 ± 1.5	7.19 ± 2.0	1.0 ± 0.1
UCL	18.2 ± 2.9	3.37 ± 0.8	1.0 ± 0.1
dIML	10.7 ± 2.4	3.45 ± 0.6	1.0 ± 0.1
IML	12.6 ± 3.0	3.7 ± 1.2	1.0 ± 0.1

*Values are presented as mean ± standard deviation

Table A.4 Dimensions of the TMC ligaments measured by Nanno et al. (2006)

Ligament	Length (mm)	Width (mm)	Thickness (mm)
DRL	9.75 ± 0.81	5.00 ± 0.61	1.86 ± 0.12
DCL	9.18 ± 1.29	4.92 ± 0.25	1.95 ± 0.14
POL	13.03 ± 1.58	5.95 ± 0.40	1.71 ± 0.22
AOL	9.38 ± 0.61	4.68 ± 0.52	0.71 ± 0.11
UCL	9.36 ± 0.60	4.27 ± 0.26	0.98 ± 0.14
IML	10.29 ± 0.75	2.20 ± 0.39	0.79 ± 0.09

*Values are presented as mean ± standard deviation

Table A.5 Dimensions of the TMC ligaments measured by Ladd et al. (2012)